*Paper ID: FM-001*

# Energy Consumption Scenario of Submersible Pumps Using in the Barind Area of Bangladesh

M. E. Haque[1], M. R. Islam[1], J. Ferdous[1], M. S. Akhter[1], H. Haniu[2]

[1]Department of Mechanical Engineering, Rajshahi University of Engineering & Technology, Bangladesh
[2]Department of Mechanical Engineering, Kitami Institute of Technology, Kitami City, Hokkaido 090-8507, Japan
*Email: emdad359456@yahoo.com*

## Abstract

*In this work the ground water level and water pumping for irrigation and drinking purposes in Northern part of Bangladesh have been studied. The Barind Multipurpose Development Authority (BMDA) and Rajshahi WASA are the major water supplying authority in the Northern Part of Bangladesh by using 14386 and 87 nos of submersible pumps, respectively. The depth of ground water level remains under 30ft throughout the year that enforcing the use of submersible pumps in most parts of Barind zone. An investigation for the values of lifecycle cycle cost elements of submersible pumps has also been carried out. Energy consumption cost is dominating the life cycle cost of the pumps using in this region and improper matching of pump performance and operation/system requirements are the main causes of energy loss. It is found that 10% to 30% of the energy consumed by submersible water pumps could be saved through the change of way of operation and control system.*

Keywords: Barind area, Submersible pump, Energy consumption, Ground water level.

## 1. Introduction

Pumping systems account for nearly 20% of the world's electrical energy demand and range from 25-50% of the energy usage in certain industrial plant operations [1]. Pumping systems are widespread; they provide domestic services, commercial and agricultural services, municipal water/wastewater services, and industrial services for food processing, chemical, petrochemical, pharmaceutical, and mechanical industries. The energy and materials used by a pump depend on the design of the pump, the design of the installation, and the way the system is operated. These factors are interdependent [1-3].

The demand for submersible pumps has been rising recently. World leading pump companies are continually building up the share of submersible pumps in their production volumes. While 50 years ago submersible pumps with air-filled electric motors were produced by only one company, by the 1990s all of the ten leading manufacturers of pumps produced submersibles. These companies, which together account for a third of the world market, dictate their policy to the remaining 10000 pump manufacturers [2-3].

During the draught season, the ground water goes down at lower level. It is generally caused when the groundwater heads in an aquifer fall below a critical level over a certain period of time due to natural or human induced causes and inventions. In the recent past, there was increased frequency of draughts in Bangladesh. Particularly, the Northern region of the country was severely affected by the occurrence of draughts and high variability in rainfall. At that time, farmers had to face tough situation due to scarcity of water and they had to dependent on ground water for irrigation. As the ground water level is declining day by day, it is almost impossible to lift water by low lift pump like centrifugal pump for irrigation, drinking and industrial purposes today. It has become urgent to lift water by high lift pump like submersible pump for irrigation and other purposes. Barind Multipurpose Development Authority (BMDA) takes initiatives for irrigation using ground water by installing deep well and supply drinking water in barind area where the depth of ground water level is high.

There are variety brands of submersible pumps available in the market place. Some of them are cheap but shorter lifespans and high maintenance and energy consumption costs. These cheapest brands pump draw primary interest of the most customers. Some other brands have comparatively longer lifespan with low maintenance and energy costs. The customers do not feel interest for high price of these pumps that is very smaller than the energy consumption cost during its life. Under these circumstances it is crucial to obtain an optimum solution for selecting a good pump and also operation of submersible pumps. However, the main objectives of the present study: (i) to investigate the causes of energy loss in operation of submersible pumps in Bangladesh.(ii) to study the ground water level in Rajshahi divisions for different seasons.(iii) to study the life cycle cost (LCC) for submersible pumps using in Northern part of Bangladesh.

## 2. Elements of Life Cycle Costs

The life cycle cost (LCC) of any pump is the total lifetime cost include initial costs, installation and commissioning costs, energy costs, operational costs, maintenance and repair costs, down time costs, environmental costs, and decommissioning and disposal cost [1].

However, LCC may be expressed mathematically by Eq$^n$. (1)

$$LCC = C_{ic} + C_{in} + C_e + C_o + C_m + C_s + C_{env} + C_d \qquad (1)$$

Where,

**$C_{ic}$ is the initial cost of the pump**: The initial costs usually includes: engineering (e.g. design and drawings, regulatory issues); the bid process; purchase order administration; testing and inspection; inventory of spare parts; training; auxiliary equipment for cooling and sealing water.

**$C_{in}$ is the installation cost that includes:** Foundations—design, preparation, concrete and reinforcing and installation of deep well; setting and grouting of equipment on foundation; connection of process piping; connection of electrical wiring and instrumentation; connection of auxiliary systems and other utilities; provisions for flushing or 'water runs'; performance evaluation at start-up.

**$C_e$ is the energy costs:** Energy consumption is often one of the larger cost elements and may dominate the LCC, especially if pumps run more than 2000 hours per year [1]. Energy consumption is calculated by gathering data on the pattern of the system output. If output is steady, or essentially so, the calculation is simple. If output varies over time, then a time-based usage pattern needs to be established. The input power calculation formula is:

$$P = \frac{Q \times H \times S}{366 \times \eta_p \times \eta_m}[kW] \qquad (2)$$

Where, P = power, H = head (m), Q = rate of flow (m$^3$/hr.), $\eta_p$ = pump efficiency, $\eta_m$ = motor efficiency and S = specific gravity (for water S = 1)

**$C_o$ is the operational costs:** Operation costs are labor costs related to the operation of a pumping system. These vary widely depending on the complexity and duty of the system. For example, a hazardous duty pump may require daily checks for hazardous emissions, operational reliability, and performance within accepted parameters. On the other hand, a fully automated non-hazardous system may require very limited supervision. Regular observation of how a pumping system is functioning can alert operators to potential losses in system performance. Performance indicators include changes in vibration, shock pulse signature, temperature, noise, power consumption, flow rates, and pressure.

**$C_m$ is the maintenance and repair cost:** Obtaining optimum working life from a pump requires regular and efficient servicing. The manufacturer will advise the user about the frequency and the extent of this routine maintenance. Its cost depends on the time and frequency of service and the cost of materials. The design can influence these costs through the materials of construction, components chosen, and the ease of access to the parts to be serviced. The maintenance program can be comprised of less frequent but more major attention as well as the more frequent but simpler servicing. The major activities often require removing the pump to a workshop. During the time the unit is unavailable to the process plant, there can be loss of product or a cost from a temporary replacement. These costs can be minimized by programming major maintenance during annual shut-down or process change-over. Major Service can be described as "pump unit not reparable on site," while the routine work is described as "pump unit reparable on site." The total cost of routine maintenance is found by multiplying the costs per event by the number of events expected during the life cycle of the pump. Although unexpected failures cannot be predicted precisely, they can be estimated statistically by calculating mean time between failures (MTBF). MTBF can be estimated for components and then combined to give a value for the complete machine.

**$C_s$ is the downtime cost:** The cost of unexpected downtime and lost production is a very significant item in the total LCC and can rival the energy costs and replacement parts costs in its impact. Despite the design or target life of a pump and its components, there will be occasions when an unexpected failure occurs. In those cases where the cost of lost production is unacceptably high, a spare pump may be installed in parallel to reduce the risk. If a spare pump is used, the initial cost will be greater but the cost of unscheduled maintenance will include only the cost of the repair. The cost of lost production is dependent on downtime and differs from case to case.

**$C_{env}$ is the environmental cost:** The cost of contaminant disposal during the lifetime of the pumping system varies significantly depending on the nature of the pumped product. Certain choices can significantly reduce the amount of contamination, but usually at an increased investment cost. Examples of environmental contamination can include: cooling water and packing box leakage disposal; hazardous pumped product flare-off; used lubricant disposal; and contaminated used parts, such as seals. Costs for environmental inspection should also be included.

**C<sub>d</sub> is the decommissioning cost:** In the vast majority of cases, the cost of disposing of a pumping system will vary little with different designs. This is certainly true for non-hazardous liquids and, in most cases, for hazardous liquids also. Toxic, radioactive, or other hazardous liquids will have legally imposed protection requirements, which will be largely the same for all system designs. A difference may occur when one system has the disposal arrangements as part of its operating arrangements (for example, a hygienic pump designed for cleaning in place) while another does not (for example, a hygienic pump designed for removal before cleaning). Similar arguments can be applied to the costs of restoring the local environment. When disposal is very expensive, the LCC becomes much more sensitive to the useful life of the equipment.

## 3. Water Pumping by BMDA and Rajshahi WASA in Northern Part of Bangladesh

Barind Multipurpose Development Authority (BMDA), Rajshahi is supplying water by using deep well pumps mainly for irrigation in sixteen districts of Northern part of Bangladesh. In some cases the BMDA supplies drinking water in Barind areas. There are total of 14999 Nos. deep well pumps under BMDA among which 14386 Nos. pumps are submersible and 613 Nos. are turbine pumps up to June 2015 [6]. Rajshahi Water Supply and Swerage Authority (Rajshahi WASA), Bangladesh is using 87 Nos. submersible pumps for supply of drinking water and household affairs in Rajshahi City Corporation (RCC) [7]. Besides, a big number pumps of smaller capacity are running for the supply of water for irrigation and drinking purposes by other organizations/private sectors in agricultural fields and towns of the Northern part of Bangladesh. Table 1 shows distribution of zone wise deep well pumps used by BMDA and Rajshahi WASA up to June 2015.

Table 1. Distribution of zone wise deep well pumps used by BMDA and Rajshahi WASA

| Sl. No. | Name of water supply authority | Name of zone | Nos of deep well pumps |
|---|---|---|---|
| 1 | BMDA | Rajshahi | 2883 |
| 2 | | Chapai Nawabgonj | 1641 |
| 3 | | Naogaon – 1 | 2149 |
| 4 | | Naogaon – 2 | 1951 |
| 5 | | Joypurhat | 319 |
| 6 | | Bogura | 236 |
| 7 | | Pabna | 328 |
| 8 | | Sirajgonj | 160 |
| 9 | | Natore | 300 |
| 10 | | Taqurgaon | 1340 |
| 11 | | Dinajpur | 1469 |
| 12 | | Ponchogor | 357 |
| 13 | | Gaibandha | 374 |
| 14 | | Rongpur | 572 |
| 15 | | Nilphamari | 229 |
| 16 | | Kurigram | 408 |
| 17 | | Lalmonirhat | 283 |
| 18 | Rajshahi WASA | Rajshahi City Corporation (RCC) | 87 |
| | | Total Nos. of pump | 15086 |

A survey work has been completed for the assessment of life cycle cost of submersible pumps that are using by BMDA and Rajshahi WASA. The reasonable values of the life cycle cost elements obtained from field data and practical experiences of the Engineers, Technicians and Operators engaged in the field level. The field data obtained from the survey work for determining the values of life cycle cost components for submersible pumps of capacity 1 cusec are summerised in Table 2.

The operation of a submersible pump of capacity 1 cusec that is supplying water for both irrigation and drinking purposes at the site Shantoshpur, Paba near Rajshahi City Corporation area has been investigated. The layout of the submersible pump under study is presented in Fig. 1. Figure shows that the depth of well from the earth surface is 186 feet and submersible pump is hanged at 80 feet depth submersed in ground water. A drinking water overhead tank is placed at 30 feet above the ground level. Stainless steel strainer is used to separate water

from gravel packing. A screen is used for filtering water at the intake of the pump. The fluctuation of the ground water level over the year at site is shown in Fig. 2. (a).

Table 2. Field data for submersible pumps of 1 cusec capacity used by BMDA and Rajshahi WASA [6, 7]

| Sl. No. | Item description | BMDA | Rajshahi WASA |
|---------|------------------|------|---------------|
| 1 | Total number of pumps (Nos) | 14999 | 87 |
| 2 | Pump types | Submersible and only 613 nos are Turbine | Submersible |
| 3 | Pump brand | KSB, SABAR, KALAMA | KSB |
| 4 | Capacity of the pump (Cusec) | 0.75 – 2.00 | 1.00 |
| 5 | Purpose of the pump | Irrigation and drinking water supply | drinking water supply |
| 6 | Price of the pump/ initial cost (TK) | 1,50,000.00/pump | 5,50,000.00/pump |
| 7 | Installation cost (TK) | 15,00,000.00/pump | 22,50,000.00/pump |
| 8 | Annual operational cost (TK) | 52,000.00/pump | 2,16,000.00/pump |
| 9 | Annual energy consumption (kWhr) | 34,000/pump | 66,000/pump |
| 10 | Energy rate (TK/kWhr) | 9.00 | 10.00 |
| 11 | Annual pump maintenance cost (TK) | 11,500.00/pump | 1,00,000.00/pump |
| 12 | Average life of pump (years) | 10 – 15 | 15 – 18 |
| 13 | Water supply system | Burried | Burried |

.
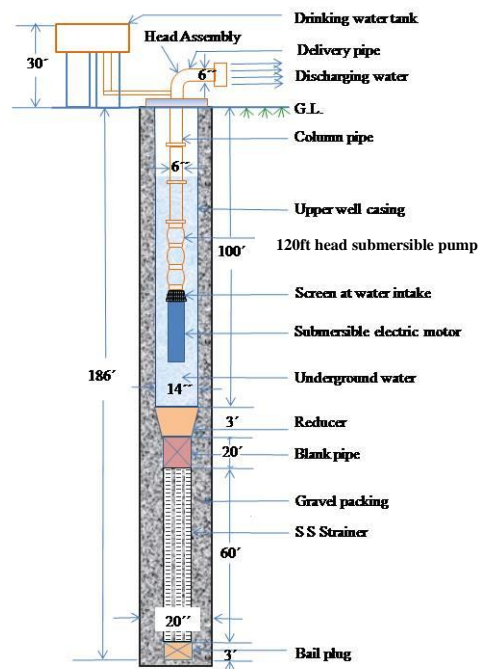


Fig. 1. Layout of 1 cusec capacity submersible pump at Shantoshpur, Paba, Rajshahi.

## 4. Water Level in Northern Part of Bangladesh

The survey work has been completed for detail study of ground water level in 25 Thana of Northern part of Bangladesh for five years. The ground water level for four sites is presented in Figs. 2(a)-(d). It is seen from these Figs. 2 (a)-(d) that the depth of ground water level is high during January-June and low during July-December. It is also seen from these figures that ground water level fluctuates yearly and on the basis of region. Fig. 2(a) and (b) shows that depth of ground water level is almost 40 feet at Shantospur, Paba, Rajshahi site and

60 feet at Atahar, Nawabgonj, Chapai Nawabgonj respectively due to dryness of the river Padma. Thus it is essential to use submersible pumps in Rajshahi and Chapai Nawabgonj regions. For this reason Table 1 shows more numbers of submersible pumps are using in these regions. Fig. 2 (c) and (d) shows that during the last five years maximum depth of ground water level is 22 feet at Chakmarojpur, Gaibandha and 25 feet at Chakai, Birganj, Dinajpur respectively. As the rivers Jamuna and Tista flows beside these regions, depth of ground water level remains low almost throughout the year. This is why less numbers of submersible pumps are using in these regions shown in Table 1.
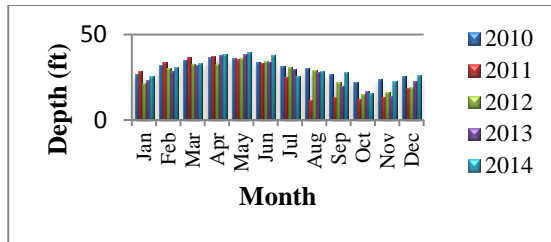


(a) Shantoshpur, Paba, Rajshahi site
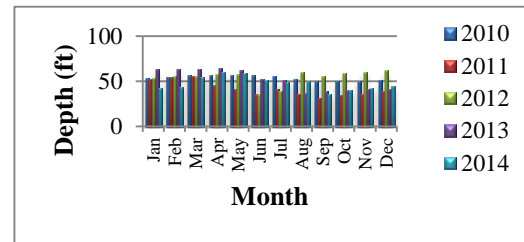


(b) Atahar, Nawabgonj, Chapai Nawabgonj site
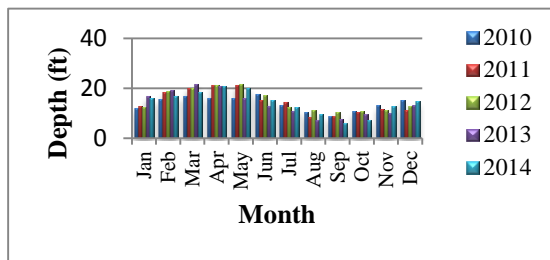


(c) Chakmarojpur, Gaibandha site
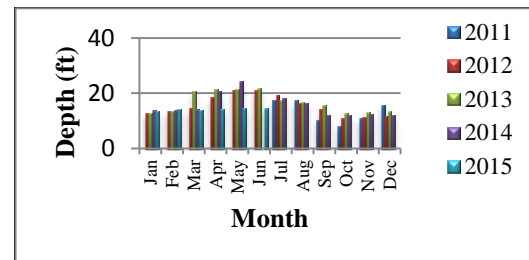


(d) Chakai, Birganj, Dinajpur site

Fig. 2. Yearly fluctuation of ground water level in different sites of Northern part of Bangladesh [6].

## 5. Results and Discussion

The performance of KSB brand submersible pump have been studied in Bangladesh University of Engineering and Technology (BUET) and its characteristics is presented in Fig. 3. From this figure it is seen that the pump shows best efficiency when the discharge of the pump is 1 cusec under a head of 120ft. If the pump operates in either sides of the best efficiency point, combined efficiency decreases and ultimately more energy is consumed to get specified amount of water by the pump. The energy loss of a submersible pump occurs due to various causes. The main causes of energy loss includes: operation with over calculated head; operation with high flows; running far from their best efficiency point (BEP); change in surface roughness of impeller and diffuser; change in flow path size in the pump; variable speed drive of the pump; improper matching of pump performance and system requirements [4-5].
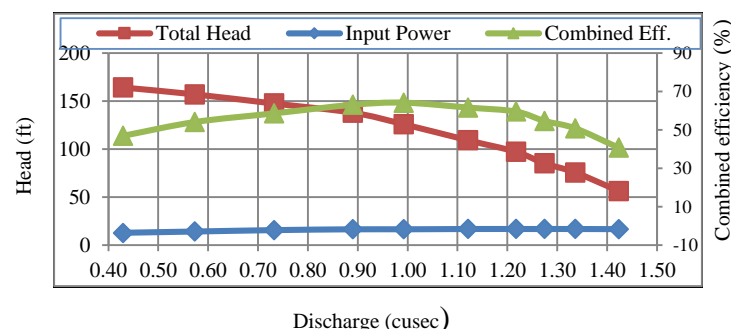


Fig. 3. Characteristics of KSB brand submersible pump of capacity 1 cusec under head of 120 ft using by BMDA

The life cycle cost of a submersible pump using by BMDA and Rajshahi WASA have been determined with the help of Eqt$^n$ – (1) and field data from Table 2. The calculated life cycle cost components are presented in Fig. 4 (a)-(b) and also compared with those of a waste water pump of Fig.(c). From these figures it can be seen that

energy and installation costs of submersible pump using by BMDA and Rajshahi WASA are higher but maintenance and operation costs are lower than that of waste water pump. It is also seen from these figures that operational cost of Rajshahi WASA is higher than that of BMDA because of the pumps of WASA runs throughout the year while the pumps of BMDA runs mostly during irrigation period. The energy cost of BMDA and WASA pumps is higher than that of waste water pump. Other cost components are almost similar. The life cycle analysis for the pump ensures that the energy cost component is the major element. From Fig. 3 it can also be seen that if the pump delivers water under head of 100ft, then its combined efficiency will reduced to 60% and consequently energy loss up to 10%. On the other hand if the pump operates under a head of 150ft and energy loss becomes up to 30%. These loss can be reduced by repositioning (lowering)/uppering) the pumps twice a year, one in the month January and other repositioning in July following ground water level history in respective sites. Drinking water supply using the same pump of irrigation site add extra head on the pump. This additional head reduces the efficiency of the pump.
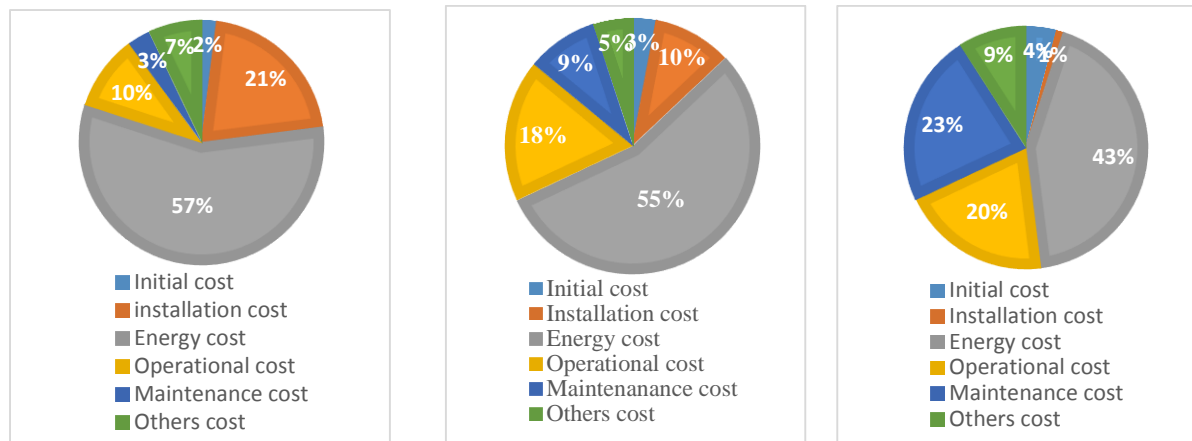


(a) Pump of the BMDA, Rajshahi     (b)Pump of the Rajshahi WASA,     (c) Waste water pump U.S.A

Fig 4. Life cycle cost for a 1 cusec, 120 ft head submersible pump using by BMDA, Rajshahi WASA and Waste water pump

## 6. Conclusions

The initial purchase price is a small part of the life cycle cost for high usage pumps. Operating requirements may sometimes override energy consumption considerations, an optimum solution is still possible. A greater understanding of all the components that make up the total cost of ownership will provide an opportunity to dramatically reduce energy consumption, operational, and maintenance costs.

## 7. Acknowledgement

## References

1]    A guide to LCC analysis for pumping systems. U.S. Department of Energy. www.pumps.org. January 2001.

[2]    Wet and dry installation of submersible pumps. World Pumps, www.worldpumps.com. October 2007.

[3]    Optimizing operational efficiency in submersible pumps. World Pumps, www.worldpumps.com. April 2004.

[4]    Energy efficiency in pump specification. World Pumps, www.worldpumps.com. April 2001

[5]    Energy cost savings with centrifugal pumps. Word Pumps, www.worldpumps.com March 2009.

[6]    A survey report on water pumping under BMDA. BMDA, Rajshahi, Bangladesh. September 2015

[7]    A survey report on water pumping under Rajshahi WASA. Rajshahi WASA, Bangladesh, September 2015.

.

# Free Convection Heat & Mass Transfer on Steady MHD Boundary Layer Flow over a Hot Stretching Plate with Hall Current and Heat Generation

## M. Ali[1]*, M. A. Alim[2], M. S. Alam[3]

[1,3]Chittagong University of Engineering and Technology (CUET), Chittagong-4349, Bangladesh
[2]Bangladesh University of Engineering and Technology (BUET), Dhaka-1000, Bangladesh
*E-mail: ali.mehidi93@gmail.com, [2]E-mail: maalim@math.buet.ac, [3]E-mail: shahalammaths@gmail.com

## Abstract

*The present problem is focused on steady two-dimensional magnetohydrodynamic (MHD) free convection, heat and mass transfer flow of an incompressible electrically conducting fluid over a hot stretching plate under the influence of an applied uniform magnetic field with Hall current and heat generation. The numerical results concerned with the primary velocity, secondary velocity, temperature and concentration profiles effects of various parameters on the flow fields are investigated and presented graphically for air with a Prandtl number of 0.71. The results presented graphically illustrate that primary velocity field decrease due to increase of magnetic parameter but increase for the values of heat source parameter while there is no effect for Hall parameter. Again the secondary velocity is increased for the increasing values of magnetic and Hall parameter but negligible decreasing effect for heat generation parameter. Temperature field increases in the presence of heat generation parameter whereas it is decreased for the increasing values of magnetic parameter and Prandtl number. Again, the concentration is decreased for the increasing values of Schmidt number and magnetic parameter but negligible increasing effect for heat generation parameter. To verify the validity and accuracy of the present numerical results for the skin friction coefficient $f''(0)$ and the local Nusselt number $\left[-\theta'(0)\right]$ are compared with results of Ishak et al. [7] in absence of Hall current and heat generation.*

Keywords: MHD, Hall current, Heat generation, Stretching sheet.

## 1. Introduction

MHD laminar boundary layer flow problems has become of its important applications in industrial manufacturing processes like plasma studies, petroleum industries, Magneto-hydrodynamics power generator, cooling of Nuclear reactors, boundary layer control in aerodynamics. Also , MHD laminar boundary layer behavior over a stretching surface is a significant type of flow having considerable practical applications in paper production, hot rolling, wire drawing, drawing of plastic films, metal and polymer extrusion, metal spinning and polymer processing. In this regard, various authors has been done a lot of works related to this field such as Venkatesulu and Rao [1] analyzed the effect of Hall Currents and Thermo-diffusion on convective heat and mass transfer flow of a viscous, chemically reacting rotating fluid through a porous medium past a vertical porous plate, Mathew *et al.* [2] studied Hall effects on heat and mass transfer through a porous medium in a rotating channel with radiation, Kumar and Singh [3] have been studied mathematical modeling of Soret and hall effects on oscillatory MHD free convective flow of radiating fluid in a rotating vertical porous channel filled with porous medium, Ruzicka [4] have also studied heat and mass transfer past a vertical flat porous plate through a porous medium with variable thermal conductivity, Chauhan [5] considered the effect of Hall current on MHD slip flow and heat transfer through a porous medium over an accelerated plate in a rotating system, further Hayat *et al.* [6] studied the slip effects on peristaltic transport in an inclined channel with mass transfer and chemical reaction. In view of the importance, the present work is focused on steady MHD free convection, heat and mass transfer flow of an incompressible electrically conducting fluid over a hot stretching sheet with Hall current and heat generation under the influence of an applied uniform magnetic field. The study extends the work of Ishak *et al.* [7] by considering the Hall and heat generation effects. Finally, the numerical values of the skin friction, wall temperature gradient and concentration gradient are also shown in a tabular form.

## 2. Governing Equations of the Present Problem and Similarity Analysis

Let us consider steady two dimensional MHD free convection heat and mass transfer in an incompressible electrically conducting fluid flow over a hot stretching sheet in a rotating system under the influence of an

applied uniform magnetic field. The flow is subjected to a transverse magnetic field of strength $B_0$ which is assumed to be applied in the positive $y$ –direction normal to the surface. By taking the magnetic Reynolds number is so small that the induced magnetic field is negligible. The pressure gradient, body force, viscous dissipation and joule heating effects are neglected because their values are generally small compared with the effects of internal heat generation. Under these above assumptions along with Boussinesq and usual boundary layer approximation, the dimensional governing equations of continuity, momentum, concentration and energy under the influence of externally imposed magnetic field with the presence of Hall current are [7] and [2]:

Equation of continuity:

$$\frac{\partial u}{\partial x} + \frac{\partial v}{\partial y} = 0 \tag{1}$$

Momentum equation:

$$u\frac{\partial u}{\partial x} + v\frac{\partial u}{\partial y} = v\frac{\partial^2 u}{\partial y^2} + g\beta(T - T_\infty) + g\beta^*(C - C_\infty) - \frac{\sigma B_0^2}{\rho(1 + m^2)}(u + mW) \tag{2}$$

$$u\frac{\partial W}{\partial x} + v\frac{\partial W}{\partial y} = v\frac{\partial^2 W}{\partial y^2} + \frac{\sigma B_0^2}{\rho(1 + m^2)}(mu\text{-}W) \tag{3}$$

Energy Equation:

$$u\frac{\partial T}{\partial x} + v\frac{\partial T}{\partial y} = \frac{k}{\rho c_p}\frac{\partial^2 T}{\partial y^2} + \frac{Q_0}{\rho c_p}(T - T_\infty) \tag{4}$$

Concentration Equation: [1]

$$u\frac{\partial C}{\partial x} + v\frac{\partial C}{\partial y} = D\frac{\partial^2 C}{\partial y^2} \tag{5}$$

Boundary conditions are:

$$u = a,\ v = 0, W = 0, T = T_w = T_\infty + bx, C = C_w \ at \ y = 0$$
$$u = 0, v = 0, T = T_\infty, C = C_\infty \ as \ y \to \infty$$

where $u$, $v$ and $W$ are the velocity components along $x$, $y$ and $z$ directions, $T$, $T_w$ and $T_\infty$ are the fluid temperature, the stretching sheet temperature and the free stream temperature respectively while $C$, $C_w$ and $C_\infty$ are the corresponding concentrations, $k$ is the thermal conductivity, $Q_0$ is the heat generation constant, $m$ is the Hall parameter, $a$ is the constant, $b$ is arbitrary constant, $C_p$ specific heat with constant pressure, $\mu$ is the coefficient of viscosity, $v$ is the kinematic viscosity , $\sigma$ is the electrical conductivity, $\rho$ is the fluid density, $\beta$ is the thermal expansion coefficient, $\beta^*$ is the concentration expansion coefficient, $B_0$ is the magnetic field intensity, $g$ is the acceleration due to gravity, $D$ is the coefficient of mass diffusivity respectively. We introduce the steam function $\psi(x,y)$ as defined by $u = \frac{\partial \psi}{\partial y}$ and $v = -\frac{\partial \psi}{\partial x}$.

To convert the governing equations into a set of similarity equations, we introduce the following similarity transformation:

$$W = axg,\ \eta = y\sqrt{\frac{a}{v}},\ \psi = x\sqrt{av}\,f, \theta(\eta) = \frac{T - T_\infty}{T_w - T_\infty}, \varphi(\eta) = \frac{C - C_\infty}{C_w - C_\infty}$$

2

From the above transformations, the non-dimensional, nonlinear and coupled ordinary differential equations are obtained as

$$f''' + ff'' + Gr\,\theta + Gm\,\varphi - \frac{M}{1+m^2}f' + \frac{Mm}{1+m^2}g = 0 \tag{6}$$

$$g'' - f'g + g' - \frac{M}{1+m^2}g + \frac{Mm}{1+m^2}f' = 0 \tag{7}$$

$$\theta'' + \Pr f\theta' - \Pr f'\theta + Q\theta = 0 \tag{8}$$

$$\varphi'' + Scf\varphi' = 0 \tag{9}$$

The transform boundary conditions:

$$f = 0,\ f' = 1,\ g = 0,\ \theta = \varphi = 1\ at\ \eta = 0\ \text{and}\ f' = g = \theta = \varphi \to 0\ as\ \eta \to \infty$$

Where $f'$, g, $\theta$ and $\varphi$ are the dimensionless primary velocity, secondary velocity, temperature and concentration profiles respectively, $\eta$ is the similarity variable, the prime denotes differentiation with respect to $\eta$. Also the non-dimensional parameters

$$Gr = \frac{g\beta(T_w - T_\infty)}{a^2 x}, \Pr = \frac{v}{\alpha}, M = \frac{\sigma B_0^2}{\rho a}, Q = \frac{Q_0}{a\rho c_p}, Gm = \frac{g\beta^*(C_w - C_\infty)}{a^2 x}, Sc = \frac{v}{D}$$

are the Grashof number, Prandtl number, magnetic parameter, heat generation parameter, modified Grashof number and Schmidt number respectively.

## 3. Results and Discussion
Numerical calculation for distribution of the primary velocity, secondary velocity, temperature and concentration profiles across the boundary layer are displayed in Fig. 1- Fig.12 for different values of magnetic parameter *M*, Hall parameter *m*, heat source *Q*, Prandtl number *Pr* and Schmidt number *Sc* and for fixed values of *Gr* and *Gm*. Throughout the calculations, the bouncy parameter *Gr = -5.0* and *Gm = -5.0* are taken which correspond to a hot plate and other parameters are chosen arbitrary.

The effects of various parameters on primary velocity profile are shown in Fig. 1- Fig. 3. In Fig. 1 it is observed that the velocity decreases with an increase in the *M*. The magnetic parameter is found to retard the velocity at all points of the flow field. It is because that the application of transverse magnetic field will result in a resistive type force (Lorentz force) similar to drag force which tends to resist the fluid flow and thus reducing its velocity. Reverse effect arises for the increasing values of heat generation parameter which are shown in Fig.3 cause increasing heat generation would increase bouncy force as a result velocity increases. From Fig.2 it is observed that there is no effect on primary velocity profile for Hall parameter.
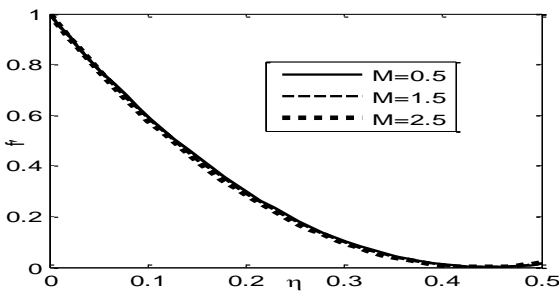


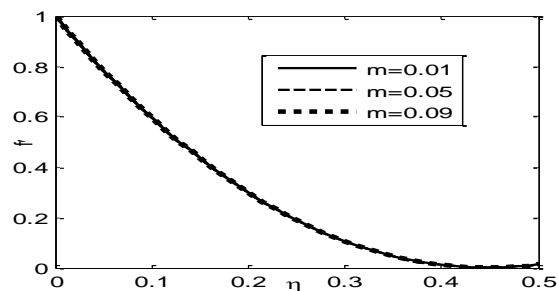Fig.1. Primary velocity profile for various values of *M*          Fig.2. Primary velocity profile for various values of *m*
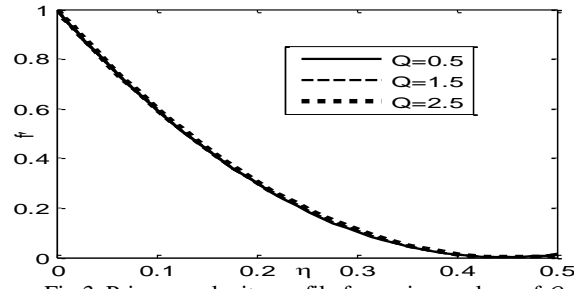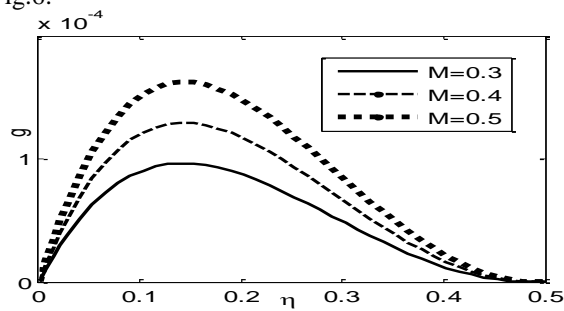
Fig.3. Primary velocity profile for various values of $Q$

Fig.4- Fig.6 display the effect of various entering parameters on secondary velocity profile. From these figures it is seen that the secondary velocity starts from minimum value at the plate and increases until it attains the maximum value within the boundary layer and then starts decreasing until it reaches the free stream area satisfying the far field boundary condition. The noticeable increasing effect of magnetic and Hall parameter on secondary velocity profile are observed which are shown in Fig.4 and Fig.5. Again, it is interesting to note that the other mentioned parameter has negligible decreasing effect on secondary velocity profile which are shown in Fig.6.


Fig.4. Secondary velocity profile for various values of $M$
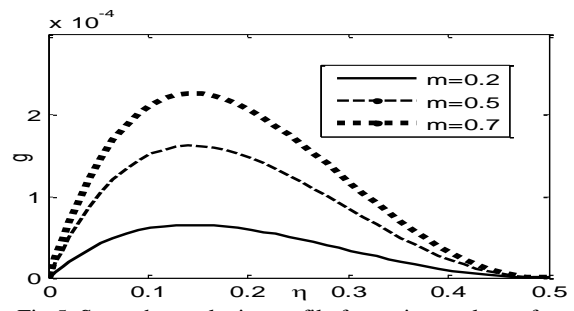

Fig.5. Secondary velocity profile for various values of $m$
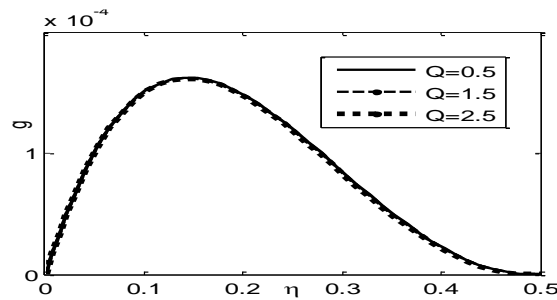

Fig.6. Secondary velocity profile for various values of $Q$

The effect of various parameters on temperature profile are shown in Fig.7-Fig.9. From these figures we see that, the temperature profile is starting at the initial point of the plate surface and increases until it attains the maximum value within the boundary layer and then starts decreasing until it reaches to zero far away from the plate satisfying the boundary condition. Fig.7 shows the temperature distribution for different values of the magnetic parameter $M$ and observed that the thermal boundary layer decreases as $M$ increases adjacent to the surface of the plate and the effect is not significant far away from the plate. Fig. 8 which illustrate the effect of Prandtl number $Pr$ on the temperature profile. From this figure it is observed that the temperature decreases with an increase in the Prandtl number, which implies viscous boundary layer is thicker than the thermal boundary layer. From these plots it is evident that large values of Prandtl number result in thinning of the thermal boundary layer. In this case temperature asymptotically approaches to zero in free stream region. Fig.9 indicates the variation of heat generation parameter and it is noticed that the thermal boundary layer increased up to certain values of eta and then decreased far from the plate.
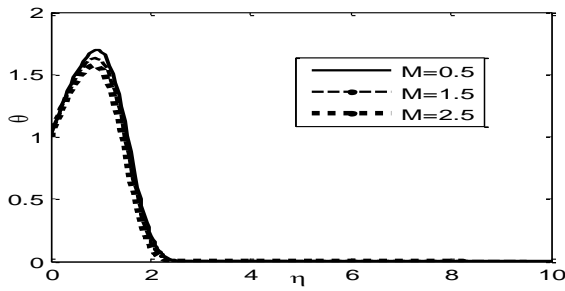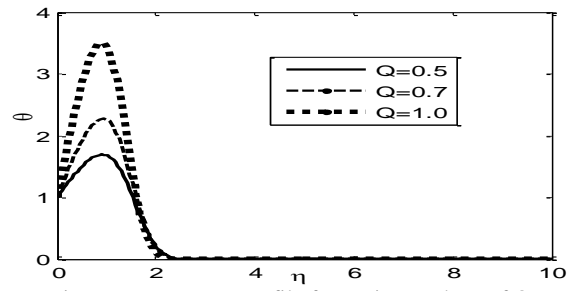
Fig.7. Temperature profile for various values of M


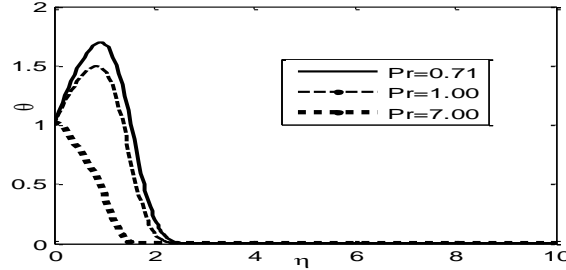Fig.9. Temperature profile for various values of Q


Fig.8. Temperature profile for various values of *Pr*

Fig. 10- Fig. 12 shows the concentration profiles obtained by the numerical simulation for various values of entering non-dimensional parameters. In Fig. 12 the effect of *Sc* is found to decrease the concentration because increasing in *Sc* decreases molecular diffusivity which result a decrease of the boundary layer. Hence the concentration of the species in lower for large values of *Sc*. From the Fig. 10 and Fig.11 it is observed that, the negligible decreasing and increasing effect on concentration profiles for increasing values of *M* and *Q*.
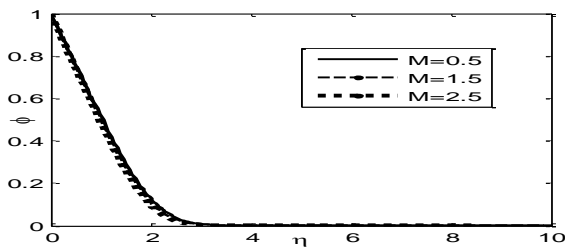

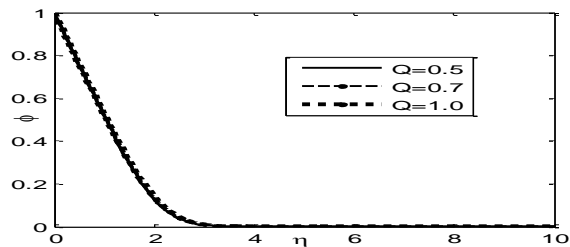Fig.10. Concentration profile for various values of *M*


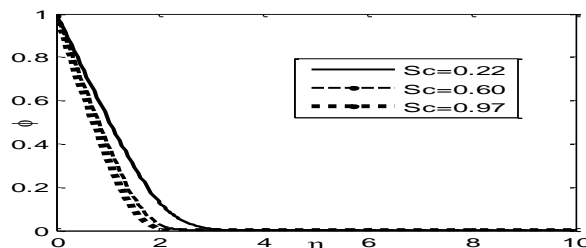Fig.11. Concentration profile for various values of *Q*


Fig.12. Concentration profile for various values of *Sc*

Again, from Table 1 it is observed that the skin friction is decreased for magnetic parameter and increased for heat generation parameter & Prandtl number. The rate of heat transfer is increased for magnetic parameter and Prandtl number as a result the thermal boundary layer is decreased but the reverse result arises for heat generation parameter. Again, the rate of concentration is increased for magnetic parameter and Schmidt number as a result the concentration boundary layer is decreased but reverse case arises for heat generation parameter. Table 2 show the compared result and found to be in good agreement between the numerical results of skin friction coeffient and local Nusselt number by Runge-Kutta sixth order shooting iteration technique and the results via Keller-Box method of Ishak et al. [7].

**Table 1**. The skin friction $f''(0)$, rate of heat transfer $-\theta'(0)$ and rate of concentration $-\varphi'(0)$ for different values of M, Q, Pr and

**Table 2**. The values of $f''(0)$ and rate of heat transfer $-\theta'(0)$ for different values of M when Pr =1.0, Gr = Gm = 0.5, Sc = 0.22 and

| | | | | | | Sc are respectively. | | | | |
|---|---|---|---|---|---|---|---|---|---|---|

Sc are respectively.

| M | Q | Pr | Sc | $f'(0)$ | $-\theta'(0)$ | $\varphi'(0)$ |
|---|---|---|---|---|---|---|
| **0.5** | 0.5 | 0.71 | 0.22 | -4.5590 | 1.260 | 0.4890 |
| **1.5** | 0.5 | 0.71 | 0.22 | -4.6670 | 1.196 | 0.5030 |
| **2.5** | 0.5 | 0.71 | 0.22 | -4.7720 | 1.140 | 0.5180 |
| 0.5 | **0.7** | 0.71 | 0.22 | -4.5406 | 2.190 | 0.4840 |
| 0.5 | **1.0** | 0.71 | 0.22 | -4.5220 | 3.120 | 0.4808 |
| 0.5 | 0.5 | **1.00** | 0.22 | -4.6721 | 1.070 | - |
| 0.5 | 0.5 | **7.00** | 0.22 | -4.1203 | 0.440 | - |
| 0.5 | 0.5 | 0.71 | **0.60** | - | - | 0.6290 |
| 0.5 | 0.5 | 0.71 | **0.97** | - | - | 0.7100 |

Q = m = 0 respectively.

| | Ishak *et. al.*[7] | | Present results | |
|---|---|---|---|---|
| M | $f'(0)$ | $-\theta'(0)$ | $f'(0)$ | $-\theta'(0)$ |
| 0.0 | 0.5607 | 1.0873 | -0.56513 | 1.0945 |
| 0.1 | 0.5658 | 1.0863 | -0.57035 | 1.0933 |
| 0.2 | 0.5810 | 1.0833 | -0.58421 | 1.0785 |
| 0.5 | 0.6830 | 1.0630 | -0.68538 | 1.0553 |
| 1.0 | 1.0000 | 1.0000 | -1.0043 | 1.0021 |
| 2.0 | 1.8968 | 0.8311 | -1.9004 | 0.9421 |
| 5.0 | 4.9155 | 0.4702 | -4.9206 | 0.4811 |

## 4. Conclusions

The results are presented to display the flow characteristic like velocity, temperature and concentration. Following are the conclusions made from above analysis:

- The magnitude of primary velocity profile decreases with increasing magnetic parameter but reverse result rises in case of heat generation parameter. The noticeable increasing effect of magnetic and Hall parameter on secondary velocity profile are observed primary velocity profile. The thermal boundary layer decreases for *M* and *Pr* adjacent to the surface of the plate and the effect is not significant far away from the plate. The effect of *Sc* is found to decrease the concentration profile because increasing in *Sc* decreases molecular diffusivity which result a decrease of the boundary layer. Hence the concentration of the species in lower for large values of *Sc*.

## 5. References

[1] D.Venkatesulu and U. Rajeswara Rao, "Effect of Hall Currents and Thermo-diffusion on Convective Heat and Mass Transfer flow of a Viscous, Chemically Reacting Rotating Fluid Through a Porous Medium Past a Vertical Porous Plate", *International Journal of Scientific & Engineering Research*, Vol. 4, No. 4, 2013.

[2] Sudha Mathew, P. Raveendra Nath and N. B. V. Rama Deva Prasad, "Hall Effects On Heat and Mass Transfer Through a Porous Medium In a Rotating Channel With Radiation", *Advances in Applied Science Research*, Vol.3, No.5, pp. 3004-3019, 2012.

[3] R. Kumar and K. D. Singh, "Mathematical Modeling of Soret and Hall Effects on Oscillatory MHD Free Convective Flow of Radiating Fluid in a Rotating Vertical Porous Channel Filled with Porous Medium", *International Journal of Applied Mathematics and Mechanics*, Vol. 8, No.6, pp. 49-68, 2012.

[4] W. Ruzicka, "Heat and Mass Transfer Past a Vertical Flat Porous Plate Through a Porous Medium with Variable Thermal Conductivity, Rotation, Soret and Dufour Effects in the Presence of Hall Current", *American Journal of Chemical Sciences*,Vol.2, No.4, 2012.

[5] D. S. Chauhan *and* P. Rastogi, "Hall Effects on MHD Slip Flow and Heat Transfer Through a Porous Medium over an Accelerated Plate in a Rotating System", *International Journal of Nonlinear Science* , Vol.14, No.2, pp.228-236, 2012.

[6] T. Hayat, H. Yasmin, S. Asghar and A. A. Hendi, "Slip effects on Peristaltic Transport in an Inclined Channel with Mass Transfer and Chemical Reaction", *Applied Bionics and Biomechanics*, Vol. 10, No.1, 2013.

[7] A. Ishak, R. Nazar and I. Pop, "Hydromagnetic Flow and Heat Transfer Adjacent to a Stretching Vertical Sheet", *Heat Mass Transfer*, Vol. 44, 921-927, 2008.

# CFD Simulation and Analysis of a UAV

Arif Alam[1*], Mahmud Hossain[1], Md. Sirajul Islam[1], Md. Azizullah Khan[1].
[1]Aeronautical Engineering, Military Institute of Science & Technology.
E-mail: arifalam1729@yahoo.com., aru.mahmud@gmail.com., semonislam@yahoo.com.,
azizullah1992@gmail.com.

## Abstract

*This paper consists of analyzing the lift and drag coefficient of a UAV and also observing the pressure distribution, velocity vector, velocity contour, path-line around the separated parts of the UAV at different angle of attack using CFD Fluent software. To fulfill the purpose the airfoil of wing, airfoil of tail and fuselage are simulated separately. In case of wing and tail the 2-D airfoil is simulated in Fluent and lift and drag coefficient is found at different AOA. Then using 2-D to 3-D conversion formula wing (3-D) and tail (3-D) lift coefficient is calculated. The total Lift coefficient ($C_{LT}$) of the UAV is calculated by adding wing, tail and fuselage lift-coefficient. It is seen from the analysis that at about 8 degree angle of attack the UAV reaches at its maximum lift coefficient. After 8 degree AOA the lift coefficients of the UAV starts to decrease. The start of transition period (flow separation) as a percentage of chord length is also determined using X-foil software. And it is seen that at an increased AOA flow separation occurs more quickly.*

Keywords: Lift co-efficient, velocity vector, Angle of attack (AOA), flow separation, path-line.

## 1. Introduction

For A good UAV design, aerodynamic efficiency of the UAV model is needed to be studied. Aerodynamic efficiency depends on the fluid flow distribution around the model. From it, certain parameters are calculated e.g. lift co-efficient, drag co-efficient, pressure co-efficient, moment co-efficient etc. are used to describe the aerodynamic behavior like boundary layer separation, downwash effect, vortices etc. These parameters are mainly determined by wind tunnel testing and CFD simulation. But to test the UAV model, the available wind tunnel in the laboratory does not provide accurate data for certain limitations e.g. calibration problem, unavailability of full scale wind tunnel etc. For this reason, CFD simulation of the UAV model is performed to determine these parameters.

CFD is based on Navier-Stokes equations, nonlinear PDEs, which are used to express the relationship among the velocity, pressure, temperature, and density of any fluid flow. In this paper the simulation of fluid flow around the airfoil and fuselage that is used for Unmanned Aerial Vehicle (UAV) model is illustrated and to calculate total lift coefficient. Any aerial vehicle which is used or intended for flight without on board pilot is called Unmanned Aerial Vehicle. As its name implies, it is capable of sustained flight in the atmosphere without the traditional pilot, it is controlled either remotely or automatically. It is used for various purposes. UAV includes airplanes, helicopters, airships, and powered–lift aircraft without an onboard pilot. Traditional balloons, rockets, tethered aircraft and un-powered gliders are not included in UAV.

For the CFD simulation of our UAV model, two airfoils are used-

  a)  NACA-4412 for wing.

  b)  NACA-0012 as for horizontal and vertical tail.

## 2. Theory

**Lift Equation:**

$$L = 1/2 * \rho V^2 C_L A \qquad (1)$$

**Drag Equation:**

$$D = 1/2 * \rho V^2 C_D A \qquad (2)$$

**Reynolds Number:**

$$Re = \rho V L / \mu \qquad (3)$$

**The approximate relating equation between wing lift and airfoil lift is-**

$$C_L \text{ (wing)} = 0.9 C_{l\,max}\text{(airfoil)} * cos^0.25c \qquad (4)$$

**As there is no sweep angle in the experimented UAV. So,**

$$C_L = 0.9 C_{lmax} \qquad (5)$$
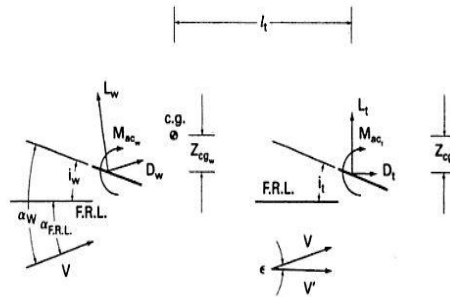
**Tail Contribution**



Fig.1. Aft tail contribution to the pitching moment

Now, angle of attack for tail,

$$\alpha_t = \alpha_w - i_w - \text{€} + i_t \qquad (6)$$

Here,

$$\text{€} = 2C_{LW}/ (\pi.\ AR_w) \qquad (7)$$

## 3. Methodology & Various Steps

### 3.1 Geometry Setting

**The 2-D airfoil (NACA0012 and NACA 4412) setting:**

The co-ordinate file of the airfoil is imported into the Design Modeler.

The chord length: NACA 0012 (for tail) = 0.4m and NACA 4412 (for wing) = 1m.

C-domain is drawn around the airfoil and divided into six surfaces. C-domain is taken as it is convenient for the air flow around the airfoil and flow enter into the domain in all direction.

**The 3-D fuselage setting:**

The 3-D fuselage is drawn in ICEM CFD. The fuselage is cylindrical shape which Diameter = 0.6m and Length = 5m.A rectangular shape domain is drawn around the fuselage. The distance of the front surface and the rear surface of the domain is taken about 3 times greater than the fuselage from the leading and trailing edge of the fuselage. The distance of the upper and lower surface of the domain from the fuselage is taken about 10 times greater than the diameter of the fuselage.

### 3.2 Mesh Setting

For 2-D airfoil (NACA 0012 and NACA 4412) Structured Grid C-mesh is used. In edge sizing number of divisions is taken as 50.And Bias factor is taken 50.Bias Type is at an increment rate at the leading edge and at a decrement rate from the tailing edge of the airfoil.

For fuselage volume mesh is used in and mesh type is tetrahedral in all domains. Prisms mesh is used surrounding the fuselage.
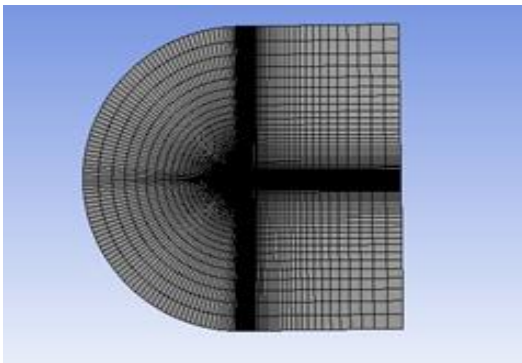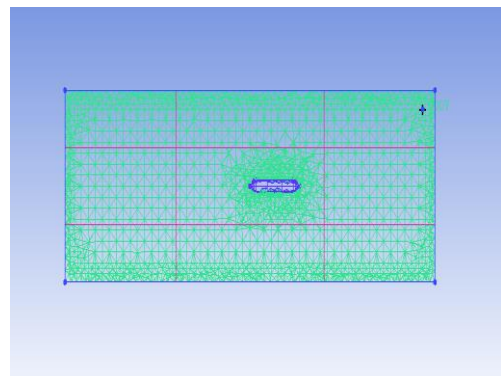


Fig.2. Mesh of 2-D airfoil NACA-0012



Fig.3. Fuselage mesh with domain
(Cut plane)

### 3.3 Solution Setup

**Table 1**. Solver settings

| CFD Simulation | 2-Ddouble precision (3-D double precision) |
|---|---|
| Solver | Fluent |
| 2d Space | Planar |
| Velocity Formulation | Absolute |
| Time | Steady |
| Type | Pressure-based |

**Table 2.** Viscous model and turbulence model settings

| Turbulence model | k-epsilon (2 equation) |
|---|---|
| k-epsilon Model | Standard |
| Near-Wall Treatment | Standard  wall Function |
| Operating Conditions | Ambient |

**Table 3.** Boundary condition settings

| Velocity Inlet | Velocity specification method | Component |
|---|---|---|
| | Reference Frame | Absolute |
| | Turbulence specification method | Intensity and Viscosity Ratio |
| | Turbulent Intensity | 5 % |
| | Turbulent Viscosity Ratio | 10 |
| Pressure Outlet | Gauge Pressure magnitude | 0 Pascal |
| | Backflow direction specification method | normal to boundary |
| | Turbulence Specification Method | Intensity and Viscosity Ratio |
| | Backflow Turbulence Intensity | 5 % |
| | Backflow Turbulent Viscosity Ratio | 10 |
| Wall zones | Wall motion | Stationary wall |
| | Shear condition | No slip |
| | Wall Roughness height | 0 |
| | Wall Roughness constant | 0.5 |
| Fluid Properties Air | Fluid Type | Air |
| | Density<br>Kinematic viscosity | $\rho = 1.225$ (kg⁄m^3 )<br>$v = 1.7894 \times 10^{\wedge}(-5)$ (kg⁄(m·s)) |

**Table 4.** Solution controls

| Equations | Flow and Turbulence |
|---|---|
| Discretization | a.  Pressure: Standard<br>b.  Momentum: Second Order Upwind<br>c.  Turbulence Kinetic Energy: First  Order Upwind<br>d.  Turbulence Dissipation Rate: First  Order Upwind |
| Monitor | Residuals & Drag and Lift Coefficient |
| Convergence   Criterion | - Continuity = 0.00001<br>- X-Velocity = 0.00001<br>- Y-Velocity = 0.00001<br>- k = 0.00001 |

## 4. Results and Discussion:

Reynolds Number is approximately $2.05*10^6$ (using eqn. 3). So the flow is turbulent.

The $C_l$ and $C_d$ for NACA-4412, NACA- 0012 and fuselage are obtained by simulation in ANSYS Fluent solver. Then the 2-D lift coefficient of the airfoils is converted into 3-D lift coefficient by using equation 5. All three (wing, tail, fuselage) lift coefficient is then added to calculate total lift coefficient for the UAV.

Initial angle of incidence for wing is 1 degree and for tail is 0 degree. Effective AOA is calculated using 6 & 7 equations.
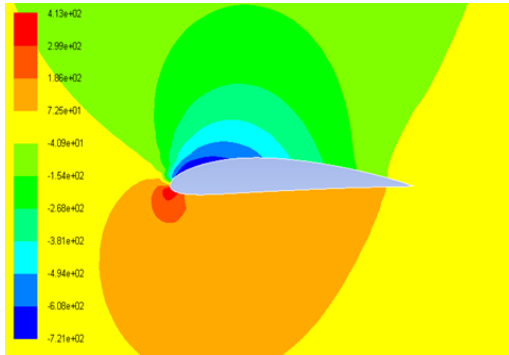


Fig.4. Pressure Contour at 4 degree AOA
(Effective AOA 5 degree) (Naca-4412)
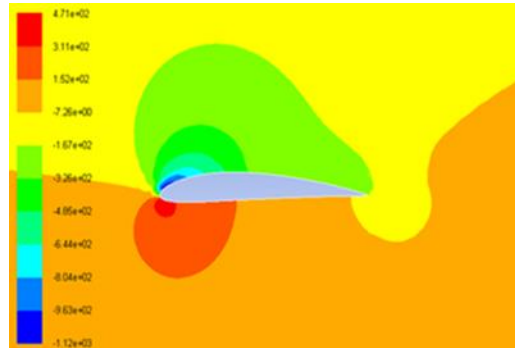


Fig.5. Pressure Contour at 10 degree AOA
(Effective AOA 11 degree) (Naca-4412)

From the fig. it is seen that at an increased AOA pressure on the lower surface increases as well as pressure on the upper surface decreases. Here, red color means higher pressure.
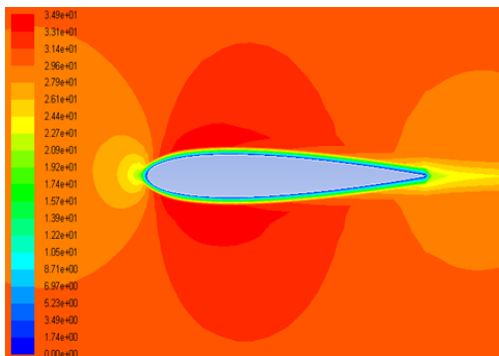


Fig.6. Velocity Contour at 2 degree AOA
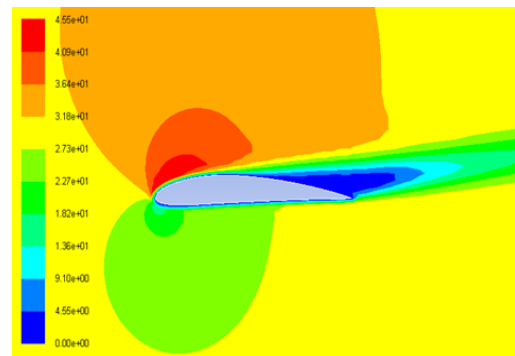(Effective AOA -0.412 degree) (Naca-0012)



Fig.7. Velocity Contour at 10 degree AOA
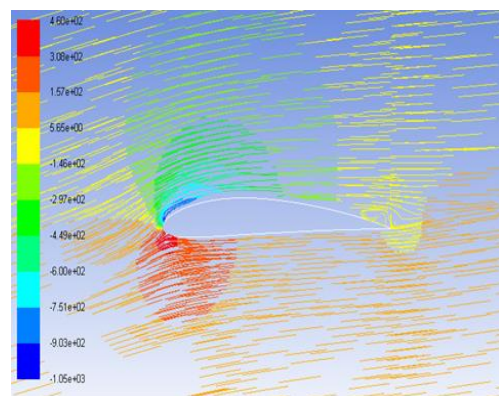(Effective AOA 11 degree) (Naca-4412)



Fig.8. path-line at 8 degree AOA
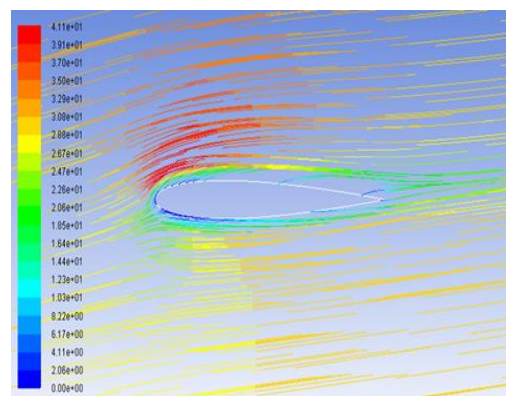(Effective AOA 9 degree)  (Naca-4412)



Fig.9. path-line at 10 degree AOA
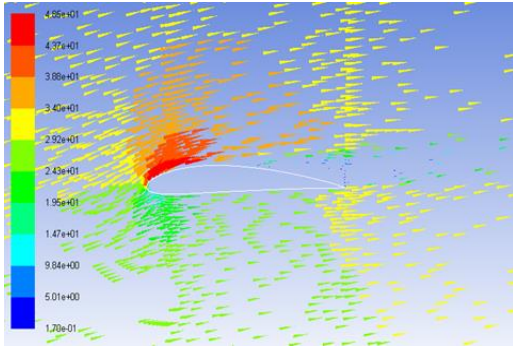(Effective AOA 7.429 degree)  (Naca-0012)

Fig.10. Velocity Vector at 10 degree AOA (Effective AOA 11 degree) (Naca-4412)
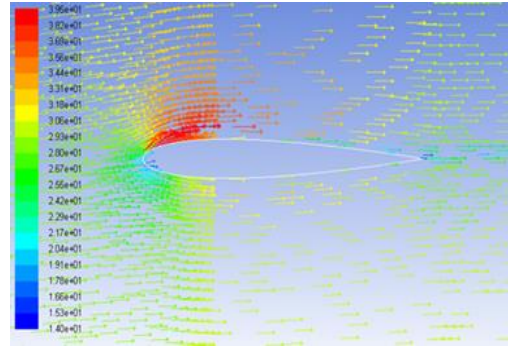


Fig.11. Velocity Vector at 6 degree AOA (Effective AOA 3.439 degree) (Naca-0012)

It is seen from the above figures that at a higher AOA velocity at the upper surface of the airfoil increases and at the lower surface decrease. And from fig. 7 & 10 it is clear that at a higher AOA air flow separates from the surface quickly which gradually causes to stall.

In fig. 8 & 9 air is circulating anti-clockwise which is called vortex Starting vortex is created in the air adjacent to the trailing edge. It leaves the airfoil and remains stationary in the flow. Downwash effect is occurred in the trailing edge which reduces lift and increase drag.
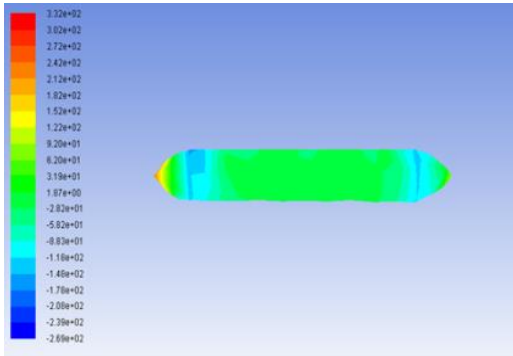


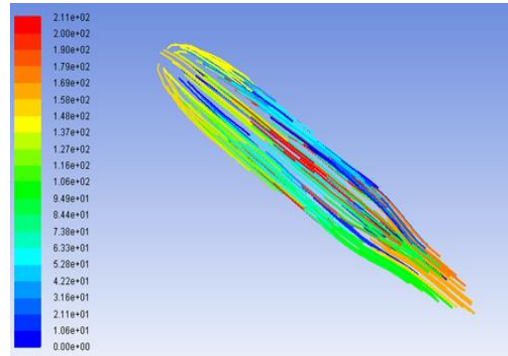Fig.12. Pr. contour of fuselage at 6 deg. AOA



Fig.13. Path line of fuselage at 10 deg. AOA

The incidence AOA of the fuselage is zero. So the change of pressure distribution, velocity distribution, path line around the fuselage does not show too much change. For this reason the lift coefficient of the fuselage is very small. As a result the fuselage has less contribution to the generation of lift force of the UAV.

**Table 5.** The start of Transition period for NACA-4412 determined by X-foil

| AOA | Transition period starts (% of chord length) |
|-----|-----|
| 0 | 44.12% |
| 2 | 41.22% |
| 4 | 33.84% |
| 6 | 12.92% |
| 8 | 6.7% |
| 10 | 2.45% |

**Table 6.** The start of Transition period for NACA-0012 determined by X-foil

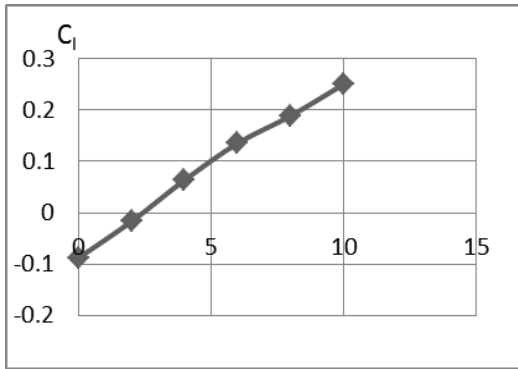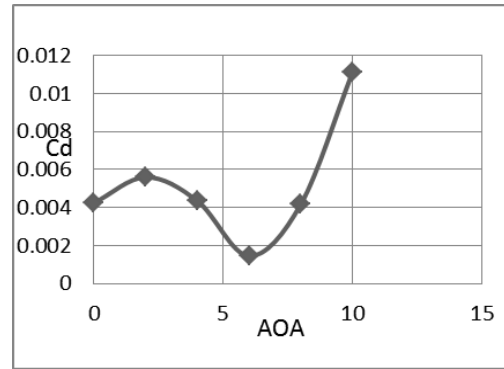| AOA | Transition period starts (% of chord length) |
|-----|-----|
| 0 | 75.79% |
| 2 | 59.15% |
| 4 | 39.57% |
| 6 | 19.91% |
| 8 | 5.84% |
| 10 | 2.47% |

Fig.14. $C_l$ vs. AOA for NACA-0012



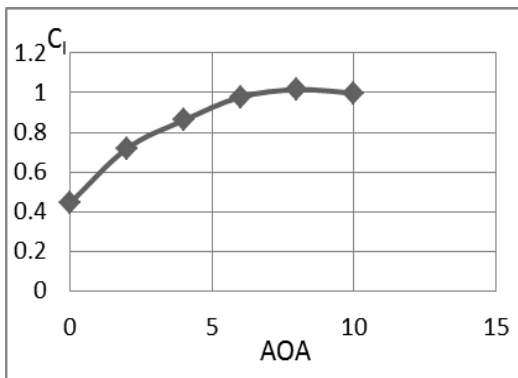Fig.15. $C_d$ vs. AOA for NACA-0012



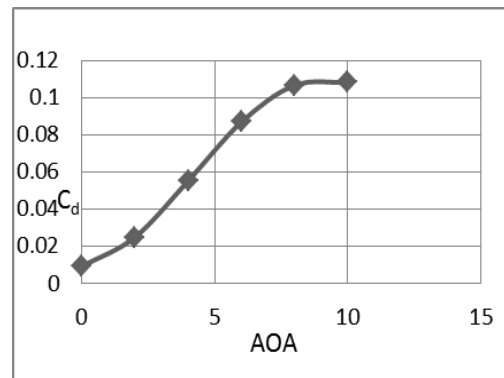Fig.16. $C_l$ vs. AOA for NACA-4412
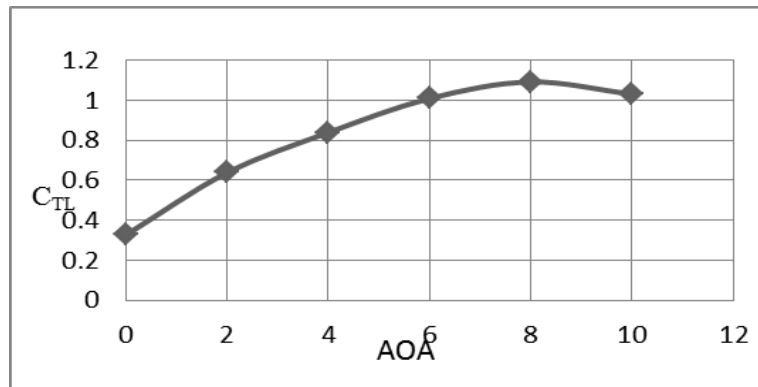


Fig.17. $C_d$ vs. AOA for NACA-4412



Fig.18. $C_{TL}$ vs. AOA for total UAV

## 5. Conclusion

Max total calculated Lift-Coefficient of the UAV is 1.0915 at 8 degree AOA. After this the Lift coefficient of the UAV decreases and drag increases. As the speed of the UAV is lower that's why stall happens at a lower AOA.

For the vertical stabilizer of the UAV NACA-0012 airfoil is used. As the contribution of the vertical tail to the lift-coefficient of the UAV is too small, so the lift coefficient of the vertical tail is neglected.

## 6. References

1. Aircraft Design: A Conceptual Approach (Fourth Edition) – by Daniel P. Raymer
2. Aerodynamics – by L J Clancy
3. Computational Fluid Dynamics – by John D. Anderson, Jr
4. Aircraft Performance – by John D. Anderson Jr.
5. Airplane Performance, Stability and Control – by Courtland D. Perkins.

*Paper ID: FM-07*

# Comparative Study of Tara Dev and Hybrid Tara Pump with Respect to Water Level in Rajshahi

S.S.Tuly[1], M.S. Zaman, M.R. Islam
Department of Mechanical Engineering
Rajshahi University of Engineering & Technology, Rajshahi-6204, Bangladesh
[1]E-mail**:**tulyruet@yahoo.com

## Abstract

*Hand pump technology is considered as being the best option for the water supply of rural communities in the developing countries. In this work, comparative study of Tara Dev and Hybrid Tara pump has been done with respect to ground water levels for different seasons in Rajshahi. Generally in Rajshahi the maximum and minimum depth of ground water levels are found in the month of March–May and August–October, respectively. The pumps have been experimented for static ground water level in between 56 ft to 16 ft. Different parameters such as water level, pump discharge, force required for pumping have been measured for both Tara Dev and Hybrid Tara pump and a comparison has been made between the two pumps. Maximum discharge by using Tara Dev pump was 35 lit/min and minimum discharge was 23 lit/min when uPVC pipe was used as buoyant rod. Under same situation, the maximum and minimum discharges in Hybrid Tara pump were 30 lit/min and 17 lit/min respectively. Hybrid Tara delivers water with lower values of applied force than that of Tara Dev pump. All of the users felt much interest for Hybrid Tara pump instead of Tara Dev for their household water uses. Due to good user acceptance, easy lifting, easy serviceability, lower force required during pumping, simple mechanism and low cost, Hybrid Tara has been selected as better option for household water supply in rural area.*

Keywords**:** Ground water level, Hybrid Tara pump, Rural area, Tara Dev pump

## 1. Introduction

 In Bangladesh, ground water is the predominant source of water supply. Hand pump tube wells lift the ground water and supply it in rural areas. Millions of people (principally women and children) spend a major amount of their daily lives fetching water. In many cases, the water comes from unprotected sources such as surface water. Hand pump technology was developed to lift ground water which sometimes holds huge quantities of safe water. Hand pumps, which are close to communities and offer access to safer fresh water, were considered to be the solution to improve children's education and allow a better quality of life for women. Their simplicity and ease of use were regarded as particularly major advantages as it was reported that human power was the most reliable and readily available source of energy for water lifting in the developing world.

Now-a-days water supplying with hand pump tube wells are facing severe problems due to various reasons and the major reason is the lowering of water table. In addition to the many places in the world where water tables are naturally very deep, increasing demography and global warming also have major impacts on ground water levels [1].In this case Tara Dev and Hybrid Tara hand pumps are very important because these pumps are cost effective, their discharge is also high and are able to operate at very deep water level. These hand pumps are Lever Action Pumps. When the static ground water level lowers down to an approximate depth of 35 ft, the manually operated suction type pump ceases to function, leading to stoppage of water lifting for human use. To combat such critical situation an idea was developed for a model pump named Hybrid Tara imposing some modifications on existing Tara Dev pump, in the portions of pump head and buoyant rod. Both of the existing Tara Dev and Model Hybrid Tara are manually operated pumps. But the former have some operational difficulties and limitations. In order to assess the superiority between Hybrid Tara and Tara Dev, these pumps were operated under different conditions throughout the year.

## 2. Fluctuation of monthly water levels in Rajshahi

Now-a-days groundwater crisis of Rajshahi area is highlighted. Water plays an important role in development of agricultural facilities in all parts of the world. Ground water condition of an area is mainly depending on geology, hydrology, hydrologic parameter, soil properties, recharge and discharge, hydraulic characteristics of aquifer. An important component of water balance equation is ground water recharge. This report focuses mainly on the performances of the Tara Dev and Hybrid Tara pump with ground water fluctuation and the trend of ground water level fluctuation in Rajshahi as well as to select the best performing pump. The vertical change in storage is not same throughout the year due to rainfall and infiltration for characteristics of soil in study area. The monthly fluctuation of ground water level at two different sites in Rajshahi district for five years is shown in Figs. 1 and 2. The maximum and minimum depth of water table are found in month of March–May and August–October respectively. Monthly variation of rainfall follows the usual pattern of monsoon with heavy rains from June to September [2].Global ground water storage is roughly equal to the total amount of fresh water stored in the snow and ice pack, including the north and south poles. This makes it an important resource which can act as a natural storage that can buffer against shortages of surface water, as in during times of drought. Ground water makes up about 20% of the world's fresh water supply, which is about 0.61% of the entire world's water, including oceans and permanent ice [3]. The increase of ground water can be achieved by infiltration of rainfall, recharge by seepage, surface flow etc. In order to maintain ground water supplies indefinitely the hydrological equilibrium must exist between all water entering and leaving the basin. The management of ground water is essential to obtain desired economic benefits. Maximum economic and beneficial use can be obtained by coordinating ground water and surface water resource. The proper management of ground water resources requires an adequate knowledge of extent of the storage, the rate of discharge, the rate of recharge to ground water body as well as the use of economical means of extraction [4].
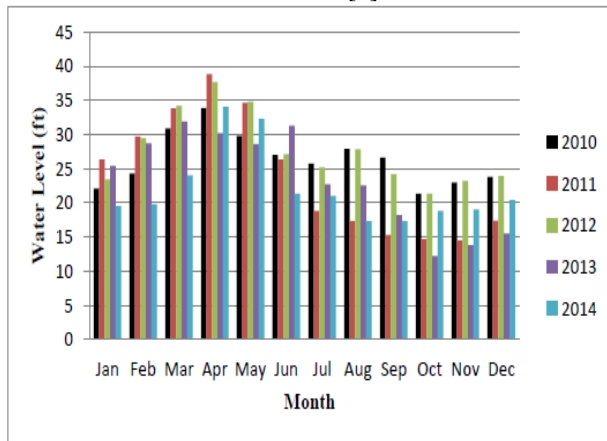


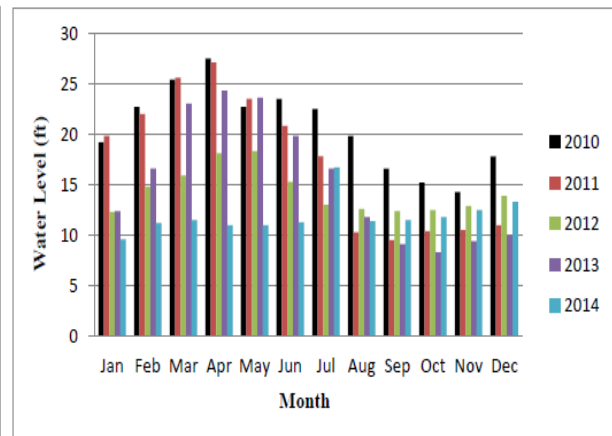**Fig.1.** Fluctuation of ground water level in Kathalbaria mouza, Puthia, Rajshahi

**Fig.2.** Fluctuation of ground water level in Bajubagha mouza , Bagha, Rajshahi

## 3. Differences between Tara Dev and Hybrid Tara Pump

Tara hand pump is a low-lift, direct action hand pump developed in Bangladesh using concepts that are now proving to be suitable for community water supply applications in other developing countries. Considering the problem encountered in rural water supply a technical committee comprising experts from different organizations started their work on Research and Development activities before 1982. Because of water table depletion, hand pump other than suction plunger hand pump was very essential to be introduced in Bangladesh. After a series of discussions, workshop and field verification, Tara hand pump technology for low water table area has been developed in Bangladesh in the year of 1984.Considering the importance and the magnitude of the Research & Development (R&D) activities, it was felt necessary to establish a separate setup of manpower to be engaged in Research & Development activities. Accordingly, the Research and Development Division of Department of Public Health Engineering (DPHE), was created in 1989 under GOB-Unicef project. The design of the pump has been developing since the first prototypes were produced in July1982, and at each stage the tara has been subjected to comprehensive testing both in the laboratory and in field trials [5]. Tara technology having lever action pump is termed as Tara Dev. Both Tara Dev and Hybrid Tara are lever action pumps. They operate on the same principles but they have some structural differences.Fig.3 shows the main components of Tara Dev pump.

In some cases, facing acute lowering of water level Tara Dev pump is not suitable. At this condition a new pump named Model Hybrid Tara has been developed by imposing some modification in the areas of pump head and buoyant rod .The pump head in Tara Dev is made of mild steel and in Hybrid Tara it is made of cast iron. Both Tara Dev and Hybrid Tara pumps were taken under experiment with two different sets of buoyant rod namely uPVC (Unplasticised Polyvinyl Chloride) pipe and PVC (Polyvinyl chloride) pipe. All other accessories for both of the sample pumps are same in design and operation.
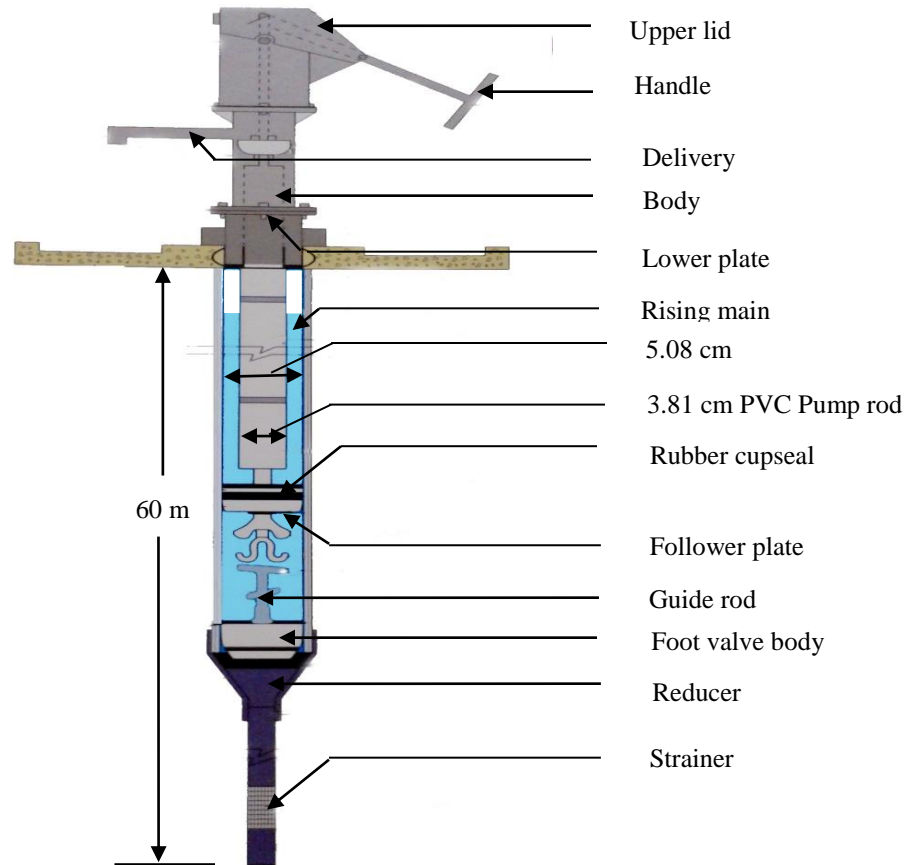


**Fig.3.** Main components of Tara Dev pump

**Table 1.** Distinctive features of Tara Dev and Hybrid Tara Pump

| Components | Existing Tara Dev | Model Hybrid Tara |
|---|---|---|
| Pump head material | Mild Steel | Cast Iron |
| Weight of pump head | 26.50 kg | 24 kg |
| Stroke length | 22 cm | 20 cm |
| Dimension of the cylindrical body | ID = 8 cm , OD = 8.60 cm<br>Height = 45 cm | ID = 8.80 cm ,OD = 10.18 cm<br>Height = 50 cm |
| Buoyant rod | (i) PVC pipe with weight 5.58 gm/cm, ID = 3.81 cm, OD = 4 cm, Total length = 19.81 m<br>(ii) uPVC pipe with weight 4.10 gm/cm, ID = 1.91 cm, OD = 2.54 cm, Total length = 19.81 m | (i) PVC pipe with weight 5.58 gm/cm, ID = 3.81 cm, OD = 4 cm, Total length = 19.81 m<br>(ii) uPVC pipe with weight 4.10 gm/cm, ID = 1.91 cm, OD = 2.54 cm, Total length = 19.81 m |

## 4. Experimentation on Tara Dev and Hybrid Tara Pump

In this experiment, the fluctuation of ground water level was recorded for the place located inside the RUET campus near Talaimari in Rajshahi. During the experiment different parameters such as ground water level, pump speed, pump discharge, force required for pumping were measured. The depth of static ground water level was measured directly by a graduated tape. During the operation of the pump, number of strokes were counted for a fixed time period. The time was recorded by a stopwatch. The pump speed (stroke/min) was determined by dividing the number of strokes by the time spent. A graduated bucket was filled for a known period of time. Pump discharge in (litre/min) was calculated by dividing the amount of water by the measured time. Force required for pumping was measured by using force meter in Newton. The parameters were determined for the two pumps with varying water level in different seasons for different operators and a comparison between the performances of the pumps were made. The tendency of a fluid to uplift a submerged body because of the upward thrust of the fluid is known buoyancy. In this study buoyancy force was calculated using the following equations:

$$\text{Buoyant force, } F_B = V\gamma \qquad (1)$$
$$\text{Volume of water displaced, } V = \pi r^2 L_s \qquad (2)$$

Where, r = radius of the buoyant rod which was 0.009525 m for uPVC pipe and 0.01905 m for PVC pipe.
L = length submerged in water which was 9.144 m when ground water level was 10.67 m
Unit gravity force of water, $\gamma$ = 9806 N/m$^3$
Theoretical value of effort was found from lever principle using the following equation:
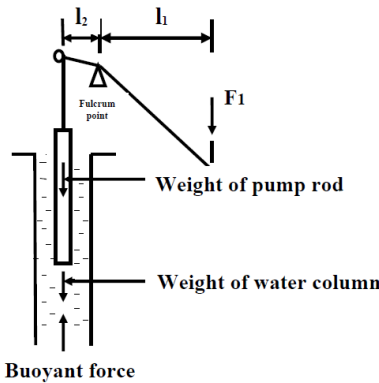
$$F_1 = (F_2 l_2) / l_1 \qquad (3)$$



**Fig.4.** Lever principle in hand pump

Where, $F_1$= effort in Newton, Pumping load, $F_2$ = (Weight of water column + Weight of pump rod) in Newton
$l_1$= horizontal distance from effort to fulcrum in meter, $l_2$= horizontal distance from load to fulcrum in meter
When ground water level was 10.67 m (using uPVC pipe), the value of $F_1$ was found 91N from force meter and that was found 81.5 N from equation (3) .



**Fig.5.** Operation of Tara Dev by a 29 years old male operator



**Fig.6.** Operation of Hybrid Tara by a 29 years old male operator

Figs.5 and 6 show the operation of the two pumps (Tara Dev and Hybrid Tara) by a male operator when ground water level was 47 ft. In this case the discharge obtained by Tara Dev and Hybrid Tara pumps were 35 lit/min and 30 lit/min respectively when uPVC pipe was used as buoyant rod and the force required for pumping was 100 Newton for Tara Dev pump and 92 Newton for Hybrid Tara pump. For the same operator, using PVC pipe, the discharge was 32 lit/min for Tara Dev pump and 28 lit/min for Hybrid Tara pump and the pumping forces were 110 Newton and 95 Newton respectively.

## 5. Results and discussion

Both of the sample pumps were experimented for static ground water level in between 15 ft to 56 ft. The readings of water levels were taken for two times in each month. In Rajshahi the maximum and minimum depth of ground water levels are found in the month of March–May and August–October, respectively.
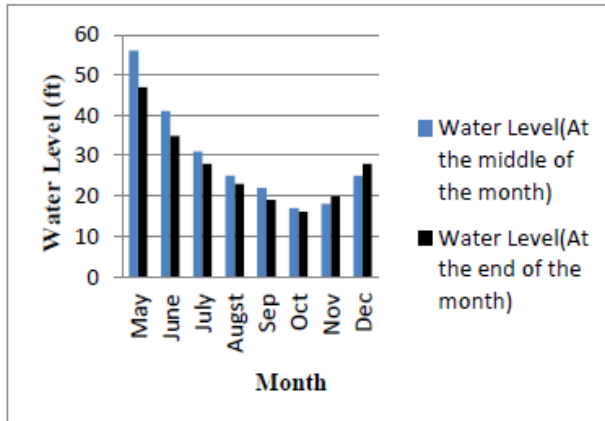


**Fig.7.** Fluctuation of ground water level at the selected site
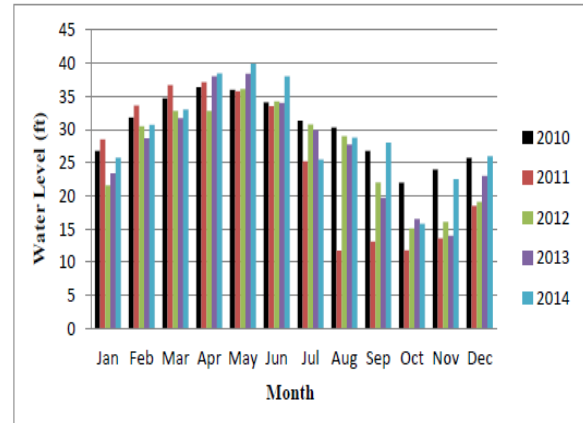


**Fig.8.** Fluctuation of ground water level for five years at Shantoshpur, Paba, near the site

From Figs.7 and 8 similar results are found. For both places, the maximum value of ground water level fluctuation was recorded in the month of May and the minimum value was found in October. In this study, better performance was obtained by the Model Hybrid Tara pump while uPVC pipe was used as buoyant rod. The performance obtained from experimental study on the both existing Tara Dev pump and Model Hybrid Tara pump are shown in Figs.9-12. It was found by the experimental investigation that the Hybrid Tara shows better result with respect to comfort level and operating force but discharge is slightly less than Tara Dev pump. The results are also greatly affected by the static ground water level, type of operator and operation mode of the respective people for both pumps. The Model Hybrid Tara pump gives discharges with lower values of applied force than Tara Dev pump due to less weight and diameter of the buoyant rod, and simplicity in mechanism.
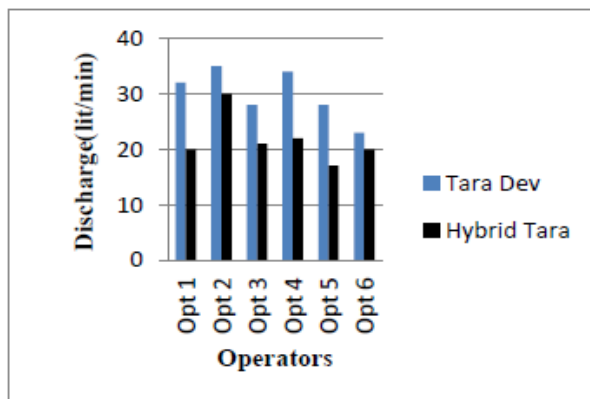


**Fig.9.** Water supply rate by Tara Dev and Hybrid Tara Pumps with respect to pump operators
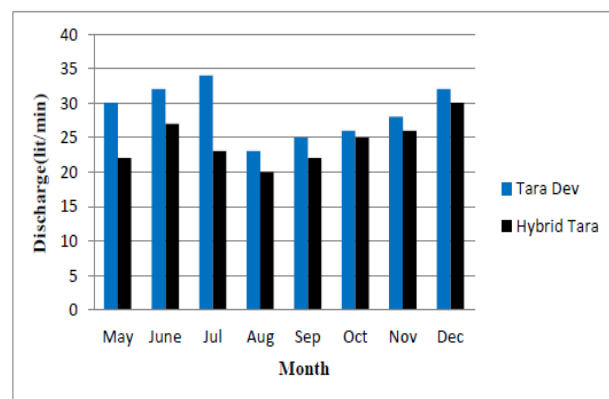


**Fig.10.** Discharge obtained for the same operator over the whole time period (May-December)

Fig.9 shows the difference in discharge between Tara Dev and Hybrid Tara pump for different operators. On the other hand, Fig.10 shows the discharge obtained for the same operator. In both cases, higher discharge is found from Tara Dev pump than that of Hybrid Tara.Figs.11 and 12 show the force versus operator curve using uPVC pipe and PVC pipe respectively.
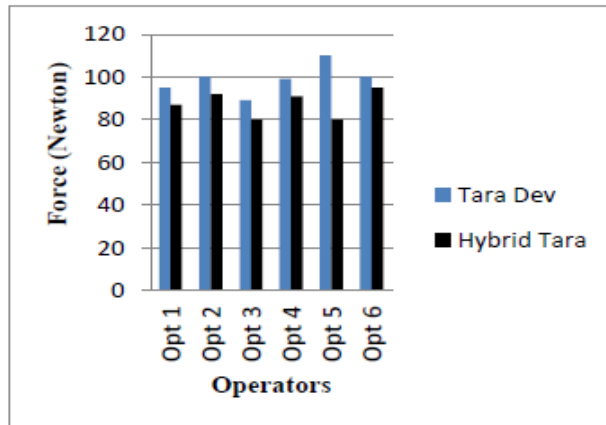


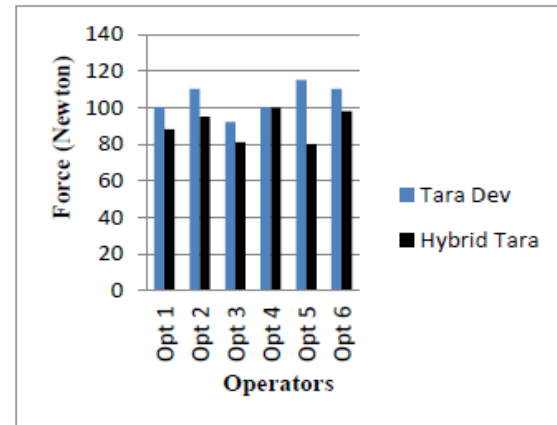**Fig.11.** Force Vs Operator curve using uPVC pipe



**Fig.12.** Force Vs Operator curve using PVC pipe

The value of applied force is found directly from the force meter. But the theoretical value of applied force is 10.4% less than the practical value.

All of the users have been feeling much interest for Hybrid Tara pump instead of Tara Dev for their household water. Thus Hybrid Tara pump can be selected as better performing pump because of it's-

- Good user acceptance
- Easy lifting
- Easy serviceability, minimum downtime
- Simplicity in mechanism and
- Low cost

## 6. Conclusions

- The comparative study of the two pumps reveals that higher discharge is found from Tara Dev pump.
- Hybrid Tara delivers water with lower values of applied force than Tara Dev pump.
- Because of easy lifting and simplicity in mechanism, Hybrid Tara has been accepted as better performing pump by all the operators.

## 7. References

[1]  L. Cornet, BSc, M. Hann, BSc, MSc, PhD, CEng FIAgrE"A Comparative Evaluation of Ultra Deep-Well  Handpumps"

[2]  International Journal of Civil & Environmental Engineering IJCEE-IJENS Vol: 13 No:02 H. M. Rasel, M. R.  Hasan, B.Ahmed and M. S. U. Miah" Assessment of Ground Water fluctuation and Recharge due to rainfall in Barind Area under Greater Rajshahi District (North Western Part of Bangladesh)".

[3]  M. Asaduzzaman , BARIND TRACT " Rajshahi Ground Water Exploration Follow-  Up Report (1983)"

[4]  K. H. Nasir Hassan (BUET) "Ground water level fluctuation and loss or gain of ground water storage of Dhaka city".

[5]  www.dphe.gov.bd/index.php

# Numerical Investigation of Aerodynamic and Structural Performance of a Centrifugal Compressor

Roohany Mahmud[1], Rofiques Salehin[2], Wing Commander S A Savanur[3]

[1,2,3]Department of Aeronautical Engineering
Military Institute of Science & Technology (MIST)
Mirpur Cantonment, Dhaka-1216, Bangladesh
E-mail: roohany.mahmud@gmail.com[1], rsalehin92@gmail.com[2], shrinisavy@gmail.com[3]

## Abstract

*Centrifugal compressors with high pressure ratio are generally used in turbochargers and turboshaft engines because of their small dimensions, high efficiency and wide operating range. By understanding the flow phenomena we can largely improve the performance of a high pressure ratio centrifugal compressor. In this paper, the flow field in a centrifugal compressor of expected pressure ratio of almost 1.83 with a vaneless diffuser has been investigated numerically on the design point. A finite-volume based CFD solver is used in this purpose. Furthermore, the temperature and pressure loads obtained from aerodynamic analysis are used to simulate the structural stresses and deformations on the blade body. This structural performance is assessed with and without the presence of rotational velocity of the addressed centrifugal compressor. Finally, the authors hope that this paper will help the future designers about upgrading aerodynamic performance of a centrifugal compressor within structural limitations in mind before going for the final design and manufacturing.*

Keywords: Centrifugal Compressor, Impeller, Tip Speed, Relative Mach number

## 1. Introduction

Centrifugal compressors are generally designed to transfer energy from a set of rotating impeller blades to the gas. The term "centrifugal" implies that the gas flow is radial, and the energy transfer is caused from a change in the centrifugal forces acting on the gas. Centrifugal compressors deliver high flow capacity per unit of installed space and weight, have good stability, better resistance and less susceptibility to the loss of performance. Moreover, they require significantly less maintenance than axial compressors. Centrifugal compressor are still in used for wide variety of products ranging from small commuter aircraft to large industrial petrochemical compressor stations. To make a low weight and small size centrifugal compressors the designers generally stick with two principles during designing: 1) To increase the compressor's specific speed to reduce the rotor exit diameter and thus to reduce the weight and size in a specific stage, 2) To increase the pressure ratio in a stage to reduce the requirement of number of stages which, in turn, will reduce the machine's weight and size. But this gives rise to a problem, i.e., the increase in Mach number in the flow inside the machine. Centrifugal compressors with transonic Mach number levels often has low efficiencies which may be due to the impact of shocks and shock/boundary layer interactions on rotor and diffuser flow.

The main objective of this paper is to demonstrate a complete computational fluid dynamics (CFD) analysis of a three-dimensional centrifugal compressor within geometric and flow constraints. The study will highlight the different important flow characteristics at different regions of the compressor parts. Finally, a structural effect on the solid body of the impeller due to the generated temperature and pressure load is described.

## 2. Numerical Aspects

The Navier-Stokes equations for steady-state flow in their conservation form is solved for the computational fluid dynamic analysis. Three transport equations of mass, momentum and energy in conservation form and two constitutive equations of state for density and for enthalpy are summed up to form a closed system. The turbulence model used here is k-epsilon which is used often in industrial applications and has very good convergence behavior. The structural analysis of the impeller is done for a linear isotropic material – structural steel. Finite element method (FEM) is adopted for the static structural analysis of the 3-D impeller system. As the main objective of the paper is show the CFD and structural analysis results, so we will not discuss about the fundamental governing equations and property relations, as they can easily be found in[1,2].

# 3. Computational model of the centrifugal Compressor

## 3.1. Case model

For the current analysis, we consider a centrifugal compressor which will operate on average sea-level pressure and temperature (design point). The expected pressure ratio is 1.83 at a mass-flow rate of 0.3 kg/s through the machine rotating at 60000 rpm. Moreover, it is assumed that the compressor has a hub and shroud diameter of 30 mm and 60 mm respectively. The compressor impeller consists of nine main blades and nine splitter blades with backsweep angle of $45^0$. For the impeller blade sets, the vane normal thickness at hub and at shroud is assumed 1.8 mm and 0.5 mm respectively. The axial tip clearance is 0.03 mm. From these assumed values, we can calculate the flow coefficient, tip width, flow angles and specific speed by iterative process. Thus, we can create 3-D geometry of the compressor impeller. The splitter blades have the same geometric characteristics like the main blades. The material used for the structural analysis is structural steel. The fluid used here is air ideal gas. From the specified geometric characteristics and the operating conditions the performance curve for the investigated model is determined.
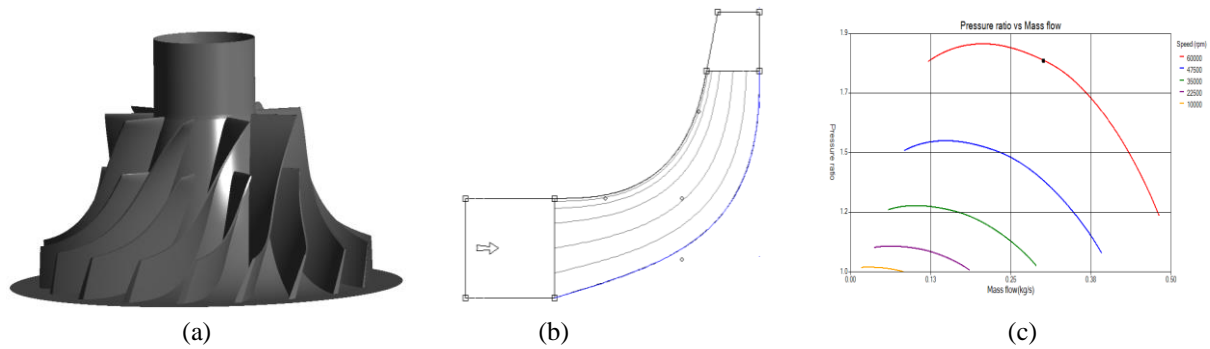


| (a) | (b) | (c) |

**Fig. 1.** (a) 3-D geometry of Compressor, (b) Meridional view of impeller, (c) Performance Curve

## 3.2. Grid distribution

For the purpose of solving the governing partial differential equations for CFD and structural model the geometry needs to be discretized over which the equations can be approximated. The grid generation for the investigated model has been done separately for two cases: CFD analysis and structural analysis. For the CFD case part, the geometry of the compressor model is discretized with anisotropic hexahedral mesh. A refined layer of mesh is created near the wall boundary and impeller tip region. Along the highly curved surfaces, the 'body-fitted' non-orthogonal structured grids generate which reduces the mesh generation time and also the solution time efficiently. The mesh for structural model is generated using sweeping method from shroud to hub. The generated mesh is hexahedral dominant with some prism layer meshes. The orthogonality factor and skewness are checked for the structural model meshes and are found to be in acceptable range.
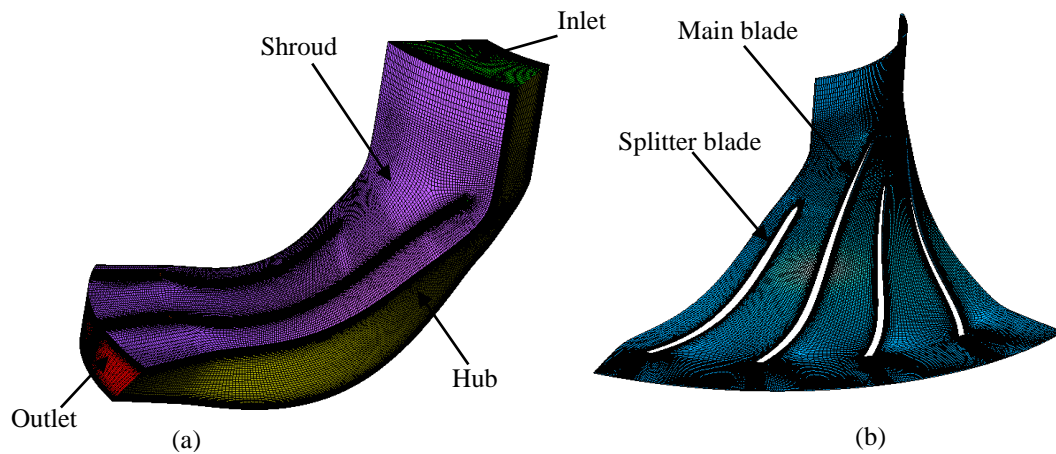


**Fig. 2.** (a) 3-D mesh view of an impeller, (b) Mesh elements at 50% of span

### 3.3. Grid Independency Verification

It is necessary to carry out the independency verification of the grid system before CFD computation. From the performance curve of centrifugal compressor at design flow rate of 0.3 kg/s, with a rotating speed of 60000 rpm, the expected pressure ratio is 1.83. The grid independency test is performed for five grid system. And finally we have chosen the 2 million fine mesh for the CFD problem to better capture the flow near the wall region. The solid blade body has 170177 nodes and 25250 elements for structural analysis.

**Table 1.** Total Pressure ratio for different grid system (CFD case)

| Total Nodes | Total Elements | Total Pressure ratio |
|:---:|:---:|:---:|
| 401746 | 370521 | 1.86 |
| 432300 | 399300 | 1.87 |
| 874680 | 822898 | 1.87 |
| 1381800 | 1312002 | 1.86 |
| 1982890 | 1894220 | 1.86 |

### 3.4. Numerical simulation method

A steady-state turbulent flow simulation method is adopted for the CFD analysis. The rotational axis of the hub is along the negative z-axis of the global coordinate system. The fluid domain consists of inlet, outlet and main passage. A solid domain is created comprising of the main blade and splitter blade, extracted from the fluid domain and meshed separately for the purpose of structural analysis. A fluid-solid interface is existed where the fluid domain touches the solid domain. And, along the tip clearance there also exists fluid-fluid interface. Hub and shroud are in rotating frame of reference and with respect to them inlet and outlet are in stationary frame of reference. For the CFD analysis, a pressure inlet and mass flow outlet is specified. Again, for hub and shroud wall no-slip condition and adiabatic heat transfer option are assigned. Adiabatic heat transfer option is available through the solid blade body. Additionally, for the structural analysis two cases are considered. In one case there is no rotational velocity and for the other case, rotationally induced inertial effect is considered. The face attached to the hub is considered to be as a fixed support. Pressure and temperature loads are imported from the CFD analysis to determine the equivalent stresses and total deformation in the blade body.

## 4. Results and discussions

### 4.1. Relative Mach number and velocity distribution
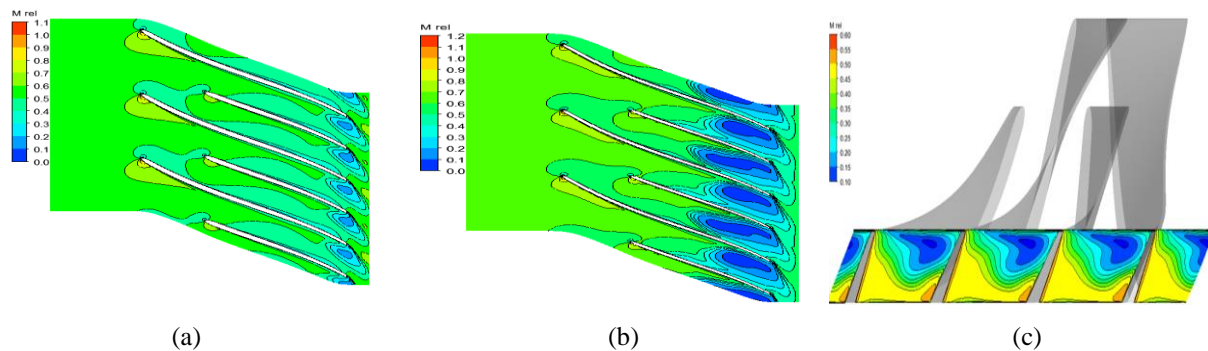


| (a) | (b) | (c) |

**Fig. 3.** Contour of relative Mach number at (a) 50% span, (b) 80% span, (c) blade trailing edge

From fig. 3 it can be seen that the relative Mach number is gradually increasing from leading to trailing edge of the main blade along the streamlines, but due to the presence of splitter blade the flow diffuses and tends to have a similar pattern of flow in the impeller exit. The vane needs to be carefully designed as transonic flow is found to be in the impeller leading edge. In fig. 3(a) and 3(b) small shock waves are seen in the leading edge which may lead to severe instabilities and corresponding losses. Flow separation is apparent near the trailing edges and thickens near the shroud due to the tip clearance effect, and thus causes larger blockage in the flow path. The use of splitter blades largely reduces the wake region and improves the mass flow through the impeller exit. Fig. 4 depicts that the flow is well attached, smooth and homogeneous, except flow reversal is seen near the shroud tip region due to the tip clearance effect. Again, due to the pressure difference between the pressure surface and

suction surface of the impeller, vortex flow generates downstream of the impeller and reduces the velocity of the air at the adjacent streamlines.
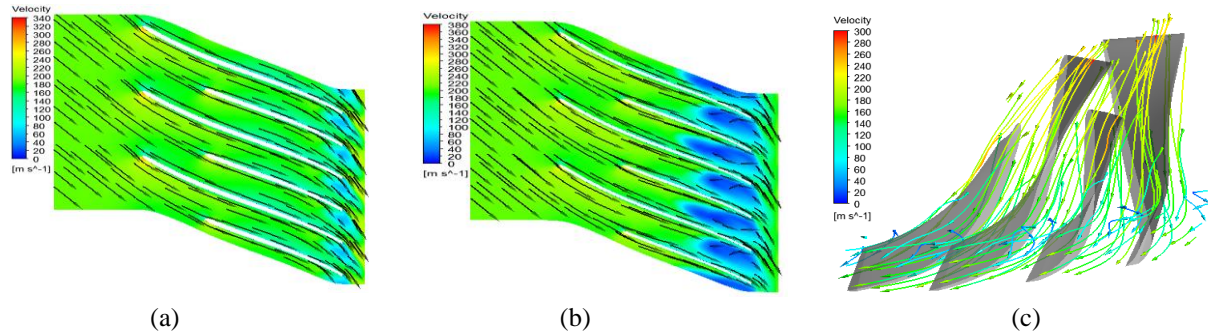


| (a) | (b) | (c) |

**Fig. 4.** Velocity vectors at (a) 50% span, (b) 80% span and (c) Velocity streamlines

## 4.2. Pressure distribution and entropy change
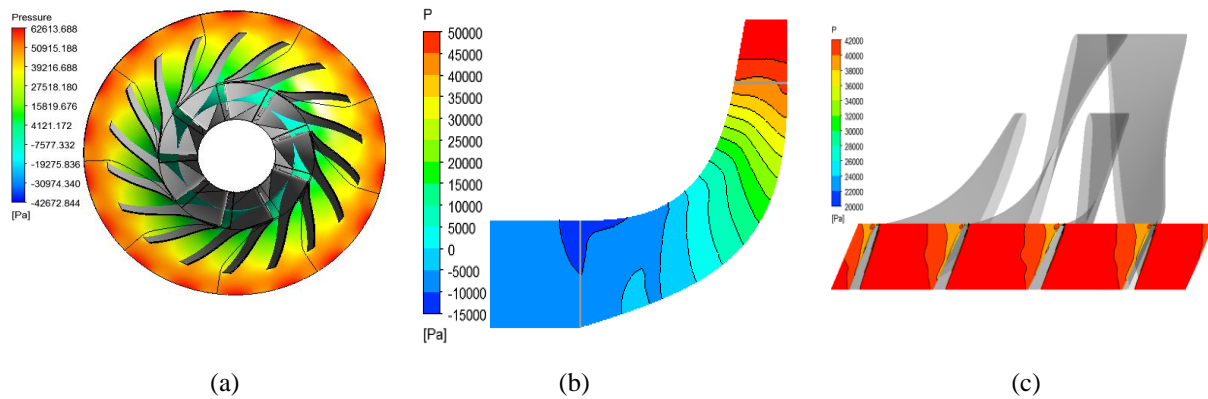


| (a) | (b) | (c) |

**Fig. 5.** (a) Pressure distribution at 50% span, (b) Contour of pressure on Meridional Surface, (c) Contour of Pressure at blade trailing edge

The fig. 5(a) shows the pressure distribution between the blade to blade passage from inlet to outlet in streamwise direction when the centrifugal compressor operating at design conditions. The pressure increases gradually along stream-wise direction and due to the presence of splitter blade the pressure is almost homogeneous on both pressure and suction surfaces. From fig. 5(c), we can observe that, the pressure at impeller exit is very smooth along the throat area except a slight decrease in pressure head near the suction side tip region. Fig. 5(b) shows the smooth increase of meridional surface pressure along the streamwise direction and also the choke flow region near the impeller inlet. As a result, there is a certain decrease in downstream pressure in the impeller inlet region and causes instabilities and vibrations in the machine.
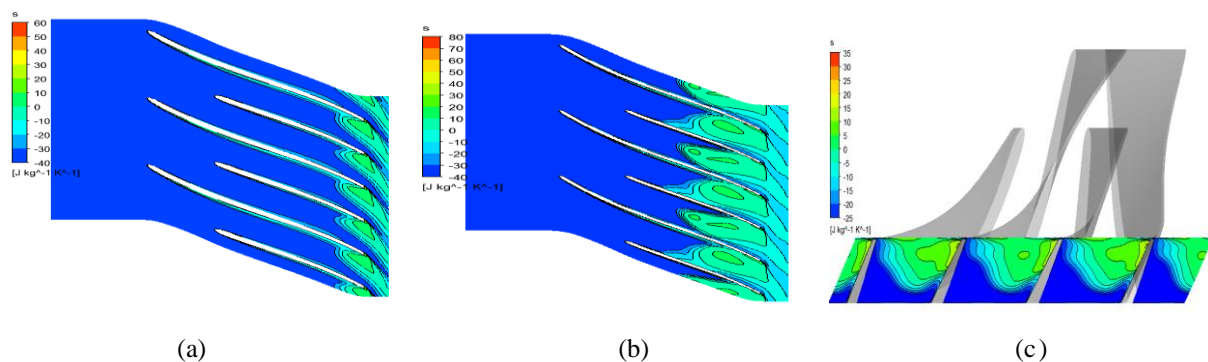


| (a) | (b) | (c) |

**Fig. 6.** Entropy change at (a) 50% span, (b) 80% span and (c) contour of entropy change at blade trailing edge

Fig. 6 points out the entropy change in blade-to-blade passage across streamwise direction and in throat area at blade trailing edge. Entropy at the wall of impeller leading edge is maximum due to the presence of shock wave. Again, entropy close to the blade side wall is higher than the blade passage due to the boundary layer effect. As flow reversal and tip leakage flow are prominent at region near the shroud, higher entropy is observed at impeller exit and even in the blade passage.

## 4.3. Turbulence kinetic energy and gas compressor performance
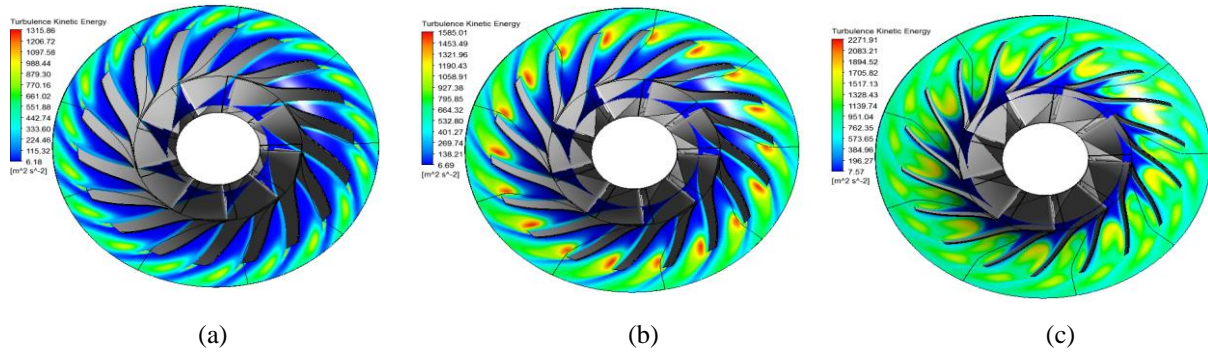


| (a) | (b) | (c) |

**Fig. 7.** Turbulence kinetic energy at (a) 20% span, (b) 50% span and (c) 80% span

Behavior of turbulence in a centrifugal compressor is very difficult to calculate accurately and is not very well known till date. The turbulence model used here is k-epsilon which solves for two variables: k; the turbulent kinetic energy, and epsilon; the rate of dissipation of kinetic energy. Turbulence starts at impeller leading edge and increases far downstream of the flow. The generation of vortex at tip due to the pressure difference between the pressure and suction sides moves in the opposite direction of the compressor rotation, convecting turbulence into the passage. Turbulence in the blade passage is more prominent near the shroud region than the hub due to the tip clearance effect. Moreover, the turbulence is higher near the blade wall than the blade passage.

The distribution of other flow parameters such as static and total temperature, pressure and enthalpy along the streamline or span of the blade were also studied. The averaged results tabulated here will be helpful in understanding the overall performance of the compressor.

**Table 2.** Gas compressor performance

| Parameters | Inlet | Outlet | Ratio(Out/In) |
|---|---|---|---|
| Temperature | 280.418 K | 331.976 K | 1.18386409782334 |
| Total Temperature | 288.001 K | 350.846 K | 1.21821205249311 |
| Pressure | 92291.2 kg m^-1 s^-2 | 155618 kg m^-1 s^-2 | 1.68616474289756 |
| Total Pressure | 101321 kg m^-1 s^-2 | 188938 kg m^-1 s^-2 | 1.86474778384332 |
| Enthalpy | -17810.3 m^2 s^-2 | 33975.3 m^2 s^-2 | -1.90761612767174 |
| Total Enthalpy | -10194.1 m^2 s^-2 | 52927.5 m^2 s^-2 | -5.19195371732098 |

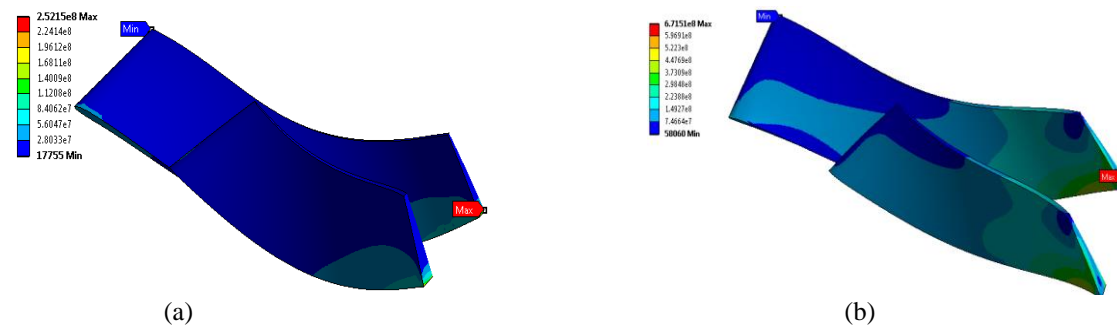## 4.4. Equivalent stresses



| (a) | (b) |

**Fig. 8.** Equivalent stress distribution (in Pascal) (a) without rotation (case-1), (b) with rotation (case-2)

The mechanical stress experienced by the impeller set due to the pressure and temperature loading through the machine is shown in fig. 8 for two cases: (a) without rotation and (b) with rotation. The maximum stress in case-2 is much larger than case-1, as there is no rotationally induced inertial effect in case-1. Moreover, the equivalent stress distribution at different span of impeller is much larger in case-2. The maximum stress is found at hub tip region for both cases. It is also evident that the blade thickness from hub to shroud strongly influences the von Mises stress. The initial design was done in such way that the blade thickness increases from shroud to hub to counter the high stress regions. In reference [6] it is shown that the hub blade thickness has little impact on compressor efficiency. For the impeller set, the maximum stress in main blade is slightly higher than the splitter blade. The high stress region near the tip is justified as the pressure, temperature and the rotational velocity all are increasing from leading to trailing edge of the impeller.

## 4.5. Total deformations



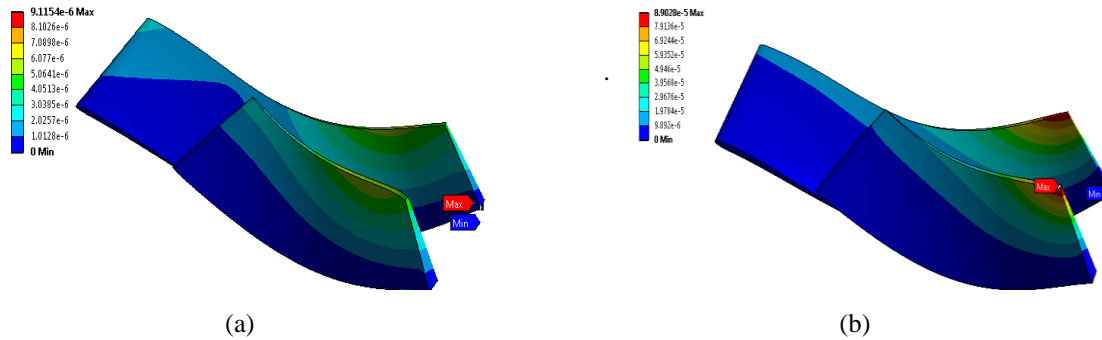<div align="center">(a)        (b)</div>

**Fig. 9.** Total deformation (in meter) (a) without rotation, (b) with rotation

Another mechanical property evaluated is total deformation of the impeller blade set. It is previously mentioned that the tip clearance between shroud and tip of the main blade is 0.03mm. So, the maximum allowable blade tip deformation must be equal to or lower than this value. For case-1 the maximum value of deformation is 0.009mm which is in allowable range. But, for case-2, due to the rotational velocity the deformation at tip is 0.089mm which is larger than tip clearance gap. So, we need to increase the gap between blade and shroud cover above 0.089mm which in turn, increases the secondary flow and tip leakage and causes further losses.

## 5. Conclusion

The complex centrifugal compressor internal flow field is investigated by using the k-epsilon turbulence model along with the simulation of 3-D steady Navier–Stokes equations. The internal flow simulation of the centrifugal compressor demonstrates the flow pattern and pressure distribution of the compressor operating at design point. The velocity vector is almost homogeneous on both pressure and suction side surfaces but, tip leakage and flow reversal exist near the impeller exit which is dominant near the shroud tip region. As for pressure distribution, the pressure increases gradually along the streamwise direction and the presence of splitter blade causes a smooth pressure distribution on both side of the blade. Small shock regions are observed near the leading edge which causes loss in energy head. For the structural analysis, the trailing edge tip is found to be the most critical region. Although, convergence and mesh generation all are in acceptable range, a physical experimentation of the addressed centrifugal compressor is still required to justify the numerical values generated during the simulation process. This paper can still help designers in choosing different parameters during the primary design phase.

## 6. References

[1] H. Versteeg, W. Malalasekera, An Introduction to Computational Fluid Dynamics: The Finite Volume Method, Prentice Hall, 2nd edition, 2007.
[2] Egor P. Popov, Mechanics of Materials, Prentice Hall, 2nd edition, 1976.
[3] S Larry Dixon and Cesare Hall, Fluid Mechanics and Thermodynamics of Turbomachinery, Butterworth-Heinemann, 7thd edition, November 13, 2013.
[4] H. Cohen, GFC Rogers and HIH Saravanamuttoo, Gas Turbine Theory, Longman Group Limited, 4th edition, 1996.
[5] H. David Joslyn, Joost J. Brasz, and Robert P. Dring, "Centrifugal Compressor Impeller Aerodynamics: An Experimental Invesitgation", Journal of Turbomachinery, Vol.113, No.4, pp. 660-669, 1991.
[6] T. Verstraete, Z. Alsalihi, R.A. Van den Braembussche, "Multidisciplinary optimization of a radial compressor for microgas turbine applications", Journal of Turbomachinery, Vol. 132, 2010.

# Flow-Induced Vibration Mechanism of a Cylinder Immersed in a Wake

B. Qin[1], Md. Mahbub Alam[1, 2], Y. Zhou[1]
[1]Institute for Turbulence-Noise-Vibration Interaction and Control, Shenzhen Graduate School, Harbin Institute of Technology, Shenzhen, China
[2]Key Lab of Advanced Manufacturing Technology, School of Mechanical Engineering and Automation, Shenzhen Graduate School, Harbin Institute of Technology, Shenzhen, China
*Email: alamm28@yahoo.com; alam@hitsz.edu.cn*

## Abstract

*Flow-induced vibration response of a circular cylinder (diameter D) placed in the wake of a rigid circular cylinder of smaller diameter d is examined experimentally. The monitoring cylinder is both-end-spring-mounted, free to oscillate only in the cross-flow direction. D is kept fixed, d is varied from d/D = 0.2 to 1.0. The spacing L between the center of the upstream cylinder to the forward stagnation point of the downstream cylinder is changed from L/d = 1.0 to 5.5. Flow-induced vibration amplitude A/D, vortex shedding frequency, lift force and PIV measurements are conducted. A decreasing d/D causes a higher instability of flow, leading to violent vibration. Vortex shedding characteristics at some representative cases are elaborated. Two shear layers reattaching alternately on the downstream cylinder may excite the cylinder vibration. In addition, what happens during the start of vibration is explicated through measurements of added mass and added damping.*

Keywords: Flow-induced vibration, Vortex shedding frequency, Different diameters, Lift force.

## 1. Introduction

The study of flow-induced vibrations (FIV) of a structure is important in many engineering fields, including aeronautical, offshore, power plant, civil, and wind engineering. Previous investigations have mostly been concerned with two rigid circular cylinders in tandem, paying attention to flow structures generated, forces acting on them, Strouhal frequencies, etc., [1]. Bokaian and Geoola [2] surveyed FIV of a both-end-spring-mounted cylinder immersed in the wake of a fixed identical upstream cylinder, where the downstream cylinder is free to oscillate laterally. The mass-damping ratio $m^*\zeta$ of the system is about 0.109 (where $m^*$ = mass ratio, $\zeta$ = damping ratio). FIV characteristics of two circular cylinders in tandem have been investigated by Kim *et al*. [3], with $L/d = 0.6 \sim 3.7$, reduced velocity $U_r = 1.5 \sim 26$ and $m^*\zeta = 0.65$. The FIV of a pair of cylinders in tandem has also been investigated by Assi *et al*. [4, 5] for $L/d \geq 4.0$ at $m^*\zeta = 0.013$, where the mechanism of the origin of the downstream cylinder lift forces has been elucidated. Divergent vibration was observed for $L/d = 4.0 \sim 6.0$ with increasing $U_r$, and constant vibration amplitude was for $L/d > 6.0$. A review of previous researches connected with FIV of two tandem cylinders indicates that former investigations have mostly been with two identical diameter cylinders at a low $m^*\zeta$ value. A systematic study on the influence of the upstream cylinder size (diameter) on FIV of a downstream cylinder is very scarce. The objective of this work is to study experimentally FIV characteristics of a cylinder in the presence of an upstream fixed cylinder of which the diameter is changed.

## 2. Experiment details

FIV experiments were carried out in a low-speed, close-circuit wind tunnel with a test section of 5 m long, 0.8 m width and 1.0 m height. A schematic diagram of the experimental setup is shown in Fig. 1. The upstream cylinder diameter $d$ was 8, 16, 24, 32 and 40 mm and the downstream cylinder diameter $D$ was 40 mm, corresponding to $d/D = 0.2, 0.4, 0.6, 0.8$ and $1.0$, respectively. $L/d = 1.0, 1.5, 2.0, 2.5, 3.0, 3.5, 4.0$ and $5.5$ were chosen. The upstream cylinder was fixed at both ends. Each end of the downstream cylinder was supported by two spiral springs (Fig. 1c). A standard laser vibrometer was used to measure the vibration-amplitude $(A)$ and vibration frequency of the downstream cylinder. $\zeta$, $m^*\zeta$, and natural frequency of the cylinder $(f_n)$ were estimated to be 0.0021, 0.58, and 11.72 Hz, respectively. Free-stream velocity $U_\infty$ was varied from 1.8 to 10.3 m/s, corresponding to variation of $U_r$ from 3.8 to 22.0 and of $Re$ (based on $D$ and $U_\infty$) from $4.8 \times 10^3$ to $2.7 \times 10^4$. Two hot wires, one (HT1) placed in the gap at $(x'/d, y'/d, z'/d) = (1, 1, 0)$, another (HT2) behind the downstream

cylinder at ($x/D$, $y/D$, $z/D$) = (4, 1, 0), were used to measure natural vortex shedding frequencies. Flow-induced forces and flow structures were measured by using a pressure scanner and a PIV system, respectively.
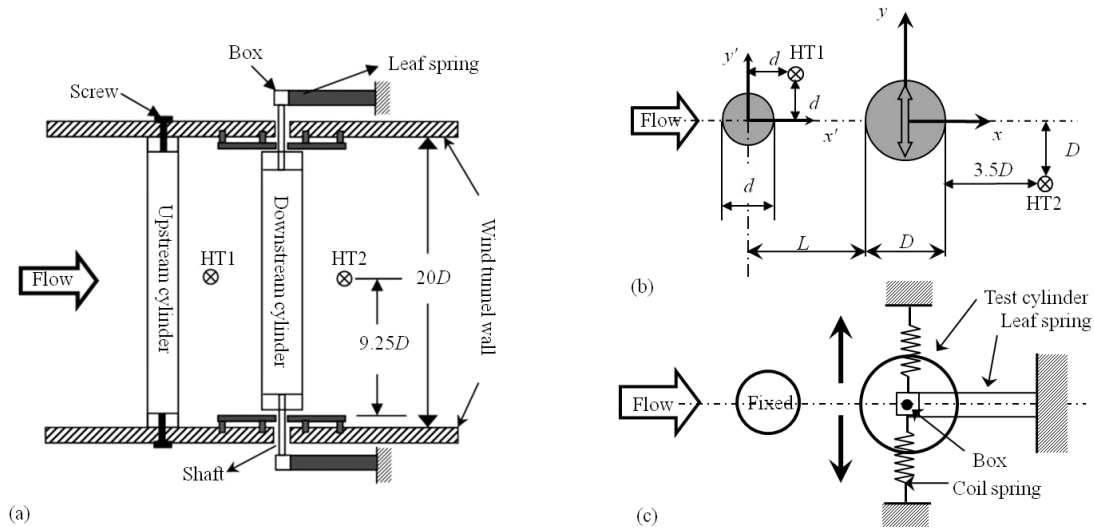


**Fig. 1.** Experimental setup (a) Experimental arrangement, (b) definition of symbols, (c) the test cylinder mounting system

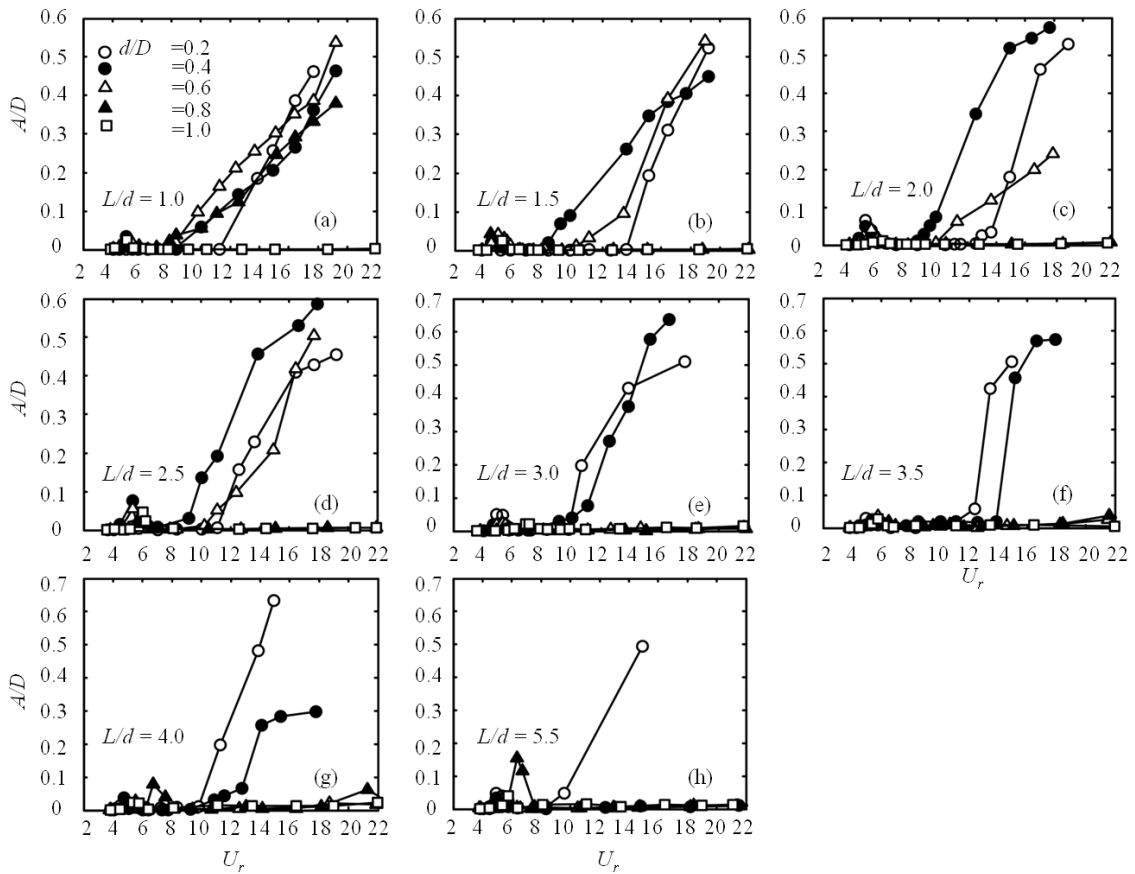## 3. Results and discussions

### 3.1. Vibration response



**Fig. 2.** FIV responses for different $d/D$ at (a) $L/d$ = 1.0, (b) $L/d$ = 1.5, (c) $L/d$ = 2.0, (d) $L/d$ = 2.5, (e) $L/d$ = 3.0, (f) $L/d$ = 3.5, (g) $L/d$ = 4.0, and (h) $L/d$ = 5.5.

Fig. 2 presents the dependence of the cylinder vibration amplitude ratio ($A/D$) on $d/D$ and $L/d$. At $L/d = 1.0$, violent and divergent vibrations occur for $d/D = 0.2, 0.4, 0.6, 0.8$ at $U_r > 11.5, 8.8$ and $8$ respectively. Tiny humps engendered around $U_r = 5$ signify the occurrence of vortex-excitation (VE) (Fig. 2a). At $1.5 \leq L/d \leq 2.5$ (Fig. 2b, c, d), $d/D = 0.2, 0.4$ and $0.6$ generate vibrations, while $d/D = 0.8$ and $1.0$ do not. As $L/d$ is increased to $3.0 \sim 4.0$ (Figs. 2e, f, g), vibration only appears for $d/D = 0.2$ and $0.4$. Extending $L/d$ further to $5.5$ leads to vibration for $d/D = 0.2$ only (Fig. 2h). Thus, it can be inferred that a cylinder immersed in the wake of another of different diameter may undergo a catastrophic vibration, and a decrease in $d/D$ results in a higher instability of flow.

### 3.2. Power spectral analysis results

Representative power spectral analysis results of HT2 and laser vibrometer signals at $d/D = 0.4$, $L/d = 2.0$ are presented in Fig. 3(a, b). $f/f_n$ of the horizontal axis is the normalized Fourier frequency $f$. The peaks in the power spectra are extracted as $f_v/f_n$ and plotted in Fig. 3(c). The corresponding vibration response is presented in Fig. 3(d) in order to have a mutual vibrant discussion between shedding frequency and vibration response. $f_v/f_n = 1.0$ at $U_r = 4.5 \sim 5.3$ is observed in both HT2 and laser vibrometer results (Fig. 3a, b). Convergent vibration occurs in this range of $U_r$ (Fig. 3d), indicating VE, resonance and lock-in. As $U_r$ goes beyond the lock-in range, $f_v/f_n \neq 1.0$, rising monotonically following $St = 0.2$ until $U_r = 8.5$. No vibration thus occurs at $5.3 < U_r < 8.5$. With an increase in $U_r$, the cylinder begins to vibrate at $U_r = 8.5 \sim 9.8$, the vibration amplitude taking off; the second peak corresponding to $f_v$ is more discernible (Fig. 3b) and HT2 results do not display peak at $f_v/f_n = 1.0$. The information indicates that the vibration is initiated by the vortex shedding from the cylinder, not by any shedding associated with $f_n$. On the other hand, when the amplitude is large enough ($U_r > 9.8$), there are two dominant peaks in the HT2 results (Fig. 3a), corresponding to vibration frequency ($f_v/f_n = 1.0$) and natural vortex shedding frequency as presented in Fig. 3(c). The latter frequency follows Strouhal number $St = 0.2$ up to $U_r = 14.9$ and then locks-in to the third harmonic of $f_n$ for $U_r > 14.9$ where $A/D$ escalation is restricted.
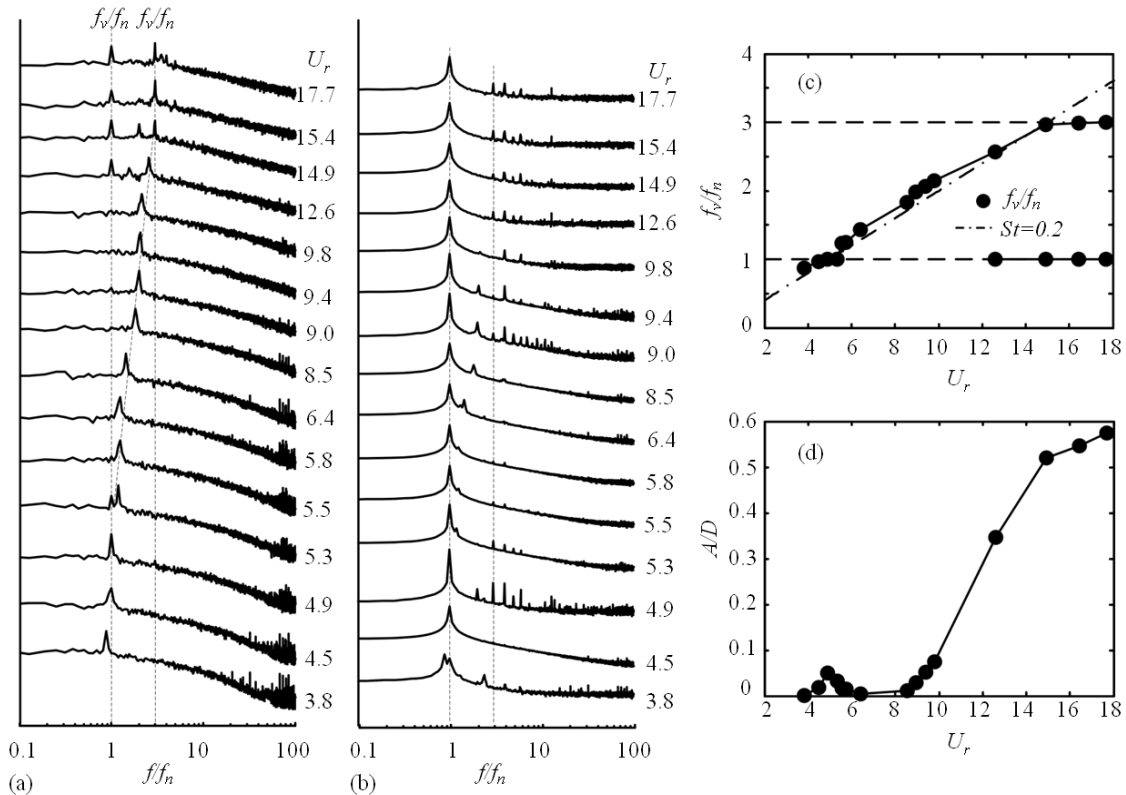


**Fig. 3.** Representative power spectral analysis results (a) Power spectrum of HT2 signal, (b) power spectrum of laser vibrometer signal, (c) vortex shedding frequency obtained from HT2, and (d) $A/D$ variation with $U_r$. $d/D = 0.4$, $L/d = 2.0$.

### 3.3. Vibration mechanism

Fig. 4(a) shows the schematic plot of the cylinder displacement $y/D$ and lift force coefficient $C_L$ in a half cycle of oscillation at $L/d = 2.0$, $d/D = 0.4$, accompanied with the phase-average vorticity and pressure coefficient $C_P$ (positive when the arrow points to the cylinder center) distributions (Fig. 4b $\sim$ f). First, it is necessary to clarify that due to the additional cables mounted around the cylinder for measuring pressure, the $m^*$

and $\zeta$ have changed to 350 and 0.043, respectively. As the downstream cylinder moves upward, the upstream cylinder shear layer emanating from lower side reattaches on the lower side of the downstream cylinder at $\theta \approx -22.5°$ where $C_P \approx +1$ (Fig. 4b). A slice of the reattached flow together with the upper shear layer sweeping over the upper side of the downstream cylinder gives rise to a highly negative pressure on the upper side, resulting in an upward lift force. With the cylinder moving upward, the shear layer from upper side reattaches, resulting in the decay of lift. A maximum negative lift occurs as the upper shear layer passes over the lower side and stagnation pressure on the upper side is generated by the freestream flow (Fig. 4d, e). The cylinder thus speeds up downward.
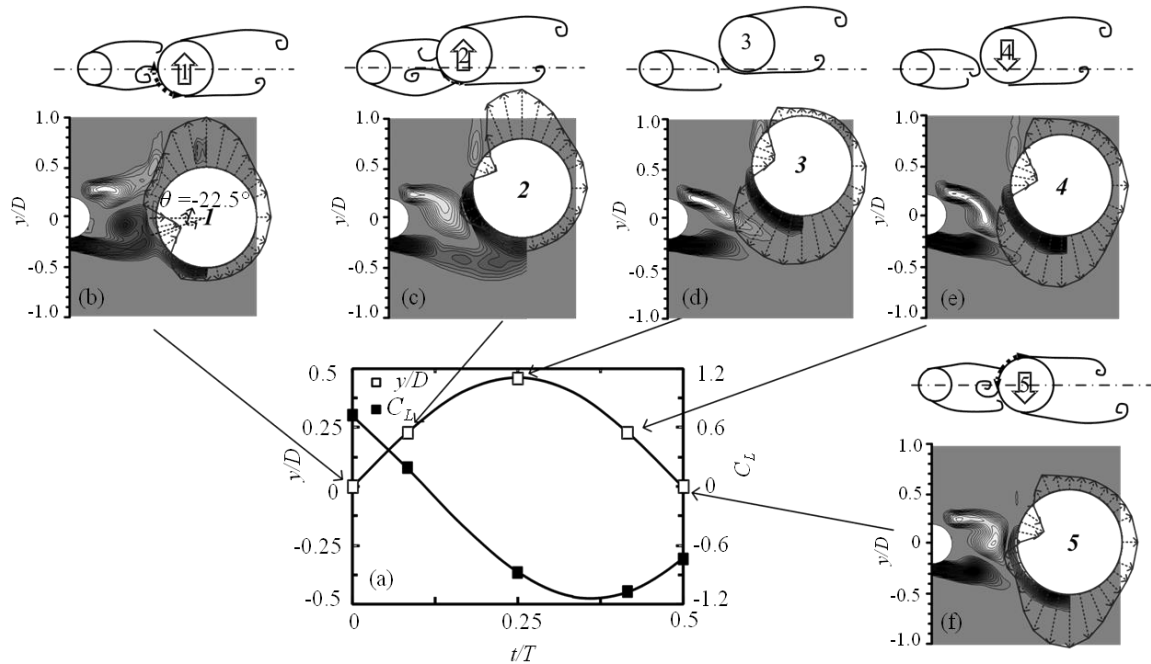


**Fig. 4.** (a) Cylinder displacement $y/D$ and lift force coefficient $C_L$ in half cycle of the oscillation, (b-f) phase-averaged vorticity and pressure coefficient $C_P$ at $L/d = 2.0$, $d/D = 0.4$, $A/D = 0.48$.

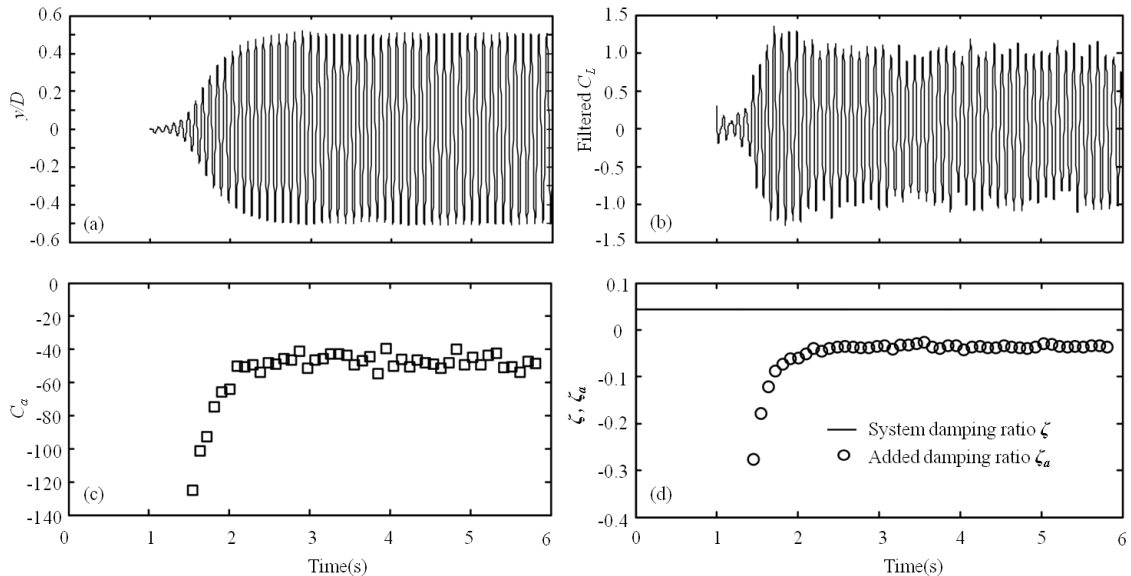### 3.4. Added mass coefficient and added damping ratio



**Fig. 5.** Time history of (a): $y/D$, (b) filtered $C_L$, (c) added mass coefficient $C_a$, and (d) added damping ratio $\zeta_a$ when the downstream cylinder is fixed and then released at $t = 1$ s.

Fig. 5 (a, b) show the evolution of $y/D$ and filtered $C_L$ where the lift force is band-pass filtered by 5 ~ 20 Hz to contain only frequency component of the lift around the vibration frequency since others will not yield a net contribution to the energy transfer between the fluid and the body [6]. Note that the cylinder was kept fixed and

suddenly released at $t = 1$ s. At the same time, the maximum $y/D$ (amplitude) in each cycle increases from $\approx 0$ to 0.48 at $t = 1 \sim 2.9$ s, and then remains nearly constant (Fig. 5a). At $t = 1 \sim 1.4$ s where the cylinder starts to vibrate, $C_L$ varies irregularly, being not sinusoidal. $C_L$ then undergoes an increase in amplitude in each cycle reaching maximum at about $t = 1.7$ s, after which it suffers a small decrease before being approximately stable (Fig. 5b). Besides, the added mass coefficient $C_a$ and added damping ratio $\zeta_a$ which are concerned with the lift force components in phase with the cylinder acceleration and velocity, respectively, are presented in Fig. 5 (c, d).

At $t < 1.4$ s, since the filtered $C_L$ is not sinusoidal and the harmonic forcing and harmonic motion assumption is not applicable, the calculation of $C_a$ and $\zeta_a$ starts at $t = 1.4$ s. The calculation method of $C_a$ and $\zeta_a$ in each cycle can be found in [7]. $C_a$ is highly negative -125 at $t \approx 1.4$ s where the vibration starts, increasing to its asymptotic value -47 at $t \approx 2.3$ s where the vibration is stable (Fig. 5c). $C_a \approx -47$ at $t > 2.3$ s is much smaller than $m^* = 350$; cylinder vibration frequency hence does not differ from $f_n$. On the other hand, $t < 2.3$ s the vibration frequency increases upto $1.12f_n$ (not shown). Between $t = 1.4$ s and 2.3 s, $\zeta_a$ being negative escalates from -0.27 to -0.043; the magnitude of the latter is equal to the system damping ratio $\zeta$ (Fig. 5d). Thus it may be inferred that during the increase of the vibration amplitude, the cylinder sustains a negative effective damping ratio ($\zeta + \zeta_a < 0$), leading to an exponential growth of oscillation amplitude. On the contrary, at the stable vibration, nearly zero damping ratio is obtained ($\zeta + \zeta_a \approx 0$), which means that a balance is reached between the energy transferred from the fluid to the structure and the energy consumed by the system damping.

## 4. Conclusions

A violent vibration of the cylinder is observed for $d/D = 0.2 \sim 0.8$ at $L/d = 1.0$, for $d/D = 0.2 \sim 0.6$ at $1.0 < L/d \leq 2.5$, for $d/D = 0.2 \sim 0.4$ at $2.5 < L/d \leq 4.0$, and for $d/D = 0.2$ at $4.0 < L/d \leq 5.5$, but not for $d/D = 1.0$. A decreasing $d/D$ is inclined to engender vibration for a longer range of $L/d$. For certain $d/D$ - $L/d$ cases, a lock-in of vortex shedding to the third harmonics of the cylinder vibration frequency is observed. Two shear layers of the upstream cylinder reattaching alternately on the downstream cylinder give rise to a large change in lift that maintains the vibration. A negative effective damping ratio ($\zeta + \zeta_a < 0$) leads to a growth in vibration amplitude where the energy transferred from the fluid to the structure is larger than the energy consumed by the system damping. On the other hand, at stable vibration condition, $\zeta + \zeta_a \approx 0$ is obtained, representing a balance between energy transfer and consumption.

## References

[1] M.M. Alam, M. Moriya, K. Takai, and H. Sakamoto, "Fluctuating fluid forces acting on two circular cylinders in a tandem arrangement at a subcritical Reynolds number", *Journal of Wind Engineering and Industrial Aerodynamics*, Vol.91, No.1, pp. 139-154, 2003.

[2] A. Bokaian, and F. Geoola, "Wake-induced galloping of two interfering circular cylinders", *Journal of Fluid Mechanics*, Vol.146, pp. 383-415, 1984.

[3] S. Kim, M.M. Alam, Sakamoto. H, and Zhou. Y, "Flow-induced vibrations of two circular cylinders in tandem arrangement, part 1: characteristics of vibration", *Journal of Wind Engineering and Industrial Aerodynamics*, Vol.97, No.5, pp. 304-311, 2009.

[4] G.R.S. Assi, P.W. Bearman, J.R. Meneghini, "On the wake-induced vibration of tandem circular cylinders: the vortex interaction excitation mechanism", *Journal of Fluid Mechanics*, Vol.661, pp. 365-401, 2010.

[5] G.R.S. Assi, P.W. Bearman, B.S. Carmo, J.R. Meneghini, S.J. Sherwin, and H.J. Willden, "The role of wake stiffness on the wake-induced vibration of the downstream cylinder of a tandem pair", *Journal of Fluid Mechanics*, Vol.718, pp. 210-245, 2013.

[6] T.L. Morse, and C.H.K. Williamson, "Prediction of vortex-induced vibration response by employing controlled motion", *Journal of Fluid Mechanics*, Vol.634, pp. 5-39, 2009.

[7] K. Vikestad, J.K. Vandiver, and C.M. Larsen, "Added mass and oscillation frequency for a circular cylinder subjected to vortex-induced vibrations and external disturbance", *Journal of Fluids and Structures*, Vol.14, No.7, pp. 1071-1088, 2000.

# Experimental Investigation of Lubrication by Wax Dissolved in Chemical Lubricant

Samira Ishrat Jahan and Sobahan Mia
Department of Mechanical Engineering
Khulna University of Engineering & Technology, Khulna-9203, Bangladesh
*E-mail: ishrat499@yahoo.com*

## Abstract

*Lubrication can describe the phenomenon where reduction of wear occurs without human intervention .It is an important fact while considering reduction of friction and wear. The aim of this project was to improve the lubrication ability of a lubricant by the addition of wax into it. Wax was added to lubricant to modify the lubrication properties. Ester was chosen as the lubricant whose properties were to be improved which has been successfully used in lubrication for more than 50 years. The properties that have impact on the behavior of a lubricant such as density, pour point, viscosity etc had been observed for pure ester as well as for wax-ester mixture with 4%, 5%, and 6% wax in it. The test results showed that improvement took place in these properties with the increase in percentage of wax. Also the comparison of resistance to wear of ester and wax-ester mixture gave a clear indication of improved lubricity of wax ester mixture.*
*.*

Keywords: Lubrication, ester, wax, lubricant.

## 1. Introduction

Lubrication is the process or technique employed to reduce wear of one or both surfaces in close proximity, and moving relative to each other, by interposing a substance called lubricant between the surfaces to carry or help carry the load (pressure generated ) between the opposing surfaces. Reducing friction is the main objectives of lubrication, but there are many other benefits of this process. Lubricating film can help prevent corrosion by protecting the surface from water and other corrosive substances.

Currently, the lubrication is a decisive factor in the power of being a source of competitiveness gains, providing improvements in equipment performance, and especially the reduction in maintenance costs **[1].**

Differing widely in viscosity, specific gravity, vapor pressure, boiling point and other properties, lubricants also offer a wide range of selection for the increasingly varied needs of modern industries.

Lubricants containing oil have additives that enhance, add or suppress the properties within the base oil. The amount of additives depends on the type of oil and the application for which it will be used.

The objectives of this project were to study about lubrication and lubrication by ester, to modify the lubricant properties of chemical lubricant by adding wax, to measure the lubricant properties of the modified lubricant and finally to compare the lubrication by wax-ester mixture with chemical lubrication.

## 2. Theoretical aspect

Esters are the reaction products of acids and alcohols. Within the realm of synthetic lubrication, a relatively small but still substantial family of esters have been found to be very useful in severe environment applications.

Synthetic oils are manufactured polyalphaolefins, which are hydrocarbon-based polyglycols or ester oils **[2].** Esters have been used exclusively in jet engine lubricants worldwide for over 40 years due to their unique combination of low temperature flow-ability with clean high temperature operation. Esters are also the preferred stock in the new synthetic refrigeration lubricants used with CFC replacement refrigerants. In automotive applications, the first qualified synthetic crankcase motor oils were based entirely on esters and these products were quite successful when properly formulated. Esters are nearly always used in combination with PAOs in full synthetic motor oils in order to balance the effect on seals, solubilize additives, reduce volatility, and improve energy efficiency through higher lubricity.

In many cases, the very same equipment which operates satisfactorily on mineral oil in one plant could benefit greatly from the use of an ester lubricant in another plant where the equipment is operated under more severe conditions.

## 3. Test procedure

Density, viscosity, flash point,pour point,surface tension and acid number were tested. The test procedures are discussed below.

### Density test

Density is a key property not only in lubricants but in all fluids. It is the measure of the mass of a substance in relation to a known volume [3]. Density test were done with a density kit along with a balance by the following formula-

$$\rho = (M2-M1)/V \tag{1}$$



**Fig. 1.** Density kit and digital balance

Where,M1 is mass of the mass of the density kit when it was empty in gm and M2 is the mass of density kit when it contained V cc of the lubricant.

### Viscosity test

Viscosity is the resistance to flow [4].Viscosity test was done by using Saybolt viscometer. Time (t) for flowing 60 mL of liquid was measured in seconds and viscosity was calculated from the following formula-

$$\upsilon = 0.0022t - 1.95/t \text{ [when t < 100]} \tag{2a}$$
$$\upsilon = 0.0022t - 1.35/t \text{ [when t > 100]} \tag{2b}$$
$$\mu = \upsilon*\rho \tag{3}$$

Where $\upsilon$ is kinematic viscosity in stokes, t is in seconds, $\mu$ is absolute viscosity in Poise and $\rho$ is density of the oil in gm/cc.



**Fig. 2.** Saybolt viscometer for viscosity measurement

### Flash point determination

The flash point of oil is the temperature at which oil begins to burn**.**



**Fig. 3.**Closed cup flash point tester

Flash point was tested using a closed cup flash point tester. The cup containing the lubricant sample was heated.At intervals a flame was brought over the surface. The temperature at which ignition began, was found by a digital thermometer which was recorded as the flash point.

### Pour point determination

The pour point of lube oil is the temperature when the oil stops flowing smoothly as a liquid. Pour point test was done in domestic refrigerator. A sample of lubricant was chilled in a test jar to a set of defined temperatures. At each temperature the test jar was tilted horizontally. When the fluid did not flow within 5 seconds, then that was the experimentally determined pour point. The recorded temperature was 3°C higher.



**Fig. 4.**Pour point determination

### Surface tension calculation

Surface tension is the elastic tendency of liquids which makes them acquire the least surface area possible **[5].** Surface tension was calculated in capillary rise method using three capillary tubes by the following formula-.

$$S_1=0.5*\rho*g*r_1*(h_1+r_1/3) \qquad (4a)$$
$$S_2=0.5*\rho*g*r_2*(h_2+r_2/3) \qquad (4b)$$
$$S_3=0.5*\rho*g*r_3*(h_3+r_3/3) \qquad (4c)$$

Where $r_1$, $r_2$, $r_3$ are internal tube radius in cm ; $h_1$, $h_2$, $h_3$ are height of liquid meniscus in cm; $S_1$,$S_2$, $S_3$ are surface tension in dynes/cm.
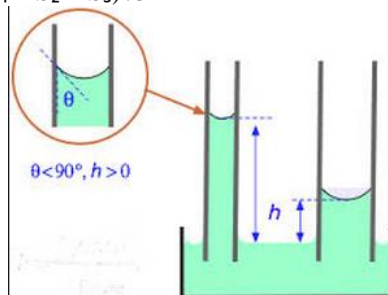
$$S = (S_1 + S_2 + S_3) /3 \qquad (5)$$



**Fig. 5.**Surface tension calculation

**Acid number test**

Acid number is an important quality measurement of crude oil and used as a guide in the quality control of lubricating oil formulations. Acid number was tested using color-indicator titration method by the following formula.

$$\text{Acid Number, (mg NaOH/g sample)} = V \times N \times 56,1 / P \qquad (6)$$

Where V is milliliters of NaOH solution required for sample titration, N is normality of NaOH solution and P is grams of sample used

## 4. Discussion

The project was performed with a view to investigating lubrication by wax dissolved in chemical lubricant. Methyl acetate ester was used as the chemical lubricant since it was easily available in market.

Variation of density with weight percentage of wax in Fig.6.showed that density increases with the increasing weight percentage of wax. The rate of increase of density suddenly became very high at 6% wax-ester mixture. As the density increases, the fluid becomes thicker. Thus the distance between contacting surfaces increases and friction is reduced.
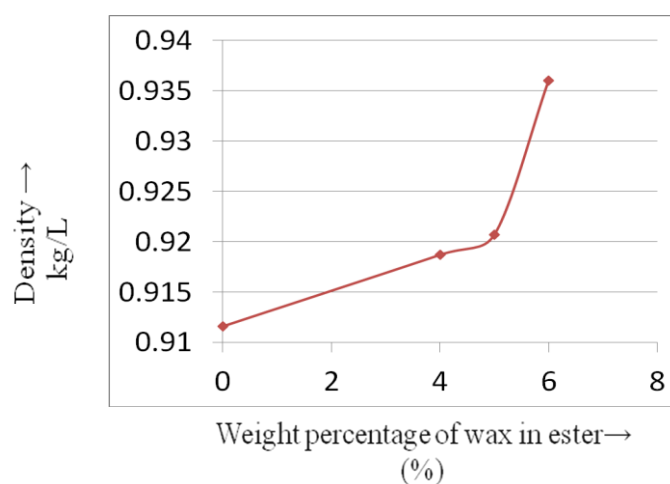


**Fig. 6**. **Re**lation between weight percentages of wax and density

Fig. 7. showed that the kinematic viscosity gradually increases with the increasing weight percentage of wax. With the increase in viscosity, the ability of the lubricant to resist shearing increases, which affects the improvement of machinery life.
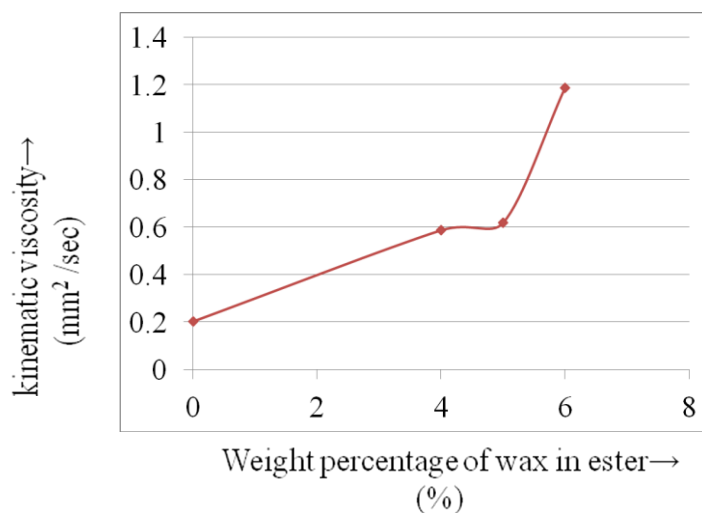


**Fig. 7.Re**lation between weight percentages of wax and  kinematic viscosity

It was observed that the pour point of wax-ester mixture was very low (less than -20°C) .That's why it would be successfully used as lubricant in low temperature condition rather than high temperature.
Often lubricant will come in direct contact with flame or enough heat generated from the friction of moving parts will cause  it to burn. It is important to use lubricant with a high flash point as it is more stable and will withstand higher temperatures, burning less.
It was seen from Fig. 8. that flash point increased with wax percentages though the variation is very small.
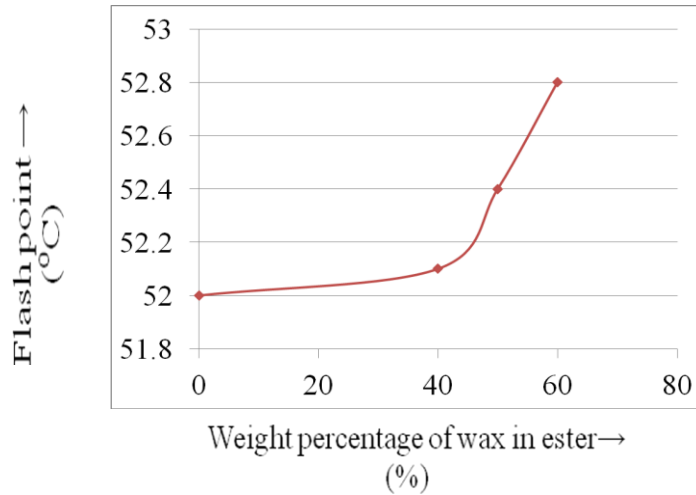


**Fig. 8. Re**lation between weight percentages of wax and flash point

From Fig. 9. it was found that up to 4% wax, the surface tension remained almost constant There was a slight increase when wax was 5% and a rapid increase occurred when the percentage of wax was increased to 6%.Due to increase in surface tension ,the lubricant become more resistant to oxidation and contamination so that lubrication property improves by the addition of wax.
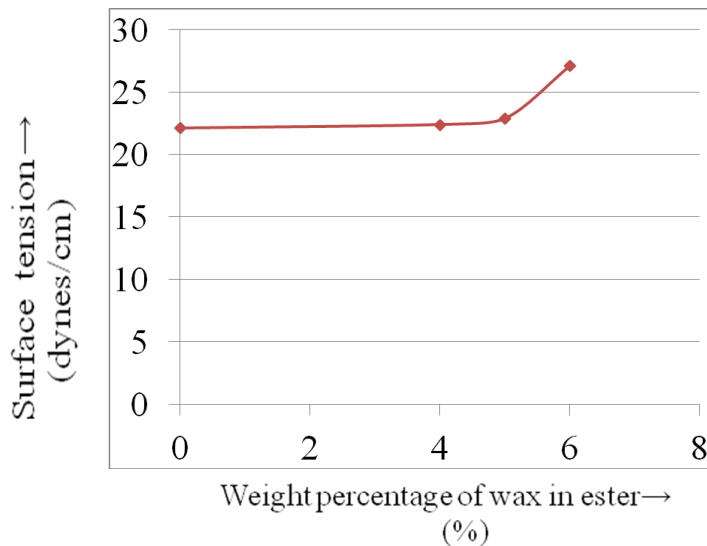


**Fig. 9.**Relation between weight percentages of wax vs. surface tension

Fig. 10.  showed that the acid number gradually increases with the increasing weight percentage of wax. AN was tested  in order to prevent problems such as machine corrosion, wear, varnish and clogged filters.
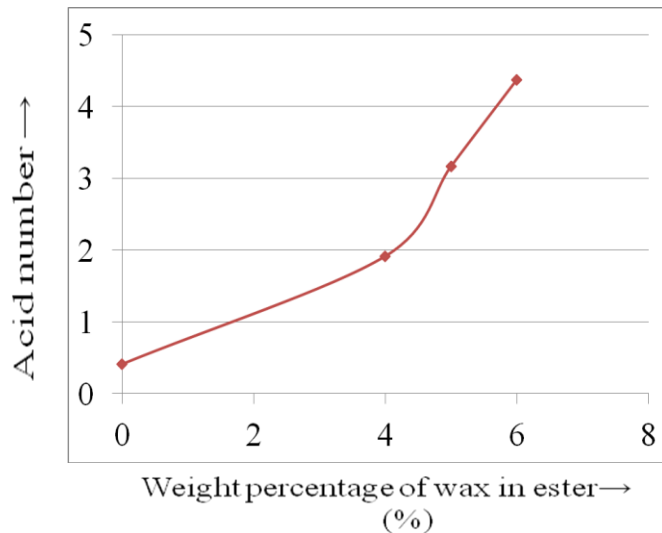
**Fig. 10.** Relation between weight percentages of wax vs. acid number

From the analysis of effect of ester and wax-ester mixture on wear behavior, it was seen that wax-ester mixture showed better resistance to wear than ester.

Since methyl acetate has a very low boiling point (about 56.9 °C) at high temperature wax-ester mixture got evaporated. But if wax could be added with ester of high boiling point then lubricity of the esters could be improved by the addition of wax.

One of the objectives of this project was to study about lubrication and lubrication by ester which has been fulfilled in the "theoretical aspect" section. The lubricant properties such as density, viscosity, flash point, surface tension, acid number have been measured for pure ester first and then for modified wax-ester mixture. From the property measurement, it was clearly observed that wax-ester mixture has shown an improvement in these properties.

## 5. Conclusion

Various features about lubrication such as its regimes, lubrication properties etc along with role of ester in lubrication were studied. Lubricating properties such as density viscosity acid number, surface tension etc were measured for both pure ester and wax-ester mixture containing 4%, 5%, and 6% wax respectively. The variation of these properties with increasing percentage of wax was also shown to compare the effect of wax in the lubrication of ester. From wear test it was found that the lubricity of ester increased with the addition of wax.

## 6. References

[1] Carreteiro.Ronald P. &Moura.Caelos R.S."Lubricants & Lubrication".Rio de Janerio:Editora Makron Books.

[2] Malone,L.J. Basic Concepts of Chemistry.John Wiley & Sons,Inc.,1989

[3] Raymond Serway,John Jewett,"Pinciples of Physics:A Calculus Based Text",Cengage Learning,p-467,ICBN 0-534-49143-X,2005

[4] J.Halling,Introduction to Tribology,Wykeham publication,London,1976

[5] John W.M. Bush(May 2004)"MIT Lecture Notes on Surface Tension,lecture 5"Massachusetts Institute of Technology.Retrived April 1,2007.

# Experimental Studies on Heat Transfer and Friction Factor in a Turbulent Flow Through a Smooth Square Duct

A.K.M. Abdul Hamid[1], M.A. Taher Ali[2], A. R. Akanda[3] and M. Riaz Pervez[4]

[1, 4] Department of Mechanical Engineering, RUET, Rajshahi-6204, Bangladesh
[1]E-mail: mahamid_ruet@yahoo.com
[4]E-mail: mrp@ruet.ac.bd
[2] Department of Mechanical Engineering, BUET, Dhaka -1000,
Road N0.3, House N0.21/A, Dhanmondi, Dhaka, Bangladesh.
E-mail: matali@me.buet.ac.bd
[3] Sonargaon University, 71 Kawranbazer, Tejgaon, Dhaka-1215
Email: akhanda@iut-dhaka.edu

## Abstract

*The forced convective heat transfer is studied experimentally and the measurements are presented of the distributions of local as well as average heat transfer coefficients and the friction factors for a fully developed turbulent flow in an asymmetrically heated smooth square duct at constant heat flux as a boundary condition. In the present experimental investigation it is found that on average, with 57 percent increase in Reynolds Number the static pressure drop is increased by 186 percent and the Nusselt's number is increased by 41 percent. In the present investigation the friction factor obtained increases with the increase of Reynolds Number instead of published data where it decreases or approaches a constant value for smooth noncircular ducts. The results are presented in their final concise form of compact correlations that involve dimensionless groups which represent the characteristics of heat transfer and friction factors. The correlations can be used for improved numerical analysis and for better design of heat transfer equipment's for engineering applications.*

Keywords: Force Convective Heat Transfer, Friction Factor, Turbulent Flow, Smooth Square duct.

## 1. Introduction

In the fluid mechanics and heat transfer several variables are combined into a few dimensionless parameters and the results are presented in the form of empirical equations that involve both individual variable parameters and dimensionless groups. No doubt this technique considerably reduces the number of variables involved in the experimental investigations but does not demonstrate how the characteristics of individual flow parameter behaves with respect to each other in complex situations with imposed boundary conditions. Thus an attempt has been made to study experimentally some of the most important flow parameters such as Nusselt's number, friction factor, Stanton number etc, for a turbulent flow through a smooth square duct. The gathered data will be useful for those pursuing the task of numerical prediction in this area of research and development. The object is to provide a good understanding on the characteristics of some of these variable flow parameters as well as on how they are related to each other when the duct is heated asymmetrically under constant heat flux boundary conditions.

## 2. Literature Survey

The turbulent flow as well as the temperature field in non-circular ducts is influenced by the existence of the secondary flow [3]. Though the velocity of this secondary flow is a small percentage of the primary flow velocity, of the order of 2 to 3 percent, its influence on the flow and temperature fields in the duct cannot be ignored [9]. This is the reason why these variable flow parameters have attracted interest not only for the light they shed on fluid dynamics, but also in relation to the augmentation of heat transfer [6]. Although, in ducts, secondary flow would affect the characteristics of the forced convective heat transfer, as has already been found by many investigators, there are only a few reports on fundamental ducts [7]. It has been recently found that in exactly the same experimental set up and configuration with constant heat flux boundary condition the Prandtl number does not remain constant [2] but it rather decreases with increase of Reynolds Number as well as with increase of location of positions y/B from center towards the side walls. In view of the above discussion, a need therefore exist for an experimental investigation to incorporate Prandtl number as an important variable parameter to obtain improve correlations for correct analysis of heat transfer problems in engineering applications.

## 3. Experimental Set Up and Methodology

The experimental set up has been designed and instruments and probes are installed in it and these are connected with a high speed digital computer. A schematic diagram of the straight experimental setup of length $9735$ $mm$ is illustrated in the Fig: 1. Hydro-dynamically fully developed velocity profiles are attained at about $2500$ $mm$ downstream from the duct entrance. Thus the test section of the duct of length 4869 mm having inner cross section area of $50$ $mm \times 50$ $mm$ consists of heated portion of length $1833$ $mm$ and unheated portion of $3036$ $mm$. The unheated portion of the duct serves to establish hydro-dynamically fully developed flow at the entrance to the heated section. At the working section, at x=1725 mm downstream from the leading edge of the heated portion of the test section, the flow is assumed to be fully developed both hydro-dynamically and thermally. Fig: 2 illustrates the details of the cross sectional view of the heated test section. The heating effect is symmetrical about z-axis but non-symmetric about x- and y- axes,



Legend          All Dimension are in mm
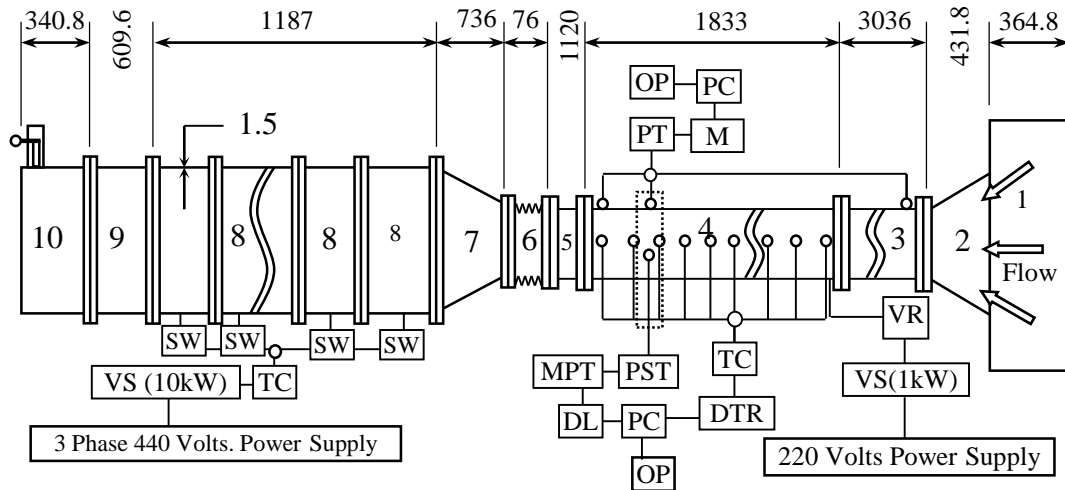
| | | |
|---|---|---|
| 1. Air Filter | 8. Fans      9. Silencer | DL = Data Logger |
| 2. Inlet Contractor | 10. Butter Fly | PC = Personal Computer |
| 3. Unheated Duct | TC = Thermo-couple | OP = Out-put |
| 4. Heated Test Duct | DTR = Digital Temperature Recorder | PT = Pitot Tube |
| 5. Unheated Duct | PST = Pilot Static Tube | SW = Switch |
| 6. Bellow | MPT = Micro Pressure Transducer | VS = Voltage Stabilizer |
| 7. Diffuser | M = Manometer | VR = Voltage Regulator |

Fig: 1 Schematic Diagram of the Experimental Setup

Fig:3. to maintain a constant heat flux a voltage stabilizer followed by a voltage regulator, both having 1kW capacity is used for constant power supply to the heater. The flat nichrome wire of size 28 SWG having the resistance of 9.8097 Ω/m is used to achieve uniform wall temperature condition.

As the thermocouple is attached intrinsically with the pitot static tube, the measurements of both the velocity and the temperature of the air flowing through 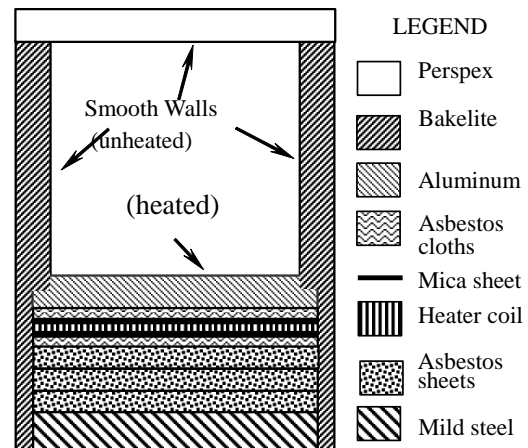the duct are taken simultaneously. Thermocouples are used to measure both wall and air temperature. Two pressure tapings one at the entry and the other at x=4761mm downstream from the leading edge of the test section are used for the static pressure drop measurement.

The heating effect is symmetrical about z-axis but non-symmetric about x- and y- axes, Fig: 3. the presence of the



Fig: 2 Illustrating the Cross sectional View of Duct

bottom heated wall creates asymmetric flow field. To maintain a constant heat flux a voltage stabilizer followed by a voltage regulator, both having 1kW capacity is used for constant power supply to the heater. The flat nichrome wire of size 28 SWG having the resistance of 9.8097 Ω/m is used to achieve uniform wall temperature condition. As the thermocouple is attached intrinsically with the pitot static tube, the measurements of both the velocity and the temperature of the air flowing through the duct are taken simultaneously. Thermocouples are

used to measure both wall and air temperature. Two pressure tapings one at the entry and the other at the working section i.e., x=4761mm downstream from the leading edge of the test section are used for the static pressure drop measurement.
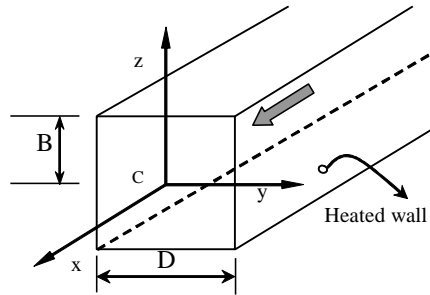
## 4. Measurement System
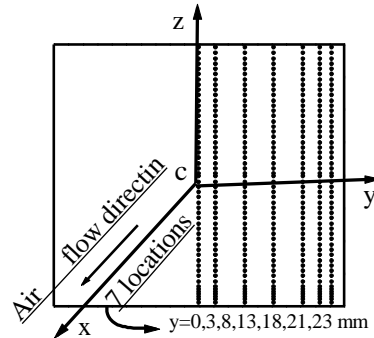


Fig: 3 Geometric Parameters and Wall Coordinate System

Fig:4 Dots represents 105 probe positions in space at each location

The geometric parameters, coordinate system, and the flow direction are schematically shown in Fig: 3. The time mean velocity and the static pressure are measured by the United Sensor (USA) pitot static tube of 1.6 mm outer diameter with a Furnace Controls Ltd. (U.K), pressure transducer (model MDC FC001 and FC012 and a Keithly (USA) digital micro-voltmeter with a data logger system (model 2426). The signals of the pitot static tube are transmitted to pressure transducer through 1.4 mm bore flexible tygon tubing. The signals of the digital micro-voltmeter correspond to the velocity head of the pitot static tube.

Before starting the experiment, the output voltage for the pressure transducer for different range of scale is calibrated in the calibration rig with a Dwyer (USA) slack vertical water tube manometer for the velocity and with an Ellison (USA) inclined manometer, using Kerosene of specific gravity 0.7934, for static pressure measurement. For the measurement of all signals with micro-voltmeter, integration times of about 30 seconds are used. The bottom wall temperatures are measured by 24 copper constant thermocouples distributed along the entire length of the heated portion. The air temperature entering and leaving the heated portion are also measured by two thermocouples.

## 5. Data Reduction

The mean values of time mean velocity and temperature are calculated by integration of the local time mean velocity and temperature profile curve divided by the total length of the curve along the abscissa [5]. The net heat transfer rate can be calculated from,

$$q = \frac{Q}{A_c} = C_P G(\Delta T_{\ln}), \qquad where \quad \Delta T_{\ln} = \frac{(T_{bo} - T_{bi})}{\ln \left[ \frac{(T_{wc} - T_{bi})}{(T_{wc} - T_{bo})} \right]} \tag{1}$$

The local outer wall temperature $T_w$ is read from the thermocouple output. The corrected local inner wall temperature, $T_{wc}$ for Eqn. (1) is calculated by one dimensional heat conduction equation [5] as:

$$T_{wc} = T_w - \left( \frac{Q\delta}{kA_c} \right) \tag{2}$$

The average value of local heat transfer coefficient h is evaluated from,

$$h = \frac{q}{(T_{wc} - T_b)} \tag{3}$$

The coordinate y indicating the location of probe position for measurement are non-dimensionalized by the half width of the duct, B=D/2 as y/B. The flow velocity recorded by data logger in millivolts is converted to velocity in (m/s) and pressure drop in (N/m²) by calibration equations. Thermal conductivity depends on temperature. Since the air velocity and temperature varies along the duct, all the air properties and related parameters are calculated at the bulk mean air temperature and the bulk mean air velocity as given bellow [6]:

$$T_b = \frac{1}{2}(T_o + T_i) \quad and \quad u_b = \frac{1}{2}(u_o + u_i) \tag{4}$$

The local Nusselt's number, friction factor, and Stanton umber are calculated from the following relations as:

$$Nu_s = \frac{hD}{K_f} \tag{5}$$

3

$$f_s = \left(\frac{\Delta p}{\Delta L}\right) \cdot \frac{D}{\left[\rho \bar{u}^2 \Big/ 2\right]} \tag{6}$$

$$St_s = \frac{h}{[\rho c_p u_b]} \tag{7}$$

## 6. Data Analysis

Since the duct is heated asymmetrically at the bottom wall only, it is symmetric about z-axis but asymmetric about the y-axis Fig.:3. The measurements are taken only in one half of the cross section about the symmetrical axis as shown in Fig.:4, which represent the flow characteristics of the entire duct. Measurements are made at the section x=34.5D downstream from the leading edge of the heated section i.e. x=94.56D from the unheated section. In this position both velocity and temperature fields can be considered to be fully developed. The time mean velocity and temperatures of air are measured within the region of -25mm<z<25 mm (i.e. -1<z/B<1) and 0≤y≤23 mm (i.e.0≤y/B≤0.92) at 7 different locations of y = 0, 3, 8, 13, 18, 21, and 23 mm (i.e., y/B=0.0, 0.12, 0.32, 0.52, 0.72, 0.84, and 0.92) in the cross section. The time mean velocity and the temperature are calculated from the probability distribution function of the measurements recorded by the data logger. There are typically 105 measurement points in space at each measuring location and a total of 105×7=735 points in space for half of the cross section of the duct which represents the data for the entire duct cross section. The measurements are taken for 10 different Reynolds Number varying between $5 \times 10^4 <$ Re$< 1 \times 10^5$.

The corresponding statistical error is between 0.55 to 1.85 percent in the time mean velocity and between 1.23 to 2.06 percent in the temperature. The scattering of the wall temperature measurement is found to be between 2.0 to 3.5 percent and the uniformity of the wall temperature distribution is considered to be satisfactory, [9]. The time mean velocity measurements are repeated whenever error or doubtful situations occurred to ensure that the measured results are repeatable.

## 7. Results and Discussions

The longitudinally constant heat flux boundary condition of the present investigation, thermally fully developed region is characterized by wall and air temperature that increases linearly as a function of longitudinal positions, [2] and [6]. The experimental results concerning Nusselt's number, friction factor and Stanton number obtained for a turbulent flow through an asymmetrically heated smooth square duct with constant heat flux as the boundary condition are discussed briefly.

### Nusselt's Number

Fig: 5 show the effect of Reynolds Number on local Nusselt's number at constant pressure drop. At constant pressure drop local Nusselt's number decrease rapidly with negligible decrease of the local Reynolds Number in the region y/B <0.52, but above the region y/B>0.52 towards the side walls the local Nusselt's number increases linearly with the decrease of Reynolds Number. This reflects the effect of the secondary flow in the region 0.72> y/B> 0.32 i. e. the secondary flow carrying primary velocity with higher temperature from the centre of the duct towards the corner along the corner bisector of the duct the mixing up of cold air with hot air and increases the turbulent intensity which intern causes the corresponding air temperature to rise thus increasing the heat transfer there and hence the Nusselt's number increases from the centre towards the side walls. With the increase of static pressure drop the curves shift up towards right. These characteristics are clearly seen in Fig; 6 showing the distributions of local Nusselt's number at constant Reynolds Number across the duct. The local Nusselt's number increases linearly with increase of y/B from centre towards the side walls at constant Reynolds Number. The nature of variation of Nusselt's number with increase of positions y/B, Fig: 6, is similar to that of local variation of heat transfer coefficient. With the increase of Reynolds Number the Nesselts number curve shifts up in a similar manner as that of heat transfer [1]. In the present experimental investigation it is found that on average, with 57.44 percent increase in Reynolds Number the static pressure drop is increased by 185.61 percent and the Nusselt's number is increased by 40.63 percent. Finally the local data in the fully developed region are compared and correlated with Prandl number as variable parameter is shown in Fig: 7. It can be seen that the Nusselt'ss number increases linearly with the increase of Reynolds Number at each location of measurement y/B. Fig: 7 also shows that the curve shifts up with increase of y/B from the centre of the duct towards the side walls. In the present investigation it found that the results obtained compared well the published data. The correlations developed are expressed as follows:

$$\overline{Nu}_{S,V} = 177.47 + 14.89\left(\frac{y}{B}\right) \tag{Fig. 6) (8}$$

$$\overline{Nu}_S = 0.046 \, Re^{0.753} \, Pr^{0.4} \tag{Fig. 7) (9}$$

Symbols for Fig: 5
□ $\Delta p_1$=1.08, ○ $\Delta p_2$=1.26, △ $\Delta p_3$=1.47, ▽ $\Delta p_4$=1.67, ◇ $\Delta p5$=1.85, + $\Delta p_6$=2.09, × $\Delta p_7$=2.46, ✳ $\Delta p_8$=2.67, — $\Delta p_9$=2.88, | $\Delta p_{10}$=3.07.

Symbols for fig: 6
□ Re=55874, ○ Re=60666, △ Re=64029, ▽ Re=67490, ◇ Re=70500, + Re=74043, × Re=79923, ✳ Re=82712, – Re=85366, | Re=87970.

———Solid lines represent present correlations.

Symbols for Fig: 7  □ y/B=0,
○ y/B=0.12, △ y/B=0.32, ▽ y/B=0.52, ◇ y/B=0.72, + y/B=0.84, × y/B=0.92.
- - $Nu_s$, Fujita, 1989;
ᵢ ᵢ $Nu_s$, Mc Adams
- - $Nu_s$, Modified Dittus-Boelter;
- ᵢ - $Nu_s$, flat plate.
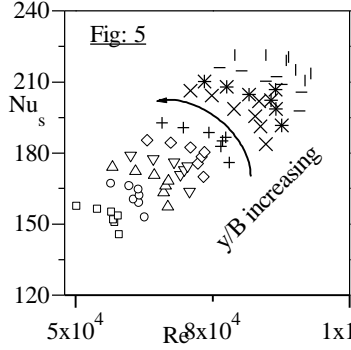


Fig: 5 Effect of Reynolds Number on local Nusselt's number.
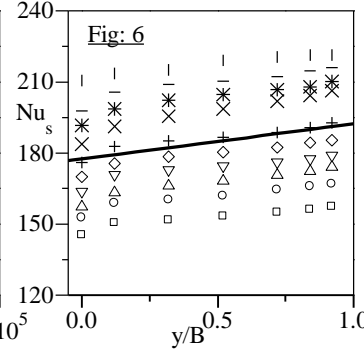
Fig: 6 Distributions of local Nusselt's number.
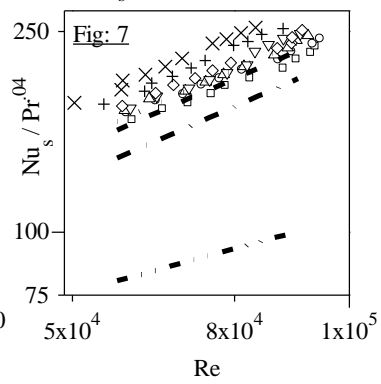
Fig: 7 Comparison of local friction factors.

Symbols for Fig: 8  □ $\Delta p_1$=83.81, ○ $\Delta p_2$=98.05, △ $\Delta p_3$=114.61, ▽ $\Delta p_4$=129.74, ◇ $\Delta p_5$=144.00, + $\Delta p_6$=162.68, × $\Delta p_7$=191.45, ✳ $\Delta p_8$=207.87, — $\Delta p_9$=224.07, | $\Delta p_{10}$=239.35.  $\Delta p$ is in N/m$^2$.

Symbols for fig: 6
□ Re=55874, ○ Re=60666, △ Re=64029, ▽ Re=67490, ◇ Re=70500, + Re=74043, × Re=79923, ✳ Re=82712, – Re=85366, | Re=87970.

Symbols for Fig: 10  □ y/B=0,
○ y/B=0.12, △ y/B=0.32, ▽ y/B=0.52, ◇ y/B=0.72, + y/B=0.84, × y/B=0.92.
- - $f_s$ Blasius (Liou et al., 1992);
. . . $f_s$ Rohsenow & Choi, 1969.

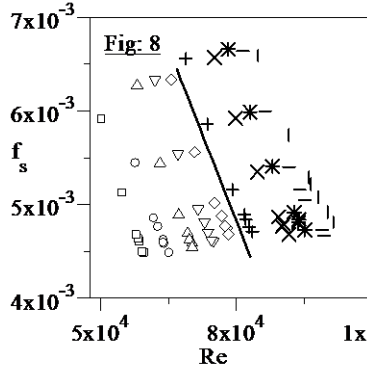———Solid lines represent Present correlations.

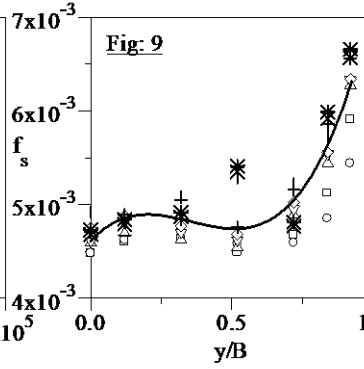Fig: 8 Effects of Reynolds Number on local friction factors.
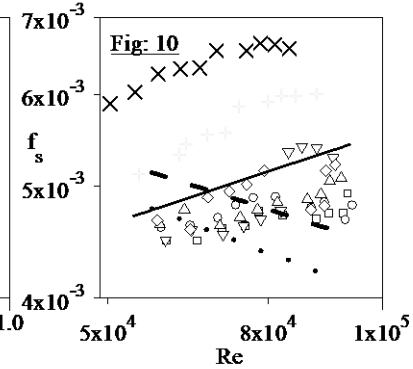
Fig: 9 Distributions of local friction factors.

Fig: 10 Comparison of local friction factors.

These equations (7) and (8) are valid for 80< $\Delta p$< 240 N/m$^2$ and 5×10$^4$< Re< 1×10$^5$ at constant heat flux boundary condition.

The local as well as the average values of Nusselt's number are compared with some of the well-known published data. The secondary flow pattern in the duct is reflected in the local distributions of the Nusselt's number the values of which on the asymmetrically heated bottom wall of the smooth square duct are 1.04 to 1.22 times higher compared with the well-known published data for smooth circular ducts. Since it is found that, for the same experimental set up, the top half of the duct behaves like a flat plat [3], the results are compared with the published data for the flat plate as shown in Fig: 7, the Nusselt's number obtained in the present investigation is 2.32 times higher compared with that of the flat plate.

### Friction Factor and Stanton number
The effects of Reynolds Number on both the local friction factor and the local Stanton number for fully developed flows with constant heat flux are depicted in Fig: 8 and 11 respectively. The characteristics of both curves are similar. Both the local friction factor and the local Stanton number increase linearly at constant

pressure drop with the decrease of Reynolds Number from center towards the side walls. Fig: 8 and 11 also show that with the increase of the pressure drop both the local friction factor and Stanton number curves shifts up towards the right but the corresponding values of friction factor and Stanton number gradually increasing and decreasing respectively with increase of pressure drop Δp. This trend is clearly visible in Fig: 9 and 12, where both the friction factor and Stanton number increase with the increase of y/B at constant Reynolds Number. In Fig: 9 and 12, the distributions of both the friction factor and the Stanton number across the duct at different Reynolds Number are displayed. It is found that with 58 percent increase in Reynolds Number the friction factor and Stanton number increase by 36 percent and 25 percent respectively. These variations of the local friction factor and the Stanton number can be expressed by third degree polynomial equations as follows:

$$\bar{f}_S = 0.0046 + 0.0022\left(\frac{y}{B}\right) - 0.0089\left(\frac{y}{B}\right)^2 + 0.0092\left(\frac{y}{B}\right)^3 \qquad \text{(Fig. 8) (10)}$$

$$\bar{St}_S = 0.0032 + 0.0015\left(\frac{y}{B}\right) - 0.0042\left(\frac{y}{B}\right)^2 + 0.0039\left(\frac{y}{B}\right)^3 \qquad \text{(Fig. 11) (11)}$$

These equations (10) and (11) are valid for $80 < \Delta p < 240 \, N/m^2$ and $5\times10^4 < Re < 1\times10^5$ at constant heat flux boundary condition.

For the same experimental set up and boundary condition the results obtained for both Nusselt's number and Stanton number shown in Fig: 7 and Fig: 13 respectively agree well with published data but the results obtained for the friction factor does not agree as shown in Fig: 10. With the increase of Reynolds Number the viscosity of air increases, the increased heat transfer in the asymmetrically heated duct is achieved at the expense of increased friction due to increase of both primary as well as secondary flow of air flow. Since the viscosity is

Symbols for Fig: 11   □   $\Delta p_1$=83.81,     Symbols for Fig: 12       Symbols for Fig: 13    □   y/B=0,

○   $\Delta p_2$=98.05,   △   $\Delta p_3$=114.61,    □   Re=55874,   ○   Re=60666,    ○   y/B=0.12,   △   y/B=0.32,   ▽   y/B=0.52,

▽   $\Delta p_4$=129.74,   ◇   $\Delta p_5$=144.00,    △   Re=64029,   ▽   Re=67490,    ◇   y/B=0.72,   +   y/B=0.84,   ×   y/B=0.92.

+   $\Delta p_6$=162.68,   ×   $\Delta p_7$=191.45,    ◇   Re=70500,   +   Re=74043,    ▬ ▬   $St_s$ McAdams.

✳   $\Delta p_8$=207.87,   −   $\Delta p_9$=224.07,    ×   Re=79923,   ✳   Re=82712,    ⌐   ⌐   $St_s$ Modified Dittus-Boelter.

ǀ   $\Delta p_{10}$=239.35.             −   Re=85366,   ǀ   Re=87970.    Solid lines represent Present correlations:
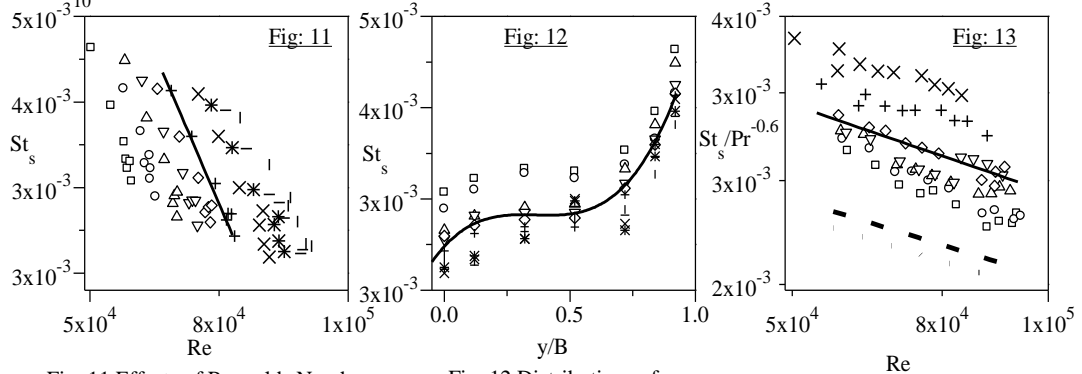


Fig: 11 Effects of Reynolds Number on local Stanton number.

Fig: 12 Distributions of local Stanton number.

Fig: 13 Comparions of Stanton numbers.

increasing with the increase of Reynolds Number the friction factor must also increase. Also it can be seen in the Darcy's formula, $f = \dfrac{(\Delta p/\Delta L)/D}{\frac{1}{2}\rho\upsilon^2}$, $f \propto \dfrac{\Delta p}{u^2}$, assuming all other parameters are constant, the ratio of $\dfrac{\Delta p}{u^2}$

increases with the increase of pressure drop. Hence the friction factor increases with the increases of Reynolds Number instead of decreasing as that of the published data. The improved correlations obtained are as follows:

$$\bar{f}_S = 0.003\, Re^{0.261} \qquad \text{(Fig. 10) (12)}$$

$$\bar{St}_S = 0.0034\, Re^{-0.221}\, Pr^{-0.6} \qquad \text{(Fig. 13) (13)}$$

These equations (12) and (13) are valid for $5\times10^4 < Re < 1\times10^5$ at constant heat flux boundary condition.

In the present investigation the friction factor obtained increases with the increase of Reynolds Number instead of published data where it decreases or approaches a constant value for smooth noncircular ducts. Comparing with the published data the friction factor and the Stanton number the results obtained in the present investigations are respectively 1.07 to 1.17 and 1.17 to 1.20 times higher than those of smooth circular duct. The results are presented in their final concise form of compact correlations that involve dimensionless groups which

represent the characteristics of the friction factor and the Stanton number. These correlations can be used for improved numerical analysis and for better design of heat transfer equipment for engineering applications.

## 8. Acknowledgments

## 9. References

[1] A.K.M.A. Hamid, A.R. Akanda, and M.A.T. ALI, "The Time Velocity and Temperature Fields in Developed Region in an Asymmetrically Heated Smooth Square Duct." *Journal of Engineering and Technology*, ISSN 1684-4114, Vol. 9 No. 2, December 2011.

[2] A.K.M.A. Hamid, "Experimental Study on Convective Heat Transfer with Turbulence Promoters", *Ph.D. thesis*, Bangladesh University of Engineering and Technology, Dhaka, Bangladesh, 2004.

[3] F.B. Gessner,"Turbulence and Mean-flow Characteristics of Fully Developed flow in Rectangular Channels," *Ph.D. Thesis*, Dept. Mech. Engg. Purdue University, 1964.

[4] F.B. Gessner, and A.F. Emery, "A Length-Scale Model for Developing Turbulent Flow in a Rectangular Duct," *ASME Journal of Fluids Engineering,* Vol. 103, pp. 445-455, 1981.

[5] J.C. Han, "Heat Transfer and Friction in Channels with Two Opposite Rib-Roughened Walls," *ASME Journal of Heat Transfer*, Vol. 106, No. 4, pp. 774-781, 1984.

[6] M. Hirota, H. Fujita, and Yokosawa, "Experimental study on convective heat transfer for turbulent flow in a square duct with a ribbed rough wall (characteristics of mean temperature field)," *ASME Journal of Heat Transfer*, Vol. 116, pp.332-340, 1994.

[7] W.M. Kays, and M.E. Crawford, "Convective Heat and Mass Transfer", *McGraw-Hill*, New York, 1980.

[8] S.J. Kiline, and F. A. McClintock, "Describing Uncertainties in Single-Sample Experiments," *Mechanical Engineering*, Vol. 75, pp. 3-8, 1953.

[9] K. Komori, A. Iguch, and R. Iguni, "Characteristics of fully developed Turbulent flow and Mass Transfer in a Square Duct." *International Chemical Engineering*, 20. (2), pp. 219-225, 1980.

## 10. Nomenclature

| | | |
|---|---|---|
| A = Area | m$^2$ | |
| B = Half of width of duct | M | |
| C = Specific heat, Centre | W.s/kg$^O$C | |
| D = Hydraulic diameter of duct | M | |
| f = Friction factor | Dimensionless | |
| G = Mass flux | Kg/m$^2$s | |
| h = Heat transfer coefficient | W/(m$^2$, $^0$C) | |
| k = Thermal conductivity | W/(m, $^0$C) | |
| L = Length | M | |
| Nu = Nusselt number | Dimensionless | |
| P = Pressure | N/m$^2$ | |
| Pr = Prandtl number | Dimensionless | |
| q = Heat flux | W/m$^2$ | |
| Q = Heat transfer | W | |
| Re = Reynolds' number | Dimensionless | |
| Re = Reynolds' number | Dimensionless | |
| T = Mean temperature | $^0$C | |
| x,y,z = Coordinate system | | |

## 10.1 Greek letters

| | |
|---|---|
| $\tau$ = Shear stress | N/m$^2$ |
| $\nu$ = Kinematics iscosity | m$^2$/s |
| $\rho$ = Density | kg/m$^3$ |
| $\delta$ = Aluminum wall thickness | Mm |

## 10.2 Subscripts

| | |
|---|---|
| a = Ambient temperature | f = Fluid |
| b = Bulk mean | i = Inlet |
| C = Centre, correct | in = Input |
| L = Loss | m = Mean |
| o = Outlet | w = Wall |
| s = Smooth duct, surface | ln = Log mean |

# Development of a Pump Test Bed

M. E. Haque[1], M. R. Islam[1], M. M. Islam[1], M. M. Islam[1], A. Roy[1], H. Haniu[2]

[1]Department of Mechanical Engineering, Rajshahi University of Engineering & Technology, Bangladesh
[2]Department of Mechanical Engineering, Kitami Institute of Technology, Kitami City, Hokkaido 090-8507, Japan
Email: emdad359456@yahoo.com

## Abstract

*In this study a pump test bed has been designed for characterization of both centrifugal and submersible pumps of capacity up to 6 cusec. The pump test bed will be installed in the Fluid Mechanics Lab of Mechanical Engineering Department, Rajshahi University of Engineering & Technology, Bangladesh. Complete two sets of pump test setup will be therein. One for small pumps of capacity up to 3 cusec and other up to 6 cusec. The each complete setup are comprised of Mild Steel (MS) pipe, elbow, tee joints, gate valves, motorized flow control valve, check valves, water flow meter and pressure gages in their proper position and alignment; and with supplying and welding 25 mm thick MS flanges to pipe bend/joint and supplying 2 Nos. 3 mm thick rubber gasket in each joints for making the joints water tight.*

**Keywords:** Centrifugal and submersible pumps, Pump test bed, Technical specifications

.

## 1. Introduction

Pumping systems account for nearly 20% of the world's electrical energy demand and range from 25-50% of the energy usage in certain industrial plant operations [1]. Pumping systems are widespread; they provide domestic services, commercial and agricultural services, municipal water/wastewater services, and industrial services for food processing, chemical, petrochemical, pharmaceutical, and mechanical industries. The energy and materials used by a pump depend on the design of the pump, the design of the installation, and the way the system is operated. These factors are interdependent [1-3].

The demand for submersible pumps has been rising recently. World leading pump companies are continually building up the share of submersible pumps in their production volumes. While 50 years ago submersible pumps with air-filled electric motors were produced by only one company, by the 1990s all of the ten leading manufacturers of pumps produced submersibles. These companies, which together account for a third of the world market, dictate their policy to the remaining 10000 pump manufacturers [2-3].

During the draught season, the ground water goes down at lower level. It is generally caused when the groundwater heads in an aquifer fall below a critical level over a certain period of time due to natural or human induced causes and inventions. In the recent past, there was increased frequency of draughts in Bangladesh. Particularly, the Northern region of the country was severely affected by the occurrence of draughts and high variability in rainfall. At that time, farmers had to face tough situation due to scarcity of water and they had to dependent on ground water for irrigation. As the ground water level is declining day by day, it is almost impossible to lift water by low lift pump like centrifugal pump for irrigation, drinking and industrial purposes today. It has become urgent to lift water by high lift pump like submersible pump for irrigation and other purposes. Barind Multipurpose Development Authority (BMDA) takes initiatives for irrigation using ground water by installing deep well and supply drinking water in barind area where the depth of ground water level is high [4-5].

There are variety brands of centrifugal/submersible pumps available in the market place. Some of them are cheap but shorter lifespans and high maintenance and energy consumption costs. These cheapest brands pump draw primary interest of the most customers. Some other brands have comparatively longer lifespan with low maintenance and energy costs. The customers do not feel interest for high price of these pumps that is very smaller than the energy consumption cost during its life. Under these circumstances it is crucial to obtain an optimum solution for selecting a good pump and also operation of submersible pumps. However, the main objectives of the present study is to develop a pump test bed for characterization of both centrifugal and submersible pumps in the Fluid Mechanics Lab of Mechanical Engineering Department, Rajshahi University of Engineering & Technology, Rajshahi, Bangladesh.

## 2. Basis of Design

The BMDA and Rajshahi WASA are using submersible pumps to supply water mainly for irrigation in sixteen districts of Northern part of Bangladesh and for house hold affairs in Rajshahi City Corporation respectively. Most of them are of pumping capacity of two cusec. Sometimes they uses centrifugal pumps of capacity up to 5 cusec for transferring surface water and hence a pump test bed has been designed of capacity up to 6 cusec for characterization of pumps under head of 335ft.

### 2.1 Pipeline

The pump test bed will be fabricated by fitting, fixing and installation of MS pipes inside and outside of the Fluid Mechanics and Energy Lab including cutting, shaping, trimming and clearing the ends of the pipes. The minimum wall thickness of the pipes is considered 6mm by the supporting calculation bellow [6-7]. The pipe shall be capable to withstand a working pressure of 10 bar that is equivalent to 335ft head. Before installation the pipes and other components shall be coated with tar epoxy resin for the internal part and for the external part with bitumen reinforced with an inner layer of fiber glass tissue and an outer wrapping of bitumen impregnated reinforced glass tissue excepting exposed pipe work. The 6 inch (150mm) diameter pipe is considered for smaller pump test bed and 10 inch (250mm) pipe is considered for bigger pump test bed for reducing the thrust on the pipe and pipe fittings.

The free body diagram for bursting force in the pipeline is shown in Fig. 1. The total bursting force $F$, acting normal to the cutting plane A-A, is resisted by equal forces acting on each cut surface of the pipe wall. Applying a horizontal summation of forces,

$$[\Sigma F_x = 0]; \quad F = pDL = 2P \quad (1)$$

Here the left half of the cylinder is occupied by water, from the accompying free body diagram it is apparent that the bursting force $F$ acting over the flat surface of the fluid equals the pressure intensity $p$ multiplied by the area $DL$ over which it acts as $pDL$.
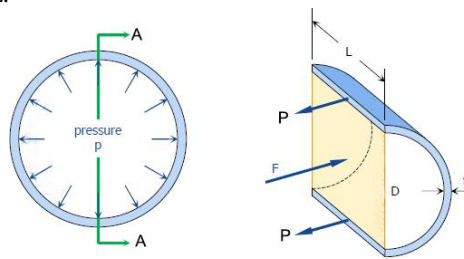


Fig.1: Direct evaluation of bursting force

The stress in the longitudinal section that resist the bursting force $F$ is obtained by area of two cut surfaces. This gives,

$$[\sigma_t = \frac{F}{A}]; \quad \sigma_t = \frac{PD}{2t} \quad (2)$$

This stress is tangential stress or hoop stress or girth stress, it is practically equal to the maximum stress at inside surface. If we consider that the pumps work under 335 ft head with 10 inch dia pipe then the resulting pressure inside the pipe line is 10 bar that is calculated by the well-known equation $p = \rho g h_T$. Thus, the designed pipe wall thickness for mild steel ($\sigma_t = 248MPa$) with safety factor 3 is obtained by using Eq$^n$. (2):

$$t = \frac{pD}{2\sigma_t} = \frac{\rho g h_T D}{2\sigma_t} = \frac{1000\times9.81\times102.74\times0.250}{2\times\frac{248}{3}\times10^6} \quad \text{Where, } h_T = h + V^2/2g)$$

$$= 0.0015m$$

$$= 1.15mm$$

In similar way the minimum wall thickness for 6 inch dia pipe is found as 0.92mm.

Bursting force on a transverse section: If we consider free body diagram of Fig. 2 of a transverse section, we can see that the bursting force acting over the end of the cylinder is resistant by the resultant P of tearing forces acting over the transverse section.

The bursting force on traverse section is calculated by the following Eq$^n$.
Bursting force for 10inch (250mm) diameter Pipe:

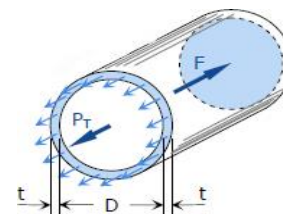$$F_B = PA_1 = \rho g h_T A_1 \quad (here \; h_T = h + V^2/2g)$$



Fig.2: Bursting force on transverse section

$$= 1000 \times 9.81 \times 102.13 \times .04909 = 49183 \text{ N}$$

The yield strength of traverse section, $\sigma_t = F/A_2;$  Where, $D_2 = D_1 + 2t$
$$= 49183/0.0502 = 979741 \text{ N/M}^2$$

In similar way the bursting force and yield strength for 6 inch dia pipe is found as 17733 N and 979723 N/M², respectively.

## 2.2 Elbow

MS elbow inside and outside of the Fluid Mechanics and Energy Lab will be fitted in their proper position including cutting, shaping, trimming and clearing the ends of the elbow. The minimum wall thickness of the elbow is also considered as 6mm. The elbow shall be capable to withstand a working pressure of 10 bar as minimum. Before installation the elbow shall be coated with tar epoxy resin for the internal part and for the external part with bitumen reinforced with an inner layer of fiber glass tissue and an outer wrapping of bitumen impregnated reinforced glass tissue excepting exposed elbow work.

Thrust on elbow, for 10 inch (250 mm) dia pipe: Fluid flow and internal pressure in a piping system may create intolerable forces and tensions without adequately supporting of the piping structure.

The thrust on elbow for discharge of 6 cusec and using 10 inch (250mm) diameter pipe can be expressed as,

$F_T = m (V_1 - V_2)$
$\quad = \rho AV (V - V\cos\alpha)$
$\quad = \rho A V^2 (1 - \cos\alpha)$
$\quad = \rho AV^2$      (for $\alpha = 90^0$)
$\quad = 1000 \times 0.04909 \times (3.46)^2$    (V = Q/A)
$\quad = 588.02 \text{N}$

Similarly, for discharge of 3 cusec and 6 inch
diameter pipe the thrust on elbow is found
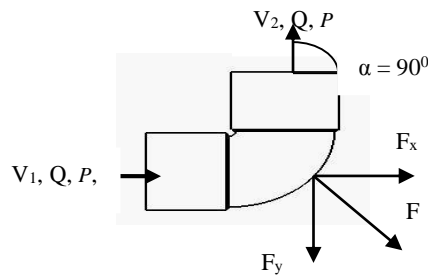as 406.11N



Fig. 3: Thrust force on elbow

## 2.3 Gate valves of diameter 150mm and 250mm

All valves shall be flanged, cast iron with gun metal wedge and rings, mornings with gun metal or stainless steel spindle and nuts. In order to ensure easy manual operation, valves should have hand wheel for closing in clockwise rotation marking "To close" and for opening in anti-clockwise rotation marking "To open" during casting, indicating with arrow. Provision should also be there for indicating the degree of opening. Designed working pressure shall be 10 bars as minimum.

## 2.4 Flanges of diameter 150mm and 250mm

The relevant requirement of BS 4504 is applicable to the 25mm thick (minimum) flanges. Jointing materials e.g., nuts-bolts, gasket, glands, sealants shall be provided for flanges where required to ensure proper joining and minor adjustment of pipe installation against the leakage. For easy replacement, packing of gland shall be arranged. In the first type flanged ends of the pipes or fittings are brought together and cotton fiber reinforced gaskets or rubber washers are placed in between the flanges to ensure water tightness and both the ends of the pipes are flanged with wholes in order to fix the bolts; the whole arrangement is finally tightened with the nuts. In the second type rubber gasket is pressed tightly between the annular space of spigot and socket with the aid of bolts, the socket end is flanged with cast iron or steel ring to slide freely on the spigot part and extra care is required during tightening of the bolts.

Stud bolt design: For 10 inch (250 mm) dia pipe, the dia. of the bolt is found by the following Eqⁿ. considering 12 nos of bolts to be used in a flange

$$\sigma_t = \frac{F}{A \times 12} = \frac{(F_T + F_B)}{A \times 12}$$

Diameter of stud bolt, $\quad d = \sqrt{\dfrac{F_T + F_B}{\pi \times \frac{\sigma_t}{4} \times 12}} = \sqrt{\dfrac{588.02 + 49183}{\pi \times \frac{248 \times 10^6}{4 \times 3} \times 12}} = 8 \text{ mm}$

Considering 8 nos of bolt for 6 inch dia flange, in similar way the bolt dia. is found as 4.83mm. Nominal size of bolt dia. to be used in flange for 10 inch and 6 inch pipes are 20mm and 15mm, respectively. Thus, the design is in safe condition.
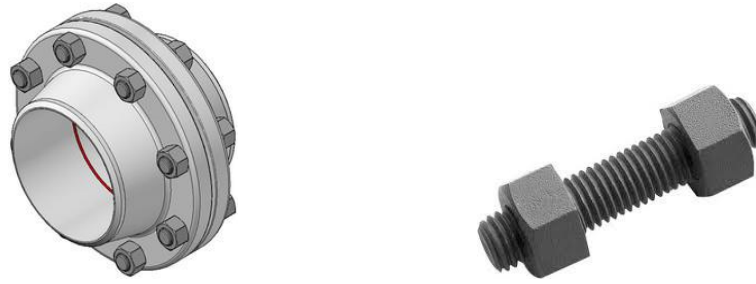
Fig.4: Flange and stud bolt

**2.5 Motorized flow control valve of diameter 150mm with range up to 500 m³/h and 250mm with range up to 1000 m³/h**

Motorized flow control valves of any reported international brand with the following requirements will be installed: valve material: stainless steel 304/316, connection type: flange connection, operating pressure: 0 to 10 bar, operating temperature: 15 to 150° C, valve opening indication: provision should also be there for indicating the degree of opening. , actuator type: electric motor, actuating time: 1 sec/mm (approximate), actuating thrust: 10-15 kN, power supply: 220-240 VAC, frequency: 50/60 Hz, electronic type: input signal 4-20mA, feedback signal 4-20mA, enclosure protection: IP 54.

**2.6 Water flow meter of diameter 150mm and 250mm**

Water flow meter of any international brand with maximum working Pressure: 10 bar, connection type: flange connection , flow rate: 50 m³/h to 1000 m³/h , accuracy: about ±3% f.s. the materials for the main components of the water flow meter comply with the following requirements:, housing: stainless steel (AISI 316L) with IP65-coated aluminum, scale plate: coated aluminum, window: polycarbonate , closing disk: stainless steel (AISI 316L), magnet group: stainless steel (AISI 316L) +alnico (coated) bearing: poly tetra fluoro ethylene (PTFE) / bronze, shaft support disk: stainless steel (AISI 316) ,spring: stainless steel (AISI 304), shaft: stainless steel (AISI 316). disk stop: stainless steel (AISI 316L) , disk: stainless steel (AISI 316Lbody: polyamide coated steel (AISI 316L).

**2.7 Check valve of diameter 150mm and 250mm**

Double door type compact design check valve shall be fitted between flanges. The doors of check valve to be spring loaded, closed by means of one or more heavy duty stainless steel torsion springs. Door is opened with the flow from the pump and when shut down, the torsion spring shuts the door before reverse flow stars at the point of nil velocity, for non-slain close. The seating shall be watertight and resilient. Provision for lifting hook is required. The deigned working pressure shall be 10 bar as minimum. Cast iron body conforming to BS 5153 clasic-16. Aluminum bronze doors conforming to BS 1400, grade LG-2 T 136 steel shall be used for stop pins and hinges. Buna-N molded to the body to be used as scaling element. Similarity with either No. 9000 series or mission style-B shall be maintained for construction. These are suitable for installation between BS 4504 class NP 10 flanges.

**2.8 Tee joint of diameter 150mm and 250mm**

Fitting, fixing and installation of MS Tee joints inside the Fluid and Energy Lab including cutting, shaping, trimming and clearing the ends of the Tee joint. The minimum wall thickness of the Tee joint is 6mm. The Tee joints shall be capable to withstand a working pressure of 10 bar as minimum. Before installation the Tee joint shall be coated with tar epoxy resin for the internal part and for the external part with bitumen reinforced with an inner layer of fiber glass tissue and an outer wrapping of bitumen impregnated reinforced glass tissue excepting exposed Tee joint work .

**2.9 Pressure gages of range 0 to 10 bar**

Supplying, fitting and fixing pressure gages with the following requirements: pressure element: bourdon tube (stainless steel 316L, C-type or helical type), dial: aluminum, white of 15cm dia (minimum), black/red lettering, NS 63 with pointer stop pin., pointer: aluminum, black/red, case: stainless steel, window: laminated safety glass (NS 63: polycarbonate), ring: cam ring (bayonet type), stainless steel ,accuracy: 1.5 (minimum), case filling: with glycerin.

**2.10 Vacuum pressure gages of 0 to -1 bar**

Supplying, fitting and fixing vacuum pressure gages with the following requirements: pressure element: Bourdon tube (AISI 316L seamless tube), dial: Aluminum, white of 13cm dia (minimum), black/red lettering, NS 63 with pointer stop pin,   pointer: Aluminum, black/red, case: Bayonet ring, 1.4301 (304 stainless

steel),window: Laminated safety glass, ring: Cam ring (bayonet type), stainless steel, accuracy: 1.5 (minimum),case filling: with glycerin.

### 2.11 Foundation/base for complete pump test setup
Each of the two complete pump test setup should be mounted at proper position/elevation by making suitable foundation/base. The position/elevation of pipeline, valves, all meters etc. should be suitable for taking reading easily. The foundation/based must be made by 100mm dia and 6mm thick MS pipe with concrete base.

### 2.12 Star-Delta control panel including capacitor bank
45 kW Star Delta 3 phase pump motor starter with voltage control coils fitted with panel board complete for up to 60 HP pumping system comprising of incoming circuit breaker of sufficient capacity, ammeter with ASS, volt meter with VSS, C/T of proper current ratio and burden, indication light for three phase indicator, comprising main contractor, auxiliary contractors, thermal over load relay, timer, ON/OFF push button, indicating light for ON/Trip, electronic relay for protection against phase failure, phase reverse and dry run, complete with necessary wires, cable lugs, cable ties, connectors capacitor bank. The start delta unit is provided with a timer for automatic changeover of star delta to reduce the voltage and current of motor starting.

### 2.13 Trolley cum base for centrifugal pump
The centrifugal pump and motor shall have to be mounted on a rectangular trolley cum base. Then the pump and motor will be coupled and fixed through coupling flanges and flexible disc. The required coupling flanges, disc, coupling pin and nut-bolts etc. are to be supplied by the bidder/supplier. The trolley/base is to be fabricated out of new mild steel channel section. The cross sectional dimension of the trolley/base will be as follows: frame: 1530mm×460mm×125mm/matching with pump motor set (should be made of 150mm×75mm×8mm channel) , steel angle (all through), wheel size: dia.38 cm, width10 cm and disc thickness 9mm., foot Bars: 51mm×25.4mm-2 nos. at diagonal ends., tow bar: A detachable tow bar fabricated out of min 40mm diameter with mild steel (M.S.) shall have to be provided., dimension of the trolley cum base must be suitable for mounting of the different size of pump coupled with motor. The trolley cum base should be designed by the supplier and get it approved by the authorized representative of the purchaser before fabrication.

### 2.14 Welding work
 Desired welding rods having about 2.5 kg/sq.cm tensile strength shall be used for all welding works. To handle high pressure welding sufficiently experienced welders shall be selected. In order to ensure perfect penetration of metals during welding, shims may be used. For carrying out butt-welding base plate joints should be placed face to face. With a view to avoiding and wrapping due to over-heat, continuous single in welding must not be done. Precautions to be taken in course of subsequent runs which has to be executed after a thorough cleaning, chipping and grinding the previous welding. Disc grinder for penetrated side finishing and for final finish, light welding to be provided. The steel pipes including fittings shall be welded quality.

When all component have been jointed together completely hydraulic tests to be started on the full length of the complete setup.  Two sets of centrifugal and submersible pump motor will be provided for testing both of two setups. The pumping is done at a pressure of 6 bars (minimum), it is kept steady for 4 hours and finally the loss of water in the tank is detected. The maximum leakage shall be maximum 0.1 liter/mm of pipe diameter per kilometer per 24 hours for the applied pressure. If the losses are more, the pipeline shall be declared unacceptable and shall have to be re-laid. Care should be taken that the pipeline and pipe work shall be tested immediately after installation and before it is covered with filling materials.

### 2.15 Painting
 Painting pipes and other fittings with super gloss enamel paint of two coats over a red oxide primer after proper cleaning of surface as per direction of the Engineer in charge.

## 3. Assembly and trial run
Basically this setup is considered of two circuit and the water flow is controlled by three valves in each circuit. The complete assembled pump test bed is presented in Fig. 5. Two of them are gate valves and denoted by $V_1$ and $V_2$. These gate valves which is used to vary internal pressure of flow by changing the gate opening which is ultimately used directly to calculate the head. Another one is motorized flow control valve .This valve is denoted by $V_3$. The flow diagram for one set of pump test bed is shown in Fig. 6. The discharge is measured by flow meter. When centrifugal pump is attached to the setup, valve $V_2$ is kept close and valve $V_1$ and $V_3$ remains open to flow the water from pump to measuring tank.  When submersible pump is attached to the setup, valve $V_1$ is kept close and valve $V_2$ and $V_3$ remains open to flow the water from submersible pump to measuring tank.
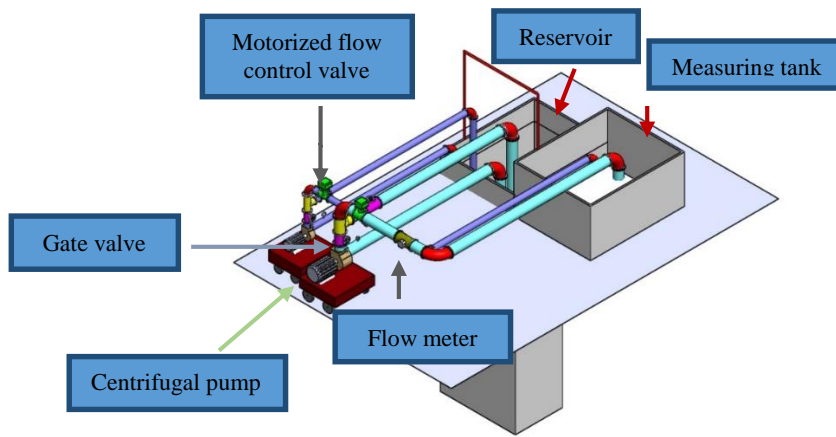
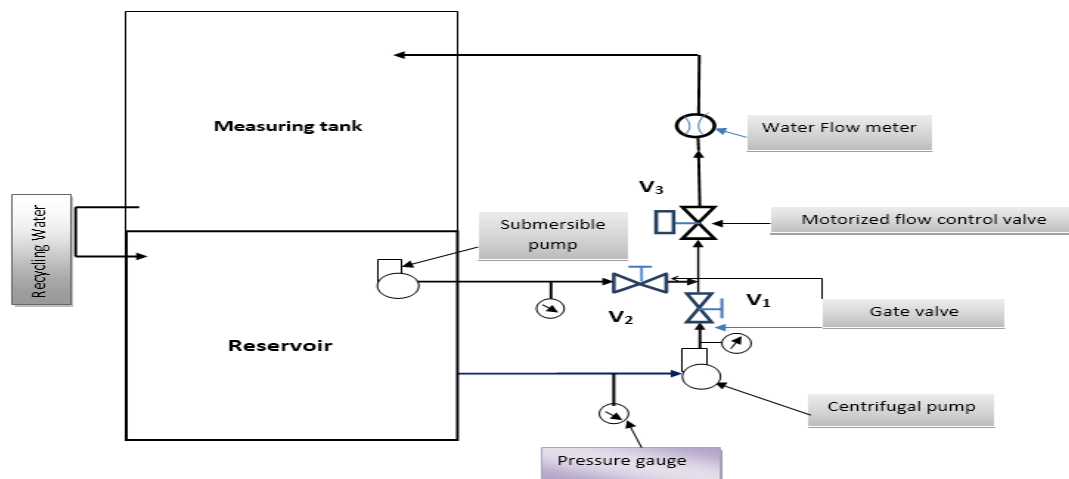Fig. 5: Assembly of pump test bed



Fig.6: Flow diagram of a single set pump test bed

## 4. Conclusions

The total successful design has been completed considering all issues for a pump test bed. Operating requirements may sometimes override energy cost considerations; an optimum solution is still possible. A greater understanding of all the components that make up the total cost of ownership for the pumps will provide an opportunity to dramatically reduce energy, operational, and maintenance costs.

## 5. Acknowledgement

## References

[1]   Wet and dry installation of submersible pumps. World Pumps, www.worldpumps.com, October 2007.

[2]   Optimizing operational efficiency in submersible pumps. World Pumps, www.worldpumps.com, April 2004.

[3]   Energy cost savings with centrifugal pumps. Word pumps, www.worldpumps.com, March 2009.

[4]   A survey report on water pumping under BMDA. BMDA, Rajshahi, Bangladesh, September 2015.

[5]   A survey report on water pumping under Rajshahi WASA. Rajshahi WASA, Bangladesh, September 2015.

[6]   F.L. Singer, A. Pytel, Strength of Materials, Harper & Row Publishers, New York, Third Edition, pp. 24-26, 1980.

[7]   D. S. Kumar, Fluid Mechanics and Fluid Power Engineering, S. K. KATARIA & SONS, New Delhi, Seventh Edition, pp. 930-31, 2012.

# Thrust Produced by Four Fingers of a Swimmer at a Low Re

Md. Mahbub Alam[1], Guoqing Xu[1], Kerry Hourigan[2], Shafiqur Rehman[3]

[1]Institute for Turbulence-Noise-Vibration Interaction and Control, Shenzhen Graduate School, Harbin Institute of Technology, Shenzhen Graduate School, Shenzhen, China
[2]Fluids Laboratory for Aeronautical and Industrial Research (FLAIR), Department of Mechanical and Aerospace Engineering, Monash University, Clayton 3800, Australia
[3]Center for Engineering Research, Research Institute, King Fahd University of Petroleum and Minerals, Dhahran-31261, Saudi Arabia

*E-mail: alamm28@yahoo.com; alam@hitsz.edu.cn*

## Abstract

*Thrust produced by a swimmer might be connected the spacing between the four fingers. It is thus crucial to examine fluid dynamics around four side-by-side fingers. Flow structure and fluid forces acting on four identical side-by-side circular cylinders placed normal to the oncoming flow is numerically simulated using the finite volume method (FVM) at a low Reynolds number Re = 100, based on cylinder diameter D and freestream velocity. How the wake structure, forces and vortex shedding patterns are contingent on the cylinder gap spacing ratio g\* (= g/D) between the cylinders is studied systemically when g\* varies from 0 to 2. Based on the intrinsic features of the flow, four distinct flow regimes are identified in the range of g\*-examined. The total time-mean drag force acting on the four cylinders escalates exponentially with a decrease in g\*, as does the lift force, repulsive, on each cylinder.*

Keywords: drag force, four fingers, cylinders, swimmer, flow, wake.

## 1. Introduction

A large portion of forward thrust of a swimmer comes from palm and fingers. Propulsive forces generated by swimmers' palm/fingers should also be studied to find the optimum spacing between the fingers. Two side-by-side circular cylinders are considered as the simplest model to understand the fluid dynamics around more structures in groups. Alam et al. [1] experimentally investigated the aerodynamics of two side-by-side circular cylinders at a Reynolds number of $5.5 \times 10^4$, identifying four distinct flows depending on the gap spacing between the cylinders. The flows were distinguished not only by their structures, but also by shedding frequencies and fluid forces.

While a number of similar studies have been carried out for two circular cylinders in side-by-side arrangement, quite less attention has been paid to examine the fluid dynamics around more than two cylinders, where much more complex flow is involved. Some features of flow around multiple cylinders can be predicted based on the fluid dynamics knowledge of two cylinders but some are not, requiring investigation on more than two cylinders.

The objective of this investigation is to study the hydrodynamics of and drag forces acting four cylinders representing the four fingers of a hand at a low *Re* = 100.

## 2. Computation

Unsteady two-dimensional laminar flow of viscous incompressible fluid is considered. The finite volume method (FVM) with a structured quadrangular grid is employed to solve the unsteady two-dimensional incompressible Navier-Stokes equations. The dimensionless 2-D Navier-Stokes equations governing the flow of a Newtonian fluid can be written in vector form as

$$\left. \begin{array}{l} \dfrac{\partial \boldsymbol{u}}{\partial t} + \boldsymbol{u} \cdot \nabla \boldsymbol{u} = -\nabla p + \dfrac{1}{Re} \nabla^2 \boldsymbol{u} \\[2mm] \nabla \cdot \boldsymbol{u} = 0 \end{array} \right\} \qquad (1)$$

where $\boldsymbol{u}$ is the non-dimensional flow velocity vector in the Cartesian coordinate system $(x, y)$ with its two velocity components $u_1$ and $u_2$; the dimensionless static pressure is denoted by $p$; $Re$ is the Reynolds number based on the free-stream velocity $U_0$ and cylinder diameter $D$. The $Re$ is is kept constant at $Re = 100$.
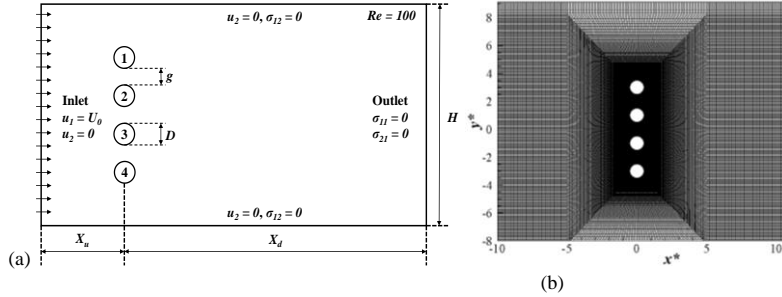


**Fig. 1** (a) Computational domain, boundary conditions and symbol definitions, (b) grid system around the cylinders.

Fig. 1(a) shows a schematic diagram of the computation domain, cylinder arrangement, definitions of symbols and boundary conditions. The gap width between the cylinders is defined by $g$, normalized as $g^* = g/D$. An appropriate computational size of $X_u = 10D$, $X_d = 25D$ and $H = 80D$ is chosen, giving a converged output (Fig. 1). An O-xy grid system near the cylinders and a rectangular-grid system away from the cylinders were used (Fig. 1b). The number of grids for the O-grid system was 200 in the transverse direction. Therefore, a total of 200 points were on the cylinder surface. The grid in the radial direction was denser near the cylinder surface with the nearest grid being $0.005D$ away from the cylinder surface. On lateral surfaces, the velocity component normal to the boundaries and the stress vector component along the boundaries are set to zero. The no-slip boundary condition is applied at the cylinder walls. All simulations start with the initial velocity $u_1 = U_0$, $u_2 = 0$. Grid and time independence test was done first, and then flow past a single circular cylinder was simulated to validate the numerical model used. The comparison of current results (time-mean drag $C_D$, fluctuating lift $C_L'$ and Strouhal number $St$) with those published in the literature states a good agreement (Table 1).

**Table 1.** Comparison of results for a single cylinder at $Re = 100$.

|           | $C_D$ | $C_L'$        | $St$  |
|-----------|-------|---------------|-------|
| Present   | 1.37  | 0.288         | 0.165 |
| [2], Exp. | --    | --            | 0.164 |
| [3], Exp. | --    | 0.18 ~ 0.54   | 0.168 |
| [4], CFD  | 1.37  | --            | 0.165 |
| [5], CFD  | 1.36  | 0.287         | 0.166 |

## 3. Results and Discussion

### Flow structures

$g^* = 0$, 0.25, 0.5, 0.75, 1.0, 1.25, 1.5, and 2.0 are simulated systematically. Fluid dynamics, flow structures and forces acting the cylinders are investigated at each $g^*$. Four distinct flow regimes are observed in the range of $g^*$ examined.

*Interlocked flow ($g^* \geq 2.0$)* Four cylinders each generates a vortex street that resembles a single cylinder's street (Fig. 2a). The four streets and the shedding from the cylinders are however interlocked in an inphase fashion. The inphase flow can further be confirmed by the time-histories of lift forces of the four cylinders (Fig. 2b). The two outer cylinders (cylinders 1 and 4) have the same amplitude of lift, larger than that of the inner cylinders (cylinders 2 and 3). The time-mean value of the lift is, however, positive for the upper two (cylinders 1 and 2) and negative for the lower two (cylinders 3 and 4), implying that all the cylinders experience a repulsive lift force about the centerline $y^* = 0$ of the four cylinders. While the lift fluctuations of the two inner cylinders are exactly inphase, those of the two outer cylinders are also inphase but with a phase lag $\delta\phi = 35°$ with respect to

the inner cylinders. All the lift signals corresponded to the same $St = 0.194$ obtained from the power spectra of lift forces, which is ~18% higher than for an isolated cylinder.
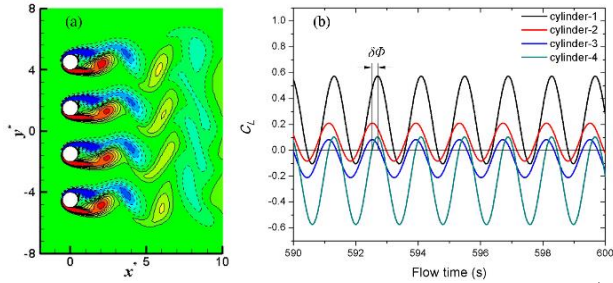


**Fig. 2.** (a) Instantaneous vorticity contours and (b) time-histories of lifts at $g^* = 2.0$.

***Quasi-interlocked Flow (1.0 ≤ g\*< 2.0)*** When $g^*$ is decreased to $1.0 \leq g^* < 2.0$, the flow becomes chaotic. Figure 3 displays instantaneous vorticity contours and time-histories of lift forces at $g^* = 1.5$, demonstrating that the sheddings from the two outer cylinders, with an identical frequency, are interlocked almost inphase, and those from the other two, with another identical frequency, larger than the prior, are interlocked antiphase.
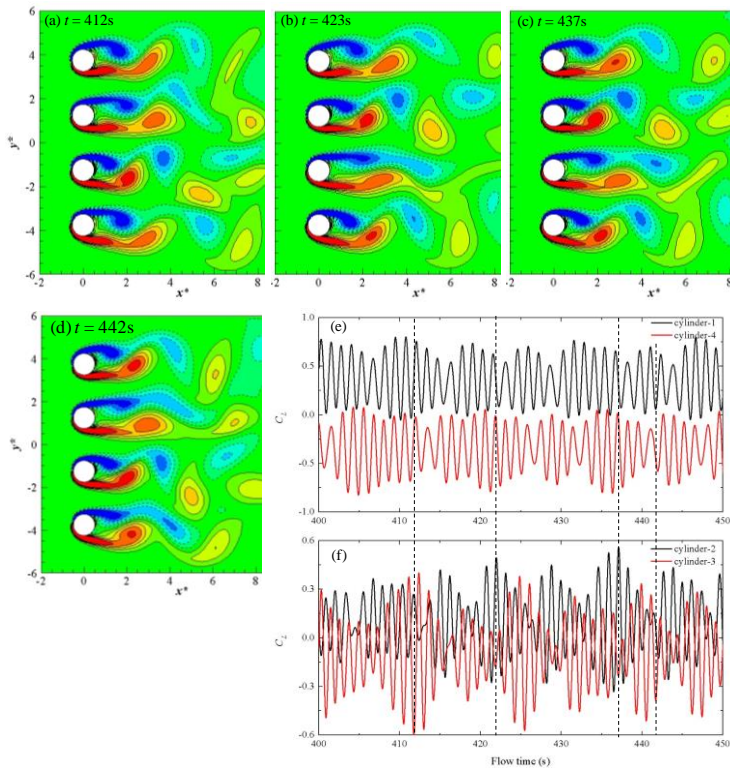


**Fig. 3.** (a-d) Instantaneous vorticity contours and (e, f) time-histories of lift coefficients. $g^* = 1.5$.

From the power spectra of the lift forces, $St = 0.201$ and $0.234$ were estimated for the outer and inner cylinders, respectively. Due to the difference in the shedding frequencies between the outer and inner cylinders, the four cylinders may have a different instantaneous phase lag in their sheddings, e.g., inphase for the upper two

3

cylinders and antiphase for the lower two (Fig. 3a), and vice versa, the upper two antiphase and the lower two inphase (Fig. 3b, c). For the former pattern (Fig. 3a), the fluctuation in the lift is the greatest for cylinder 3 as the sheddings from either gap concerned with the cylinder is coupled (≈0° phase lag); it is the smallest for cylinder 2 as the sheddings are coupled from the lower gap of the cylinder and decoupled (≈180° phase lag) from the upper gap. On the other hand, for the latter pattern (Fig. 3b, c), cylinder 2 - accompanied by coupled shedding from the each of the two adjacent gaps - experiences a larger fluctuating lift (Fig. 3e, f)

Interestingly, when the sheddings from the lower two gaps or the upper two gaps are coupled and the sheddings from the other gap are of about 90° phase lag, there will be a tendency of the sheddings from the latter gap to be coupled, with the shedding from the outer side of the associated inner cylinder slowing down (e.g., cylinder 2, Fig. 3a; cylinder 3, Fig. 3b; cylinder 3, Fig. 3c; cylinder 2, Fig. 3d). In such a case, the corresponding cylinder will have a wider wake and smaller fluctuation in the lift; see the lift of the corresponding cylinder in Fig. 3(f).

The difference in frequencies also makes the time series of the lift forces have a beat-like change with varying amplitude (Fig. 3e, f). The two inner cylinders experience a larger undulation in their lifts than the two outer cylinders. This is because the two inner cylinders have the chance of coupled shedding from the two adjacent gaps. For the outer cylinders, coupled shedding may happen only from one gap concerned.
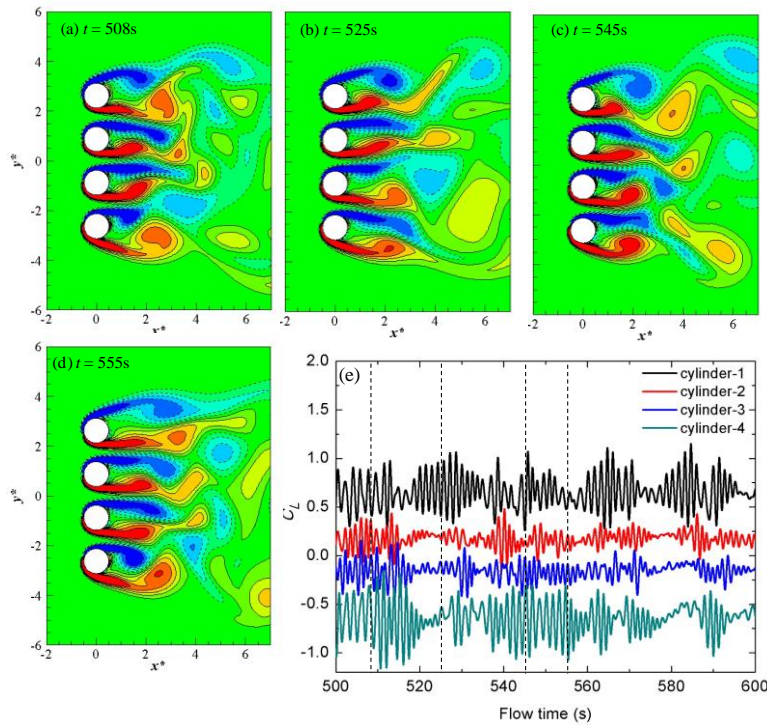


**Fig. 4** (a-d) Instantaneous vorticity contours and (e) time-histories of lift coefficients. $g^* = 0.75$.

***Flip-flopping Flow (0.25 < g*< 1.0)*** Wakes being narrower or wider than that of a single isolated cylinder appear behind the four cylinders when $0.25 < g^* < 1.0$.The narrow and wide wakes switch from one to the other randomly as can be seen from the vorticity patterns and lift signals shown in Fig. 4 for $g^* = 0.75$. The two outer cylinders feature wide wakes (Fig. 4a, c), larger lift amplitudes (Fig. 4e), stronger shedding occurring alternately, coupled sheddings from the gap concerned, while the inner cylinders have opposite features: narrow wakes, smaller lift amplitudes, and weaker shedding not alternating exactly. The larger amplitude of the lift for the outer cylinders largely results from the alternate and coupled sheddings from the gaps concerned. A strong alternating shedding appearing only for cylinder 1 (Fig. 4b) and only for cylinder 4 (Fig. 4d) engenders again a large amplitude of lift of the respective cylinders. The observation implies that the outer and inner cylinders

largely undergo respectively larger and smaller lift amplitudes due to an alternating shedding for the former and almost symmetric shedding for the latter. The symmetric sheddings from the inner cylinders are more conspicuous at a smaller $g^* = 0.5$ (Fig. 5). Comparing Figs. 4 and 5, it can be concluded that the widths of wide and narrow wakes swell and shrink, respectively, with $g^*$ decreasing.
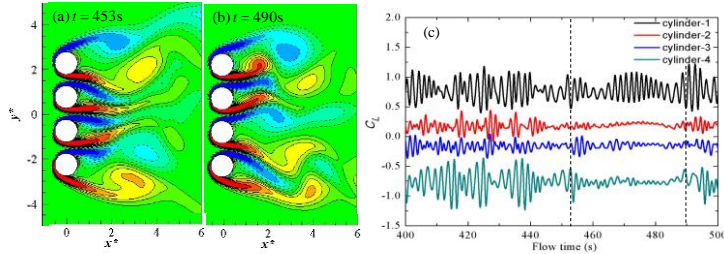


**Fig. 5.** (a-b) Instantaneous vorticity contours and (c) time-histories of lift coefficients. $g^* = 0.5$.

***Single-body Flow ($g^* \leqslant 0.25$)*** The four cylinders act as a combined bluff body where vortex sheddings occur only from the freestream sides of the outer cylinders, forming one Karman wake of a much smaller *St* (Fig. 6a). The gap flows are too weak to form vortices and interfere the freestream side shear layers. However, they move freely up and down following the sheddings from the freestream sides. Lift histories of the four cylinders are regular and of constant amplitude and frequency. A large amplitude of lift, however, prevails for the outer cylinders. Overall, observing the lift signals, it can be concluded that time-mean lift force is always repulsive about $y^* = 0$, decreasing with increasing $g^*$.
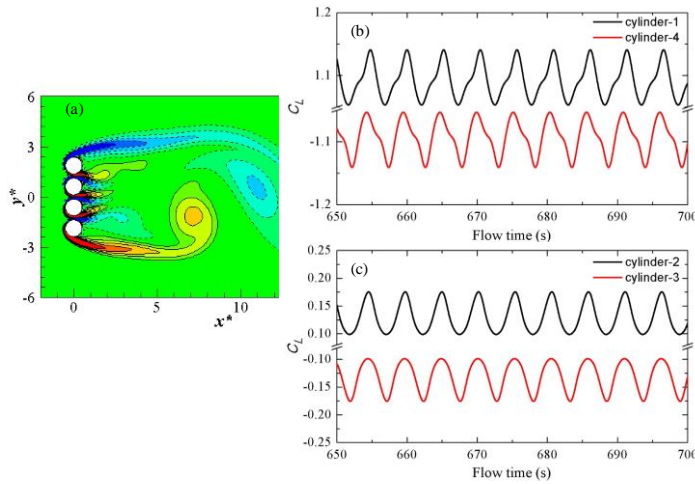


**Fig. 6.** (a) Instantaneous vorticity contours and (b, c) time-histories of lift coefficients. $g^* = 0.25$.

**Total time-mean drag force**

It would be interesting to know how the time-mean drag force on the four cylinders varies with $g^*$. The total drag force $C_{D1-4}$ on the four cylinders is obtained by adding drag forces of the individual cylinders. It is presented as $C_{D1-4}/4C_{D0}$ in Fig. 7, where $C_{D0}$ is the drag force on a single isolated cylinder. $C_{D1-4}/4C_{D0}$ levitates with a decrease in $g^*$ and reaches a maximum of 2.36 when the cylinders are closely connected. That is, the total drag on four cylinders (fingers) in contact is 2.36 times larger than that for a very large spacing. With a decrease in $g^*$, the increase in drag is dramatic ($1.68 \leq C_{D1-4}/4C_{D0} \leq 2.36$), significant ($1.4 < C_{D1-4}/4C_{D0} < 1.68$), and mild ($1.29 \leq C_{D1-4}/4C_{D0} < 1.4$) in the range $g^* \leq 0.25$, $0.25 < g^* < 1.0$ and $1.0 \leq g^* < 2.0$, respectively, corresponding to the single bluff-body, flip-flopping and quasi-interlocked flows. The relationship between $C_{D1-4} / 4C_{D0}$ and $g^*$ can be represented by a best fit curve equation, coefficients obtained using least square method, as follows,

5

$$\frac{C_{D1-4}}{4C_{D0}} = 1.0 + 0.51e^{-0.26g^*} + 0.85e^{-6g^*}.$$

The solid line in Fig. 7 represents the above equation. When $g^* \to \infty$, the equation gives $C_{D1-4} / 4C_{D0} = 1.0$, satisfying that each of the cylinders behaves as single cylinder at a large $g^*$.
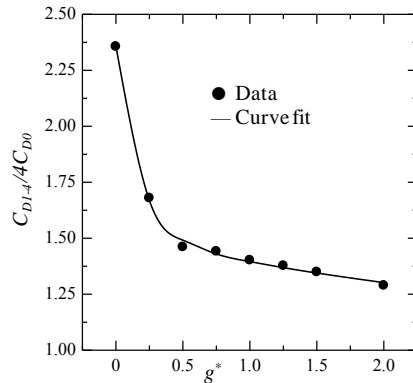


**Fig. 7.** Variation in the total time-mean drag on four cylinders against $g^*$.

## 4. Conclusions

A low-Reynolds number ($Re = 100$) flow around four side-by-side circular cylinders is investigated with a change in $g^*$ from 0 to 2.0. Vorticity patterns, shedding frequencies and drag and lift forces are extracted and presented. Depending on $g^*$ and features of the wake, the flow can be classified into four: single bluff-body, flip-flopping, quasi-interlocked, and interlocked flows appearing at $g^* \leq 0.25$, $0.25 < g^* < 1.0$, $1.0 \leq g^* < 2.0$, and $g^* \geq 2.0$, respectively.

The single bluff-body flow is characterized by a hefty drag force ($1.68 \leq C_{D1-4}/4C_{D0} \leq 2.36$) and a single wake behind the four cylinders. Prevailing wide and narrow wakes behind the cylinders, flip-flopping from one to the other randomly, exemplify the flip-flopping flow. The drag force is still significant ($1.4 < C_{D1-4}/4C_{D0} < 1.68$), but smaller than that in the single bluff-body flow. A further smaller drag force ($1.29 \leq C_{D1-4}/4C_{D0} < 1.4$) prevails in the quasi-interlocked flow where the sheddings from the outer cylinders are interlocked inphase and that from the inner cylinders are antiphase, with a larger shedding frequency appearing for the latter. The interlocked flow features the sheddings from all cylinders occurring in an inphase fashion with an identical frequency.

## 5. Acknowledgments

## 6. References

[1] M.M. Alam, M. Moriya, and H. Sakamoto, "Aerodynamic Characteristics of Two Side-by-Side Circular Cylinders and Application of Wavelet Analysis on the Switching Phenomenon". Journal of Fluids and Structures, Vol. 18, pp. 325-346, 2003.

[2] C.H.K. Williamson, " 2-D and 3-D Aspects of the Wake of a Cylinder, and Their Relation to Wake Computations", Lectures of Applied Mathematics, Vol. 28, pp.719-751, 1991.

[3] C. Norberg, "Fluctuating Lift on a Circular Cylinder: Review and New Measurements", Journal of Fluids and Structures, Vol. 17, pp. 57–96, 2003.

[4] J.R. Meneghini, and F. Saltara, "Numerical Simulation of Flow Interference between Two Circular Cylinders in Tandem and Side-by-Side Arrangements Journal of Fluids and Structures, Vol. 15, pp.327-350, 2001.

[5] H. Ding, C. Shu, Y.O. Yeo, and D. Xu, "Numerical Simulation of Flows around Two Circular Cylinders by Mesh-Free Least Square-Based Finite Difference Methods", International Journal of Numerical Math and Fluids, Vol. 53, pp. 305–332, 2007.

# Experimental and Numerical Measurement of Lift and Drag Force of NACA 0015Aerofoil Blade

Md. Kamal Uddin, Md. Zahidul Islam, Md. Rokunuzzaman, Robiul Islam Rubel

Department of Mechanical Engineering, Rajshahi University of Engineering& Technology,
Rajshahi-6204, Bangladesh

E-mail: kamaluddin.me10@yahoo.com, jahid10ruet@gmail.com, rzaman.mte@ruet.ac.bd,
rubel.ruet10@gmail.com

## Abstract

*A Symmetric aerofoil (NACA 0015) is used in many applications including aircraft vertical stabilizers, submarine fins, rotary and some fixed wings. The ultimate objective of an aerofoil is to obtain the lift necessary to keep an airplane in the air. However, construction of the blade with proper angle of attack implementation has significant effect on lift force. Insufficient lift force might cause failure of airplane flying, especially at high speed. The objective of this paper is to find the aerodynamics characteristics of aerofoil NACA 0015. In this work, numerical and experimental investigation of NACA 0015is studied at different angle of attack (degree) with different velocity of air. The experimental test is conveyed in low speed wind tunnel at the Fluid Mechanics Lab of RUET. The numerical analysis is conducted using ANSYS (combined with CFD and FLUENT FLOW). The use of the CFD technology greatly reduces the overall investment and efforts for aerofoil design. CFD method contributes to visualize the flow pattern inside aerofoil with less time than experimental methods. At the end of investigation, the results of the experimental and numerical data are compared.*

Keywords: Aerofoil, CFD, Lift and Drag Force, Angle of Attack.

## 1. Introduction

An aerofoil is defined as the cross section of a body that is placed in an airstream in order to produce a useful aerodynamic force in the most efficient manner possible. The cross sections of wings, propeller blades, windmill blades, compressor and turbine blades in a jet engine, and hydrofoils, aircraft vertical stabilizers, submarine fins, rotary and some fixed wings are examples of aerofoil[1,2]. The basic geometry of an aerofoil is shown in Fig. 1 and Fig. 2. Since an aerofoil is stream lined body, it may be symmetrical or unsymmetrical in shape characterized by its chord length (C), angle of attack ($\alpha$), and span length (L) [3]. The drag force and lift force significantly depends on its geometrical shape [4]. The proper designing of the aerofoil can minimize the produced drag on the aerofoil [5]. The lift on the aerofoil is due to negative pressure created on the upper part of aerofoil [6]. Low Reynolds number aerofoil aerodynamics is important for both military and civilian applications. The applications include propellers, high-altitude vehicles, sailplanes, light man carrying aircraft, wind turbines, unmanned aerial vehicles (UAVs) and micro air vehicles (MAVs). Flow control over aerofoil is primarily directed at increasing the lift and decreasing the drag produced by the aerofoil [7]. The evaluation of turbulence models for unsteady flows of an oscillating aerofoil has been reported in [8]. In this work, NACA 0015 aerofoil by using five different turbulence models has been considered. It has been found that Spalart-Allmaras turbulence model has a good agreement with experimental results for lift, drag and moment coefficient. The performance of wind turbine using NACA0012 aerofoil using FLUENT programs has been investigated in [9]. Spalart-Allmaras turbulence model for numerical solutions has been used by Lianbing for aerofoil at $3\times 10^6$ Reynolds number, for lift and drag performance and stall angle. NACA 63-415 aerofoil profile has been studied in [10]. Different turbulence model in FLUENT has been used in this work and it is found that SA (Spalart-Allmaras) model is better than others models. Moreover, aerodynamics of aerofoil at low and high angles of attack has been considered. NACA4412 aerofoil profile at $3\times 106$ Reynolds numbers has been studied in [11]. The transition from laminar flow to turbulence flow by using two different numerical models have been investigated which are k-epsilon and Spalart-Allmaras. Numerical results are compared with experimental results. Two numerical models give similar results at high Reynolds number has also been indicated.
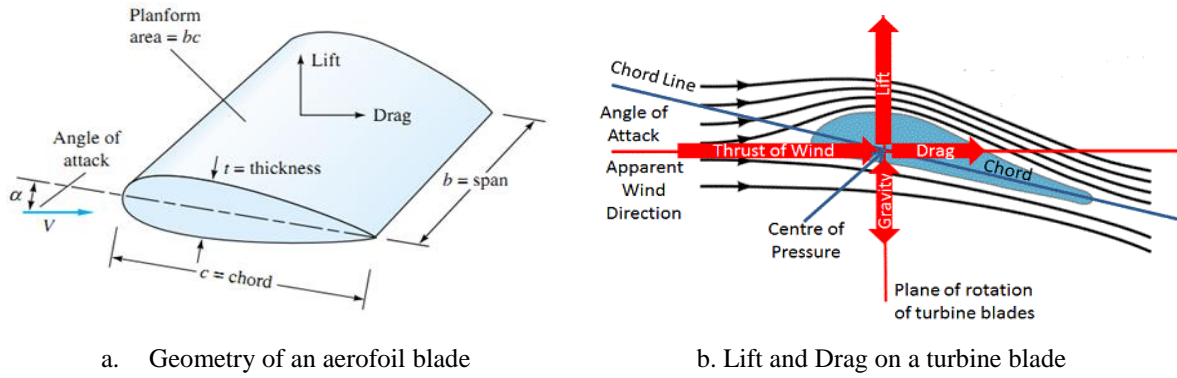
a. Geometry of an aerofoil blade        b. Lift and Drag on a turbine blade

**Fig. 1.** Geometry of an aerofoil blade

A fine mesh is required in the vicinity of the aerofoil to model the flow field precisely. In the vicinity of the aerofoil it is necessary to refine the mesh at the trailing edge in order to confirm accurate modeling, as this would be the point of interest. It is imperative to maintain good aspect ratios of cells through the domain as well as sustaining smooth changes in cell size [12]. Thus quadrilateral elements are used. One of the most practical problems in flight operation is the wing ground interference, or what is called 'collision', during takeoff and landing of aircrafts. Aircraft performance during takeoff and landing is influenced due to the influence in the aerodynamic factors of the wing [13].The aerodynamic characteristics of the wing are changing in the collision phenomena. This paper is intended for finding the aerodynamics characteristics using CFD method and this method has contributed to visualize the flow pattern inside an aerofoil which is faster than experimental methods. The model of NACA 0015 has been chosen for its symmetrical in shape and ease for computation. In this work, Lift and drag force is measured at different velocity by inclined tube manometer. Lift coefficient ($C_l$), drag coefficient ($C_d$) and drag polar ($C_l/C_d$) is also measured.

## 2. Methodology
The experiment is conducted by an open channel wind tunnel having cross section of .3m×.3m and length 0.4m at 8.5-9.65 m/s wind velocity. The model is first prepared by casting followed by other machining processes to obtain the desired model. The model is placed and tested in the open wind tunnel having a motor operating at 2800 rpm which drives tunnel fan. Lift and drag force are measured from balanced arm and velocity of air is determined from inclined tube manometer after placing the model at an angle of attack (2 degree) with an increment of 2 degree. The chosen model is NACA 0015aerofoil blade. Later on an aerofoil body is designed by ANSYS 14.0 workbench design modeler. Boundary conditions are applied to obtain the distribution of turbulence and pressure.

### 2.1 Design Criteria
In this paper, the NACA 0015, the well documented airfoil from the 4-digit series of NACA airfoils, is utilized. The NACA 0015 airfoil is symmetrical; the 00 indicates that it has no chamber. The 15 indicates that the airfoil has a 15% thickness to chord length ratio. It is 15% as thick as it is long. The parameters of the NACA 0015 aerofoil blade are the following:

Chord length of the aerofoil, $C$= 0.06 m

Maximum chamber, m = first digit × % $C$ = $0 \times \frac{1}{100} \times 0.06 = 0$

Distance from leading edge to maximum wing thickness, p = second digit× 10% $C = 0 \times \frac{10}{100} \times 0.06 = 0$

Maximum wing thickness, $t$ = last two digit × % $C$ = $15 \times \frac{1}{100} \times 0.06 = 0.009$m

### 2.2 Reynolds number
The Reynolds number is dimensionless number which is defined by the eq. 1.

$$\text{Re}_L = \frac{\rho V L}{\mu} \tag{1}$$

Where, density of air $\rho$ = 1.23 kg/m³, kinematic viscosity, $\mu$ = 1.973kg.m⁻¹ s⁻¹, span length, $L$ = 26cm

### 2.3 Lift force
Lift on a body is defined as the force on the body in a direction normal to the flow direction. Lift will only be presented if the fluid incorporates a circulatory flow about the body such as that which exists about a spinning cylinder. The velocity above the body is increased and so the static pressure is reduced. The velocity beneath is slowed down giving an increase in static pressure. Consequently, there is a normal force upwards called the lift force. Lift and drag force data are usually expressed in dimensionless terms by using lift coefficient and drag

coefficient. Lift force is a component of total force $F$ perpendicular to the stream of $F\cos\alpha$. The lift coefficient ($C_l$) is defined mathematical by eq. 2.

$$C_l = \frac{2F_L}{\rho V^2 A}$$ (2)

Where, $F_L$ = lift produced, $\rho$ = density of air, $V$ = velocity of the air and $A$ = ($C\times L$) = area of the aerofoil.

## 2.4 Drag force

The drag on a body in an oncoming flow is defined as the force on the body in a direction parallel flow direction. For a windmill to operate efficiently the lift force should be high and drag force should be low. For small angles of attack, lift force is high and drag force is low. If the angles of attack ($\alpha$) increases beyond a certain value, the lift force decreases and the drag forces increases. Therefore, the angle of attack plays a vital role. Lift and drag is presented in Fig. 1(b). There is also a component of total force F in the direction of the stream, which is $F\sin\alpha$. The drag coefficient ($C_d$) is defined as mathematical by eq. 3.

$$C_d = \frac{2F_D}{\rho V^2 A}$$ (3)

Where, $F_D$ = Drag produced, $\rho$ = density of air, $V$ = velocity of the air, and $A$ = ($C\times L$) is the area of the body or aerofoil.

## 2.5 Inputs and Boundary condition

We consider the problem of flow around the aerofoil at 0° - 8° angle of attack. For this, we take some initial inputs and impose some boundary conditions for our problem which is shown in the table 1.

**Table 1.** Inputs and Boundary condition for CFD analysis

| Inputs | Boundary conditions |
| --- | --- |
| Velocity of flow | 8.5-9.65 m/s |
| Operating temperature | 30° C |
| Operating pressure | 1 atm |
| Model | Transition (sst) |
| Density of fluid | 1.23 Kg/m³ |
| Kinematic viscosity | 1.973 kg.m⁻¹ s⁻¹ |
| Reynolds number | Vary with air velocity |
| Length | 0.06 m |
| AOA | 0-8 degree respectively |
| Fluid | Air as an ideal |
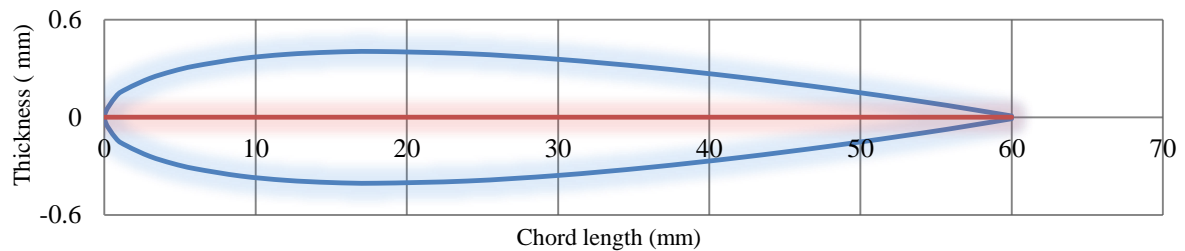


**Fig. 2.** NACA 0015 aerofoil profile
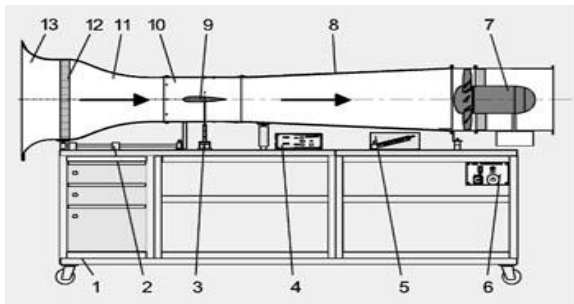


**Fig. 3.** Diagram of an open type wind tunnel

**Fig. 4.** Experimental setup

a.   Aerofoil blade                           b. Balance arm                          c. Protector
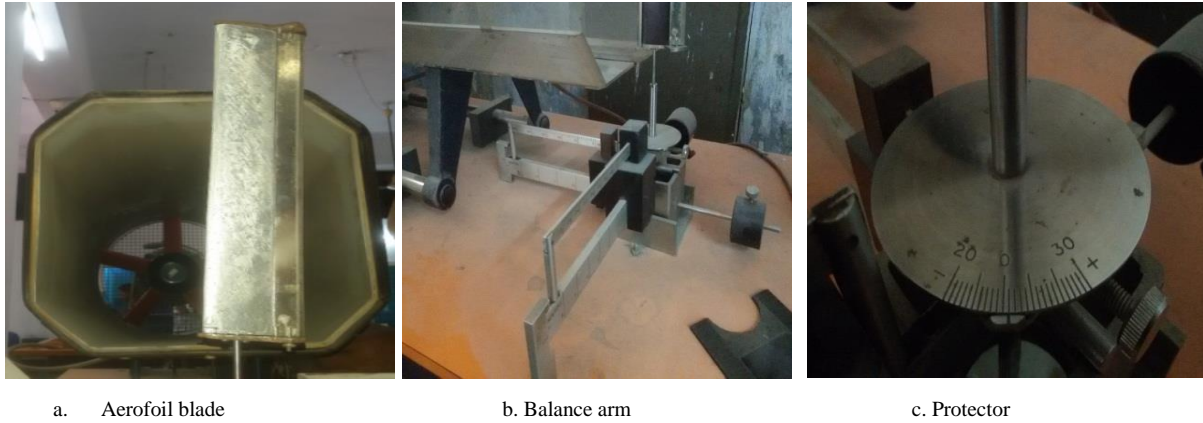
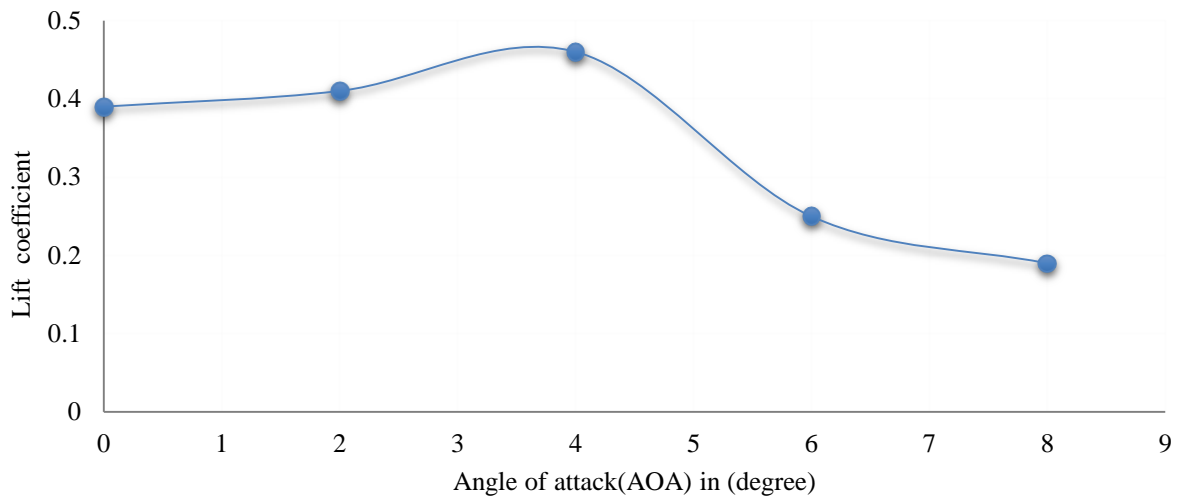**Fig. 5.** Photography of experimental work



**Fig. 6.** Lift coefficient VS angle of attack at different Reynolds's number for NACA 0015

Figure 3 is the diagram of an open type wind tunnel with the following components numbered by (1) Base, (2) Moving carrier, (3) Balance Arm, (4)  Speed Controller, (5) Inclined tube manometer, (6,7) Drive section (Motor, fan), (8) Diffuser, (9) Model, (10) Test Section, (11,13) Contraction Cone. The experimental setup is shown in Fig. 4. The different components of the setup are shown in Fig. 5.

## 3. Results

The experimental data are tabulated in Table 2. The lift coefficient and drag coefficient both depend on angle of attack. The experimental results obtained from our model NACA 0015 are plotted on graph. The Fig. 6 shows that lift coefficient increases with increasing angle of attack and after a certain angle of attack it decreases and this angle is called stall angle. Lift coefficient $C_l$ is maximum (0.46) at 4 degree of angle of attack. The stall angle is caused due to transition from laminar to turbulence flow. It is clear from Fig. 7 that, the value of drag coefficient is increased as angle of attack is increased. From Fig. 8 it is noticed that $C_l/C_d$ is gradually decreased as the value of AOA is increased. The value of lift coefficient is maximum (0.46) at Reynolds number $1.46 \times 10^5$ as shown in Fig. 9. According to Fig. 10 the variation of drag coefficient slightly increases and gives upward line with the increase of Reynolds number of the air for each AOA.

**Table 2.** Experimental data for NACA 0015aerofoil blade

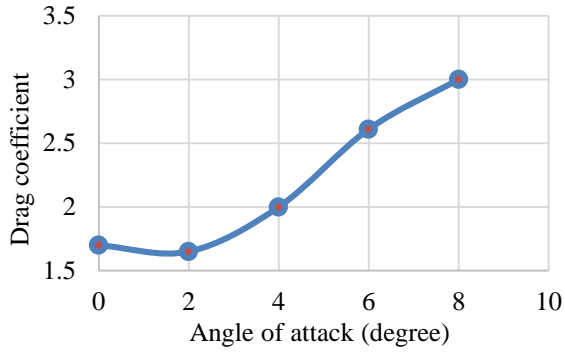| Angle of attack in degree | Lift Coefficient, $C_l$ | Drag coefficient $C_d$ | Reynolds's Number $\times 10^5$ | $C_l/C_d$ |
|---|---|---|---|---|
| 0 | 0.39 | 1.70 | 1.31 | 0.230 |
| 2 | 0.41 | 2.22 | 1.39 | 0.180 |
| 4 | 0.46 | 2.60 | 1.46 | 0.170 |
| 6 | 0.25 | 2.61 | 1.48 | 0.096 |
| 8 | 0.19 | 2.64 | 1.49 | 0.072 |

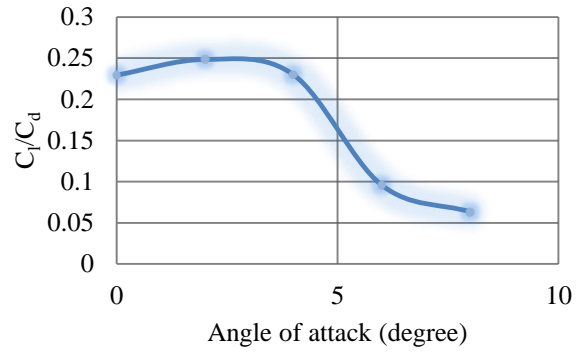**Fig. 7.** Drag coefficient vs. angle of attack



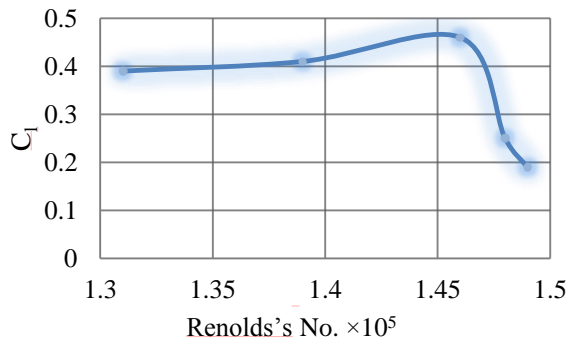**Fig. 8.** Drag polar vs. angle of attack



**Fig. 9.** Lift coefficient vs. Reynolds's number at different angle of attack for NACA 0015
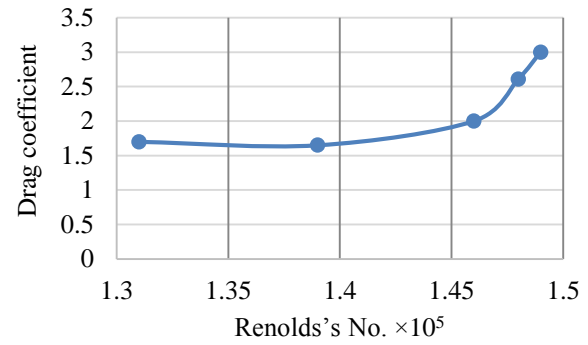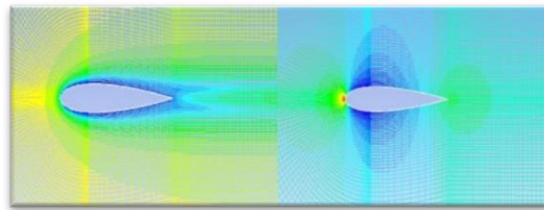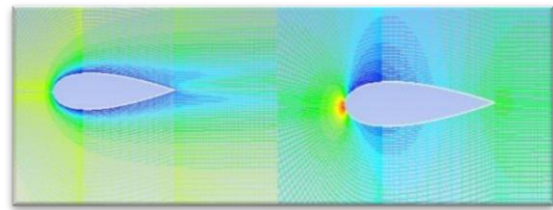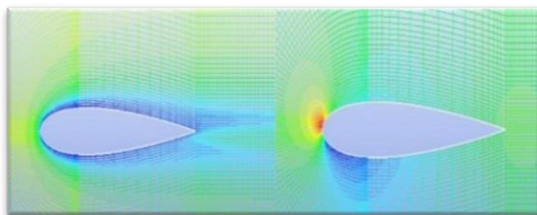


**Fig. 10.** Drag coefficient vs. Reynolds number at different angle of attack for NACA 0015
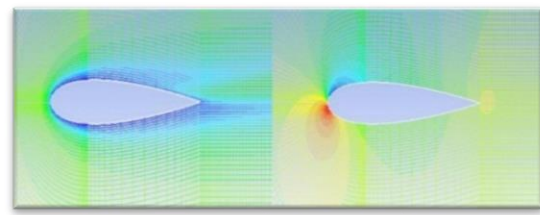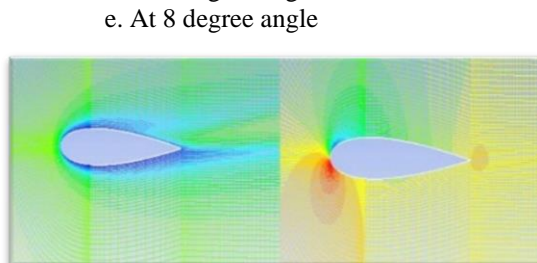


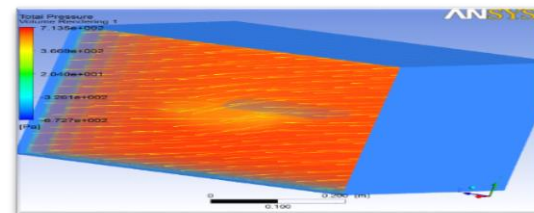a. At 0 degree angle



b. At 2 degree angle



c. At 4 degree angle
e. At 8 degree angle



d. At 6 degree angle
f. Total pressure volume rendering





**Fig. 11.** Distribution of turbulence and distribution of pressure and total pressure volume rendering around NACA 0015 obtained by simulation (ANSYS)

It is clear from Fig. 11(a)-11(e) that pressure developed increases with increasing angle of attack. Thus negative pressure at angle of attack 8 degree is greater than pressure created at angle attack 0,2,4,6 degree. Figure 11(f) shows the total pressure volume rendering after simulation with ANSYS.

## 4. Conclusions

After preparing a NACA 0015 aerofoil blade, experimental and numerical measurement of lift and drag force has been performed. The experiment is compensated for NASA 0015 by an open type wind tunnel. Fluent flow program is used for numerical analysis to show distribution of turbulence, distribution of pressure and total pressure volume rendering around NACA 0015 aerofoil blade. The maximum value of lift coefficient is found as 0.46. The stall angle is found as 4 degree. Both lift and drag coefficient increases as angle of attack is increased. The drag coefficient is gradually decreased as Reynolds's number increases. However, with the increase of Reynolds's number lift coefficient increases slightly and after a certain point it decrease. The optimum value of lift coefficient is found as 0.46 at Reynolds's number of $1.4 \times 10^5$.There is a large negative pressure created on the aerofoil which accounts for most of the lift. The results of the experiments help in designing wind turbine and aircraft wings. Moreover, the proper blade angle can be selected based on the experimental results.

## 5. Acknowledgement

## 6. References

[1] Md. Rasedul Islam, Md. Amzad Hossain, Md. Nizam Uddin, and Mohammad Mashud, "Experimental Evaluation of Aerodynamics Characteristics of a Baseline Aerofoil", *American Journal of Engineering Research (AJER)*, Vol.4, Issue.1, pp. 91-96, 2015

[2] S. Kandwal, and S. Singh, "Computational Fluid Dynamics Study of Fluid Flow and Aerodynamic Forces on an Aerofoil", *IJERT*, Vol.1, Issue.7, 2012

[3] R. K. Bansal, "Fluid Mechanics And Hydraulic Machines", *Laxmi Publication (P) Ltd*, 9th Edition, pp. 686- 687, 2010.

[4] M. Morshed, S. B. Sayeed, S. A. Al Mamun, and G.M. Jahangir Alam, "Investigation of Drag Analysis of Four Different Profiles Tested at Subsonic Wind Tunnel", Journal *of Modern Science and Technology*, Vol.2, No.2, pp. 113-126, 2014

[5] Izzet Şahin, and Adem Acir, "Numerical and Experimental Investigations of Lift and Drag Performances of NACA 0015 Wind Turbine Aerofoil", *International Journal of Materials, Mechanics and Manufacturing*, Vol.3, No.1, pp. 22-25, 2015

[6] E. H. Lewitt, "Hydraulics and Fluid Mechanics", *Sir Isaac Pitman & Sons Ltd*, 10th Edition, pp.382-383, 1963

[7] Zifeng Yang, Hirofumi Igarashi, Mathew Martin, and Hui Hu, "An Experimental Investigation on Aerodynamic Hysteresis of a Low-Reynolds Number Aerofoil", *American Institute of Aeronautics and Astronautics*, AIAA-2008-0315, 2008

[8] G. R. Srinivasan, J. A. Ekaterinaris and W. J. McCroskey, "Evaluation of Turbulence Model for Unsteady Flows of an Oscillating Aerofoil", *Elsevier Science Ltd.*, Computers & Fluids, Vol.24, No.7, pp. 833-861, 1995

[9] L. B. Li, Y. W. Ma, and L. Liu, "Numerical Simulation on Aerodynamics Performance of Wind Turbine Aerofoil", *IEEE Conference on World Automation Congress (WAC), Puerto Vallarta, Mexico*, ISSN. 2154-4824, pp. 1-4, 2012

[10] F. Villalpanda, M. Reggio, and A. Ilinca, "Assessment of Turbulence Model for Flow Simulation Around a Wind Turbine Aerofoil", *Modeling and Simulation in Engineering*, *Hindawi Publishing Corp.*, New York, United States Vol.2011, No.06, 2011

[11] H. C. Ravi, N. Madhukeshwara, and S. Kumarappa, "Numerical Investigation of Flow Transition for NACA 4412 Aerofoil Using Computational Fluid Dynamics", *International Journal of Innovative Research in Science Engineering and Technology*, Vol.2, Issue.7, pp. 2778-2785, 2013

[12] Hakim Tarteeb Kadhim, "Computational Modeling of Turbulent Flow around Aerofoil Using Different Turbulence Models" *Al-Qadisiya Journal for Engineering Science,*Vol.7, No.3, pp. 278-289, 2014

[13] H. H. Al-Kayiem and AK Kartigesh, "An Investigation on the Aerodynamic Characteristics of 2-D Airfoil in Ground Collision", *Journal of Engineering Science and Technology*, Vol.6, No.3, pp. 369-381, 2011